Swansea University
Prifysgol Abertawe

Impact of Tides and Calving on Glacier Flow

James Colinese

Swansea University

Submitted to Swansea University in fulfilment of the requirements for the Degree of Masters by Research.

September 2023

Abstract

Globally, sea level rise poses an ever-increasing threat to coastal areas. Tidewater glaciers fed from the Greenland ice sheet directly (the second largest ice sheet on earth) interact with the sea and the ocean tides. Our understanding of the ocean interaction and tidewater glaciers is still developing with regional and glacier-specific differences. During the 2013 summer, 20 GPS nodes were placed near the glacier front of Helheim Glacier for ~44 days, recording the position every 4-7 seconds. Iceberg calving resulted in many nodes being lost from the glacier front, with only 5 surviving the season. The GPS data was filtered using a Kalman filter to remove variance occurring from the harsh environment and inherent inaccuracies of GPS. This allowed the identification of long-term trends and tidal signals. Median horizontal glacier velocity ranged between 16 and 24m/d, with peaks reaching over 38m/d after some calving events. There is evidence of semi-diurnal modulation in both height and flow rate. Peak height varied slightly out of phase with the tide, with peak height occurring ~2 hours after high tide. Peak horizontal velocity occurred at low tide also with a ~2-hour delay; this is attributed to the increased water depth at high tide buttressing Helheim Glacier and retarding flow; then, during low tide, there is less force allowing flow to increase. Semi-diurnal height modulation is found at the front centre of Helheim Glacier, showing that part of Helheim is semi-floating, because glacial earthquakes are also identified. During calving events, the glacier front saw flow speeds increase by 30% in some regions, and other portions experienced no changes, indicating that the flow regime of the glacier front is highly variable. This research shows the plethora of information available when using GPS data. Future research should explore the Kalman Filter and increased GPS usage focusing on long-term deployment across the glacier.

Declaration

This work has not previously been accepted in substance for any degree and is not being concurrently submitted in candidature for any degree.

Signed.....  .....

Date……..05/10/2024.....

This thesis is the result of my own investigations, except where otherwise stated. Other sources are acknowledged by footnotes giving explicit references. A bibliography is appended.

Signed.....  .....

Date……05/10/2024.....

I hereby give consent for my thesis, if accepted, to be available for electronic sharing.

Signed.....  .....

Date……05/10/2024.....

The University's ethical procedures have been followed, and where appropriate, that ethical approval has been granted.

Signed.....  .....

Date……..05/10/2024.....

Acknowledgements

I want to express my sincere gratitude to everyone who has helped and guided me through this year.

Supervisors:

I extend my heartfelt thanks to my primary supervisors, Tavi Murray, and Rebecca Schlegel, for their support and guidance throughout this journey. Their patience during confusing moments and the constant pursuit of excellence in my work have been invaluable.

I am also extremely grateful to my external supervisors, Stuart Edwards, and Christopher Pearson, for their expert guidance, particularly Christopher's dedicated time spent with me on the Kalman Filter.

Data Contributors:

Special thanks to Fiammetta Straneo for generously providing the tide gauge data and to Michael Shahin for supplying the air temperature data.

Colleagues and Office:

I am indebted to the wonderful individuals in my office who welcomed me with open arms and provided a supportive environment. Your warmth and kindness are something I will cherish.

Friends and Family:

Finally, I want to express my deepest appreciation to my friends and family for their unwavering support throughout this year. Your willingness to listen to my trials and tribulations has strengthened and motivated me.

I am genuinely grateful to everyone who played a part in this year. Your contributions have been instrumental, and without you, I would not have finished.

Contents

List of Figures

List of Tables

List of Acronyms

AD: Anno Domini (refers to years after the traditionally reckoned year of the birth of Jesus Christ)

CMIP6: Coupled Model Intercomparison Project Phase 6

DEM: Digital Elevation Model

DMI: Danish Meteorological Institute

DOY: Day of Year

EPSG: European Petroleum Survey Group

ENU: Easting, Northing, Up

GMSL: Global Mean Sea Level

GSN: Global Seismographic Network

GPS: Global Positioning System

GrIS: Greenland Ice Sheet

Gt/yr: Gigatons per year

GE: Glacial Earthquake

K1: Principal lunar diurnal tidal constituent

Km: Kilometre

M2: Principal lunar semidiurnal tidal constituent

m/d: Meters per Day

MATLAB: Matrix Laboratory

NAC: North Atlantic Current

NAN: Not a Number

PE: Percent Energy

S2: Principal solar semidiurnal constituent

SLR: Sea Level Rise

SNR: Signal-to-Noise Ratio

SST: Sea Surface Temperatures

SSWT: Subsurface Water Temperature

TWG: Tidewater Glaciers

UTide: Unified Tidal Analysis and Prediction Package

UTM: Universal Transverse Mercator

WGS: World Geodetic System

Chapter 1 - Introduction

This thesis applies Global Positioning System (GPS) techniques, to examine Helheim glacier's flow behaviour and how this is impacted by both iceberg calving events and tides. In the opening chapter, background information is provided on topics such as tidewater glaciers, the impact of global temperature on the Greenland Ice Sheet, and what might happen to sea levels in the future. Then explain why this research is essential and what this research hopes to achieve. Finally, the structure of the thesis is outlined ahead.

1.1 Temperature

As global temperatures increase because of climate change (IPCC 2021), glaciers worldwide are under threat. Greenland is situated between the Arctic and Atlantic oceans and the Greenland Ice Sheet (GRIS), is "currently the fastest melting ice sheet in the cryosphere" (Gallagher et al., 2020). In Greenland, the total land surface area covered by ice is roughly 82%, equating to ~2 x 10^6 km^3 (Catania et al., 2020; Ohmura, 2011) equivalent to a volume of ~2.6 - 2.8 million km^3 of ice (Christoffersen & Hambrey, 2006; Weidick et al., 1995). Approximately 97% of glaciers in Greenland are part of GrIS, with the remaining ice consisting of mountain glaciers and ice caps (Ohmura, 2011). Ignoring the effects of hydro-isostasy, a complete melting of the GrIS would lead to a 6-7.5m rise in global sea level(Aschwanden et al., 2019; Christoffersen & Hambrey, 2006; Morlighem et al., 2017; Ohmura, 2011). By 2018, mass loss from the GrIS reached 286±20 Gt/yr (2010-18), an almost 600% increase compared to 1990-2000 (Mouginot et al., 2019).

1.2 Tidewater/Outlet Glaciers

A large portion of the GrIS is drained by outlet glaciers flowing through valleys or troughs. If these outlet glaciers terminate in ocean water (typically in narrow ocean fjords), they are known as tidewater glaciers (D. Benn & Evans, 2014). Enderlin et al. (2014) reported that the 15 largest tidewater glaciers account for 77% of the discharge recorded from the GrIS.

Other researchers have noted that 181 gigatonnes of mass are lost annually on the GrIS, equating to 1.32 mm/yr in global sea level rise (Bamber et al., 2018; Gallagher et al., 2020). From 1972-2018 ~66% of mass loss from the GrIS has been associated with changing dynamics of tidewater glaciers, thought to be a direct cause of a ~9 mm rise in sea level in the period from 1972 to 2018 (Catania et al., 2020; Miles et al., 2016; Mouginot et al.,

2019). The outlet glaciers in Greenland typically have much higher flow velocities than Antarctic ice streams.

Greenland's outlet/tidewater glaciers accelerate due to oceanic and atmospheric drivers (Ultee et al., 2022) and are sensitive to a warming climate (Juan, 2011). Climate-induced ice sheet change is observable in coastal areas with interaction with the ocean and warmer temperatures. In the summer, surface melt drains into the fjords/ocean as surface runoff and through subglacial channels. These channels lubricate the bed, increasing flow speed and potentially increasing iceberg calving (Juan, 2011). Three of the largest tidewater glaciers in Greenland (Helheim Glacier, Kangerlussuaq and Jakobshavn) in 2005 accounted for 28% of the GrIS mass loss (Joughin et al., 2012; Rignot & Kanagaratnam, 2006). Flow speeds of these glaciers range between 20-35m/d (Amundson et al., 2008; Luckman et al., 2006).

1.2 Climate of Greenland

The first decade of this millennium stands to be warmer than any other decade over the previous 1000 years (Hansen et al., 2010; Mernild et al., 2014). 2010-2020 has seen continued warming, with 2020 marking the 44th consecutive year since 1977 when global land and ocean temperatures were above the 20th-century average (NOAA, 2021). Since the 1990s, melt induced by summer warming has extended from the coastline across the ice sheet (Hanna et al., 2021). From 1991-2019 (28 years), Greenland has experienced significant warming over winter (~4.4°C), spring (~2.7°C), and summer (~1.7°C). West/Northwest Greenland experienced the most extreme warming in winter of ~6–6.5°C (Hanna et al., 2021). Employing a climate scenario of 2.8℃ warming by 2100, four glaciers in Greenland (Petermann, Kangerdlugssuaq, Jakobshavn Isbrae and Helheim Glacier) that account for 22% of discharge from the GrIS would contribute 19-30 mm to sea level rise by 2200 (Nick et al., 2013).

1.3 Sea Level Rise

From 1901-2018 Global Mean Sea Level (GMSL) has risen by 0.2 m (IPCC, 2021b). It can be attributed to several factors, including the loss of land-based ice masses, changes in terrestrial water storage, and thermal expansion (Khan et al., 2020). Projections suggest that by 2100 this sea level rise could increase to a range of 0.7 to 2 m due to accelerated ice loss (Bamber et al., 2019; Khan et al., 2020). When considering the historical context after

the last ice age, it is believed that Sea Level Rise (SLR) rates reached 80 mm/yr (Christoffersen & Hambrey, 2006), implying the potential for even more rapid changes in the future.

The most significant water reservoirs in the world are the Greenland Ice Sheet (GrIS) and the Antarctic Ice Sheet (Fox-Kemper et al., 2021), which stores this water frozen as ice. To put things in perspective, if the GrIS and Antarctic ice sheets were to melt entirely, they would result in approximately 7 meters and 57 meters of global sea level rise respectively (Lemke et al., 2007; Ohmura, 2011). Hence, the ability to model environmental changes in these ice sheets is critical for understanding the potential impact of climate change on a global scale.

Global sea level rise poses an escalating threat to coastal areas worldwide. The GrIS significantly contributes to this phenomenon, accounting for 25% of the observed GMSL rise (Straneo & Heimbach, 2013). The SLR contribution from Greenland is increasing at an accelerated rate. The GrIS during 1993-2003 contributed to 0.21±0.07 mm/yr^{-1} of SLR, a steep increase compared with 1961-2003 when it contributed only 0.05 ± 0.12 mm yr^{-1} (Bindoff et al., 2007). Other studies using repeated laser-altimeter surveys show that from 1997-2003, the average ice loss was 80 ± 12 km^3 yr^{-1}. During 1993-1999, this was only 60 km^3 yr^{-1} (Krabill et al., 2004). A leading mechanism in transferring freshwater into the oceans is mass loss at the calving front (where the ice breaks off) of tidewater glaciers (TWG). Understanding how these areas work, and the processes involved is critical in creating parameters in SLR predictions (Luckman et al., 2015).

Rignot et al. (2015) believe Greenland's sensitivity to ocean warming and enhanced runoff is underestimated, and projections must be updated. As air and ocean temperatures increase, the mass balance of GrIS is unknown (Khan et al., 2015). Research of these crucial regions is of utmost importance if better models of future climate scenarios are to improve.

1.4 Aims of this Thesis

A better understanding of dynamics and improved modelling is needed to understand TWGs and the likely impact of a changing climate (Benn et al. 2017). This thesis aims to continue the work done by Tavi Murray (Swansea University) and Stuart Edwards (Newcastle University) whereby they deployed a network of GPS receivers on Helheim Glacier near the calving front during the summer of 2013. Several papers have been published using the data set they collected, and the goal of this thesis is to further

contribute to the overall understanding of Helheim by trying new and different approaches to filtering data and focusing on investigating if the ocean tides modulate flow on Helheim Glacier. The importance of TWGs and their mechanisms are outlined in Chapter 2.

1.3.1 Research Objectives/Questions

- Write a Kalman Filter to filter and process the GPS data, producing a high-quality, robust data set.
- Investigate:
    - How tidal modulation affects the glacier's vertical and horizontal displacement.
    - The impact on glacier flow during calving events.
    - Whether tidal modulation during calving is affected significantly.

1.5 Thesis Outline

This chapter has presented a general overview of the state of Greenland and its vulnerability to climate change and the research questions, investigated and explained in the following chapters.

Chapter 2 is split into 4 sections:

- Section 1 explains tidewater glaciers and their dynamics, including the links between air and ocean temperatures and calving events together with the associated glacial earthquakes.
- Section 2 introduces tides and how their cause is due to the gravitational interactions between the Moon, Sun, and Earth in forming the dominant tidal constituents.
- Section 3 brings the concepts presented in Chapters 2 and 3 and presents how tides are reported to affect glaciers across the globe, from semi-diurnal flow variations in Alaska and Greenland to stick-slip motion in Antarctica.
- Section 4 introduces Helheim Glacier, explaining in detail our understanding of its fjord interaction, past and present flow dynamics, calving and our current research around tidal modulation at Helheim Glacier.

Chapter 3 is an in-depth explanation of the GPS network used, the process and the challenges of filtering GPS data, the equations and process of identifying tidal modulation

from U-Tide, and together with other data and methods used such as that from the tide gauge and the identification of calving events.

Chapter 4 presents the results of the methods described in Chapter 3, first explaining the general trends and some individual GPS position dynamics, then going into detail about the tidal modulation of height and horizontal flow and then deconstructing how flow changes before and after calving events.

Chapter 5 discusses the results of Chapter 4, showing that the height for the modulating nodes is anti-correlated but the horizontal flow in time with the tide, showing regions that are semi-floating during the 2013 summer. Then, an explanation of the dynamics occurring is given. Lastly, a description of some of the limitations of this research with some ideas for improvement and areas for further study.

Chapter 6 summarises the work presented in this thesis and provides an overview of areas identified for future research.

Chapter 7 is an appendix of extended material for the methodology and results.

Chapter 8 has the full Reference list.

Chapter 2 – Literature Review

The following literature review is split into 4 sections, the first section describes what tidewater glaciers are and explains the processes that affect their flow. The second section describes the tides, their formation, and their main constituents. Then putting these concepts together, the third section describes the tidal impact on glaciers in Greenland, Alaska, and Antarctica. The last section details Helheim Glacier, explaining the past and current flow dynamics and notes what research has already revealed regarding the tidal impact on Helheim Glacier's flow.

2.1 Tidewater Glaciers

2.1.1 Overview

Tidewater Glaciers (TWG) are outlet glaciers that terminate into the ocean water usually through narrow ocean fjords, they can be either grounded at the calving front or have a short floating tongue (D. Benn & Evans, 2014; Moon & Joughin, 2008). The dynamics of TWG are more complex than other glaciers due to the glacier-ocean interface, which is affected by factors such as the rising and falling ocean tide and the effects of submarine melt caused by warm waters (Luckman et al., 2015; O'Leary & Christoffersen, 2013; Stevens et al., 2022; Vaňková & Holland, 2016). TWGs in Greenland are known for their fast flow speeds because of reduced basal friction (Cassotto et al., 2018).

Physical processes associated with TWGs are still not fully understood. Comprehending TWG dynamics is crucial in predicting how climate change will impact their dynamics and contribution to sea-level rise (Benn, Cowton et al., 2017; Vieli et al., 2001). For example, when a TWG front is at a submarine frontal moraine (debris build-up at the glacier tongue underwater), the terminus can begin to retreat into deeper water, coinciding with increased calving activity, causing an enhanced retreat (Meier & Post, 1987; Vieli et al., 2001). TWGs can also undergo cycles of stable phases marked by slow advance (~100-1000 years), followed by swift and drastic retreat (over 10-100 years) (Larsen et al., 2015; Post et al., 2011; Vieli et al., 2001).

Climate change is impacting the behaviour and dynamics of TWG. Glaciers may thin as temperatures continue to rise, and thinning can increase driving stress if the surface slope increases. For example, Aavatsmarkbreen Glacier in Svalbard retreated 1.7 km between 1983 and 2013 alongside thinning and steepening. The surface slope increased from 2.9˚ to

5.3˚ in the lower 4 km, and driving stress increased from 55 kPa to 63 kPa in certain regions, resulting in Aavatsmarkbreen accelerating (Sevestre et al., 2018). However, shear stress depends on the slope and glacier thickness, so thinning can lead to increased or decreased shear stress.

Tidewater glaciers occur across the globe. Principle regions of study and some example glaciers include Alaska (e.g., LeConte, Yahtse Glacier (Bartholomaus et al., 2015; O'Neel et al., 2003)), Svalbard (e.g., Hansbreen and Tunabreen (Błaszczyk et al., 2021; Holmes et al., 2019)) and Greenland (e.g., Helheim Glacier, Jakobshavn Isbræ (Cassotto et al., 2018; Voytenko et al., 2015). Since the advent of remote sensing, accurate quantification of glacier changes over weekly and longer time scales has been possible. Understanding shorter-term glacier change is also paramount (Bartholomaus et al., 2015; Stevens et al., 2022) and remains challenging. Significant focus on the controls and limits of TWGs arises from using the position of their termini as a global indicator of glacier change (Catania et al., 2018). In Alaska, nearly all TWG are in a "retracted stable" (Larsen et al., 2015) state, no longer going through phases of advance and retreat (Larsen et al., 2015; Post et al., 2011) since the dramatic retreat post-Little Ice Age (Larsen et al., 2015). As a result, Alaskan land-terminating glaciers are becoming the dominant contributor to sea level rise (SLR) compared to Alaskan TWGs because many TWGs have become stable in their retreat (Larsen et al., 2015). However, in Greenland, 30 to 50% of annual mass loss from the GrIS into the ocean is from a combination of iceberg calving and submarine melting from TWGs (D. I. Benn, Cowton, et al., 2017).

2.1.2 Controls of TWG Dynamics

The dynamics and mechanisms that control TWG are more complex than land-terminating glaciers because of their interaction with fjord waters and mass loss through iceberg calving and submarine melt processes. The response to environmental changes can have vastly different impacts on mechanisms. The main factors are interactions between temperature, calving and fjord water (Figure 2:1). The challenge at present is to try and fully understand the mechanisms controlling TWGs and how they interlink. On top of these complex interactions, there is evidence of glacier regional synchroneity and responses of individual glaciers that make it harder to differentiate whether specific changes are due to individual glacier-related factors or part of a regional change. For example, Greenland has a regional influence from ocean forcing (Luckman et al., 2006); however, independent responses are superimposed.

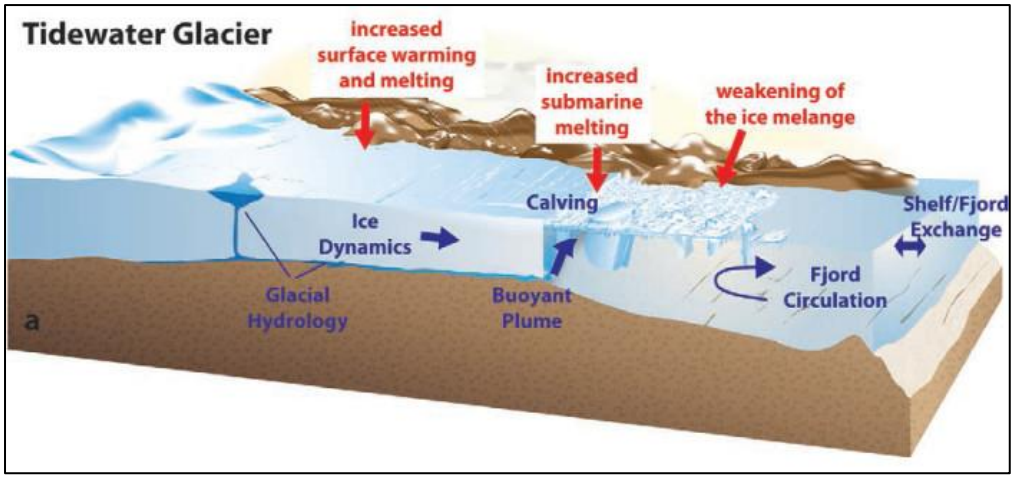

Figure 2:1, The mechanisms for glacier retreat and acceleration (red) and the key processes (blue), created by Straneo et al. (2013).

2.1.2.1 Temperature

TWG dynamics are complex due to ice flow interactions between the oceans and atmosphere (Catania et al., 2020; Stevens et al., 2022). Accurately predicting how glaciers will react to a warming climate is difficult because glaciers are sensitive to small changes in atmospheric forcings (Sugiyama et al., 2015). There are many different possible future climate scenarios all dependent on our future emissions (IPCC, 2021a). To effectively model these scenarios and predict mass changes in glaciers, it is crucial to fully understand how temperature changes, impact glacier dynamics (Huss & Hock, 2015). There is a connection between TWGs and changing ocean and air temperature, changes in seawater depth at the terminus and the ice supply to the glacier front (Truffer & Motyka, 2016).

There is typically an annual cycle of glacier advance during cooler periods and retreat during the warmer months (Schild & Hamilton, 2013). Finding a simple correlation between the annual onset of terminus retreat and the arrival of sub-zero temperatures is elusive. However, there is a link between the clearing of the sea-ice mélange and terminus mobility (Howat et al., 2010; Schild & Hamilton, 2013).

2.1.2.2 Air Temperature

Air temperature warming will either cause increased melting through ablation processes or increased accumulation through increased precipitation, depending on geography (Benn & Evans, 2014). In Greenland, the increase in ice loss from surface melt is driven by air temperature changes (Hanna et al., 2012; Van Den Broeke et al., 2016). In the summer of 2012, there were record levels of melt on the Greenland Ice Sheet (GrIS) due to changes in the Summer North Atlantic Oscillation favouring warm air advection from the south along

the western coast, causing extreme ice loss (Hanna et al., 2014; Straneo et al., 2016). Surface melt from warm air temperatures has a profound effect on glacier flow. Meltwater accumulates at the surface, filling crevasses or forming supraglacial lakes/streams, penetrating the ice sheet through moulins or crevasses (Benn & Evans, 2014). Increased surface melt means more water supplied to the glacier bed, which could increase basal water pressure, decoupling the glacier from the bed, and allowing glacier acceleration (Kamb, 1987; Tuckett et al., 2019). From 2000-2010, basal melting of the GrIS increased by 2.9 ± 5.2 Gt/yr. Looking to the future, as global warming continues, the Arctic will warm, driving increased basal melting and leading to faster glacier flow (Karlsson et al., 2021).

2.1.2.3 Ocean Temperature

CMIP6 (Coupled Model Intercomparison Project Phase 6) models suggest that sea surface temperatures (SST) are also increasing; over the next 100 years, SST increases could range from 0.43-1.47℃ depending on the climate scenario considered (Fox-Kemper et al., 2021). Variations in ocean temperatures directly influence ablation at the glacier front of TWGs leading to changes in submarine melt and iceberg calving (Bartholomaus et al., 2013; Holmes et al., 2019). Collectively, these two processes are known as frontal ablation.

SST could have a longer-lasting impact on glacier flow than the air temperature. When the air temperature drops below freezing, there is a time lag where ocean temperatures remain above freezing, in some places lasting over two months (Błaszczyk et al., 2021). Luckman et al. (2015) reported frontal ablation continues 1-2 months after air temperatures and SST has fallen below 0℃ but is in sync with sub-surface ocean temperatures. Furthermore, the duration of TWG retreat in some locations is determined by ocean temperature, irrespective of air temperature. For example, Hansbreen in Svalbard retreats in June/July, coinciding with sea temperature increases, ending around October/December (Błaszczyk et al., 2021). In Greenland, TWGs are indicators of dynamic thinning of the GrIS, with retreat indicating increased calving contributing to SLR or increased melting (Murray, Scharrer, et al., 2015).

2.1.2.4 Are Air Temperature and Ocean Temperature Coupled?

Acceleration and retreat of TWGs are due to responses of both air and ocean temperatures. These variables are not isolated. From 1995 through 2010, Bevan et al. (2012) found that an increase in glacier flow speed coincided with an increase in the mean summer air and SST. Straneo and Heimbach (2013) noted that subpolar North Atlantic warming intensified due to increased air temperatures, leading to enhanced submarine melt, triggering the retreat

of Greenland's TWG. When water temperatures are high, frontal ablation is significantly affected through increased submarine melt-promoting calving. However, when temperatures are low, air temperature might have greater control over ablation (Holmes et al., 2019). Increased atmospheric temperatures increase subglacial discharge, manifesting as submarine melting in the summer. However, during the winter, atmospheric increases have a negligible effect in direct contrast to ocean temperatures. Because the consequences from a warming ocean are identifiable year-round (Slater & Straneo, 2022), the role of atmospheric and ocean temperature in Greenland's TWG retreat and speed up is regionally specific. Slater and Straneo (2022) reconstructed submarine melting in Greenland between 1979 and 2018. They found that ocean warming was the main factor in South and Central-West Greenland, whereas, in the Northwest, it was the atmosphere. A thorough acknowledgement of atmospheric and ocean changes is essential to fully understand the impacts of submarine melting (Slater & Straneo, 2022).

2.1.2.5 Calving

Alongside submarine melt, calving is the second factor in frontal ablation (Benn, Cowton, et al., 2017; Luckman et al., 2015; O'Leary & Christoffersen, 2013). Calving events occur when large bodies of ice break off the end of a glacier (D. I. Benn, Cowton, et al., 2017). At TWGs, this ice forms icebergs and ”bergy bits” (NOAA, 2023) floating in the fjord, which can fuse with sea ice, forming an ice mélange at the front of the glacier (Figure 2:2). In Greenland, 30-50% of total mass loss directly occurs from calving (Enderlin et al., 2014; Murray, Nettles et al., 2015). Observations of calving regimes and monitoring their change can indicate atmospheric and oceanic changes (Holmes et al., 2019). An improved understanding of the processes related to calving is fundamental in understanding global SLR due to the direct ocean interface and the contribution from GrIS and the Antarctic ice sheet (Murray et al., 2015).

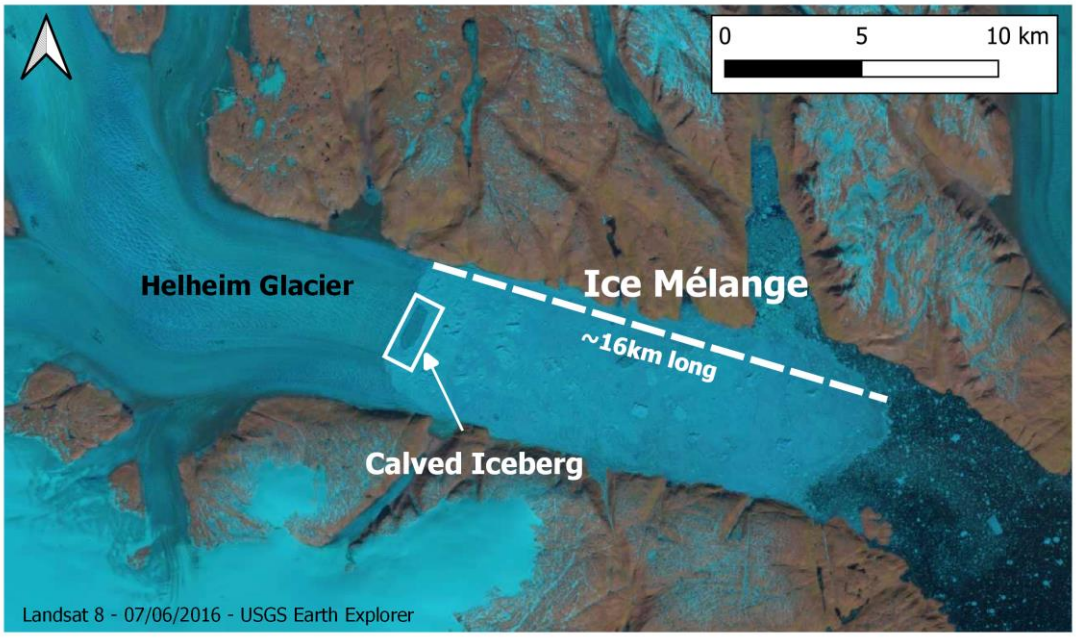

Figure 2:2, Helheim Glaciers ice mélange and calved Icebergs floating in Sermilik Fjord. Landsat 8 images Accessed from USGS Earth Explorer and reprojected in QGIS.

2.1.2.5.1 Mechanisms of Calving

Calving is a complex process with many factors in play. Alongside the dangerous nature of an active calving front, understanding the exact calving mechanisms is unknown and variable between glaciers (O'Neel et al., 2003). There are many theories of what causes calving. One leading theory involves submarine melt-induced fracture, where warm water melts the glacier ice, causing fractures. The fractures propagate vertically, causing ice break-off (Bartholomaus et al., 2013; Luckman et al., 2015; Medrzycka et al., 2016). Many models include complex fracture mechanics focusing on surface crevassing (Krug et al., 2014) without considering whether the glacier is grounded or floating. Observations and models suggest buoyancy forces and basal crevasse formation and propagation are important (Cook et al., 2014; Murray, Selmes, et al., 2015; O'Neel et al., 2003).

Making models and predicting calving is difficult because local variables such as the shape and size of the front of glaciers are not uniform, pre-existing weak points are unknown, and bed topography is inconsistent (Nick et al., 2010). For example, post-calving, glacier flow speed can increase. For example, Cassotto et al. (2018) found a ~10% increase in flow speed after significant calving events. However, there was no correlation between calving area loss and increased flow speed. They also found sizeable (~30 m) elevation changes after calving events in regions behind the calving front. An additional factor is that the ice mélange that

forms in front of TWG can stabilise the glacier, reducing calving because of the small resistive force (back stress) (Cook et al., 2014; Herdes et al., 2012; Nick et al., 2013).

Calving events have been correlated to steady tidal forcings. For example, in Alaska, calving increased during a spring tide. The maximum tidal amplitude increases ice flexure at/near the terminus, causing increased fracturing and subsequent calving (O'Neel et al., 2003).

Investigating the immediate near terminus region of active glaciers is difficult and potentially dangerous, limiting our direct knowledge of calving and hampering the advancement of calving models (Murray, Nettles et al., 2015). TWG are not uniform at the calving front. Some glacier fronts are fully floating, forming floating ice tongues, whereas others are grounded to the sea floor. Both conditions can occur on the same glacier. Glaciers can also be lightly grounded or ungrounded at varying tidal states (D. I. Benn, Cowton, et al., 2017).

Conditions at the calving margin also significantly impact iceberg calving style. For example, longitudinal stretching at long floating ice tongues or near the grounding line can lead to the calving of tabular icebergs (Figure 2:3). Tabular icebergs are "pieces of floating ice with horizontal dimensions substantially larger than the vertical dimension" (Stern et al., 2017). Non-tabular icebergs result from buoyancy-driven calving. Upward rotation of the glacier's terminus occurs, then detachment (D. I. Benn, Åström et al., 2017). This process occurs when the glacier terminus is lightly grounded (Sergeant et al., 2019).

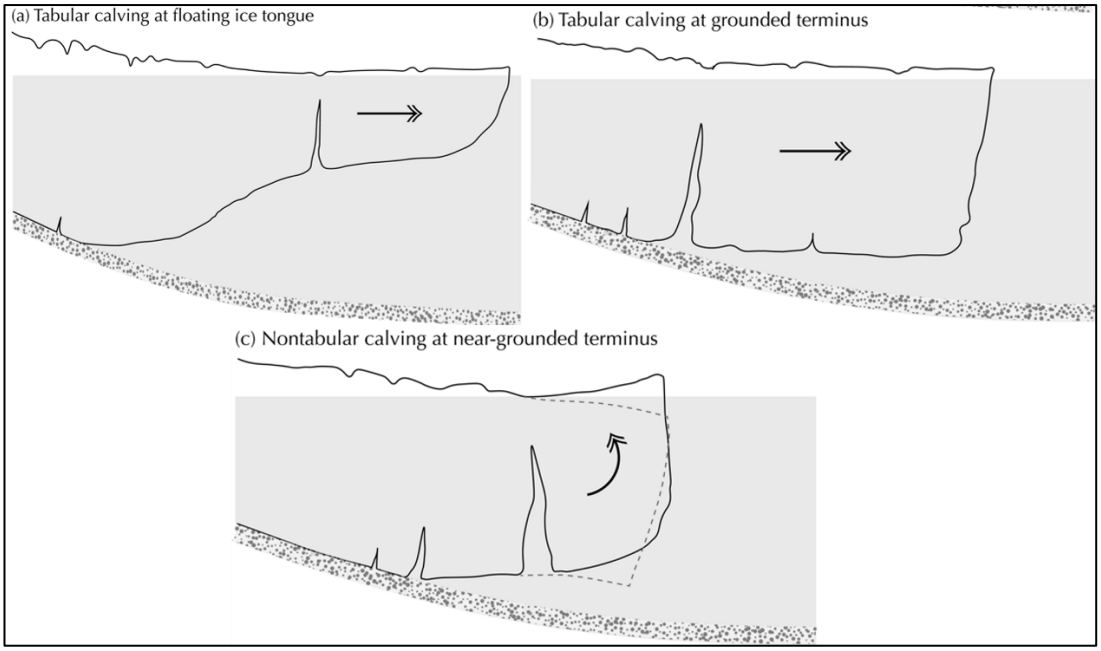

Figure 2:3, Different calving styles based on whether the glacier is ground from Sergeant et al. (2019).

2.1.2.5.2 Seasonal calving / Seasonality

There is seasonality in the rate of glacier calving at different glaciers. Working on a grounded, northern-hemisphere TWG, Luckman et al. (2015) found peak calving rates occurred in September and October, noting that frontal ablation lags air temperature and SST by 1-2 months. In a warming scenario, sea ice break-up will occur earlier, allowing longer calving seasons, causing flow acceleration, and driving glacier retreat (Cassotto et al., 2015; Walter et al., 2012). Normal glacier flow is described by periods of advance during the winter and then retreat in the summer (Schild & Hamilton, 2013). However, the long-term trend over multiple years of varying ablation and accumulation will have a dominant influence compared to a single year. For example, Jakobshavn Isbræ (Greenland) varied seasonally over 12 years (2000-2012), and the overall trend was retreat (Cassotto et al., 2015).

2.1.2.6 Fjord Termination

Glacial fjords provide the buffer zone between ice sheets and the ocean, acting as gateways for warm ocean waters to interact with and melt ice. This interaction transfers freshwater into the ocean and acts as the medium for ocean tides to modulate glacier flow (Jackson, 2010; Khan et al., 2015). Apart from submarine melting, little is known about other fjord processes (tides, local wind, shelf variability) controlling melt (Jackson, 2010). Wind-driven exchange of warm and cold waters creates circulations, bringing warm waters into the fjord and encouraging frontal ablation (Straneo et al., 2010; Walter et al., 2012). The behaviour

of TWGs is strongly modulated by the bathymetry of fjords, with narrow/shallow sections of fjords (pinning points) encouraging stability and over-deepened basins, allowing rapid retreat (Benn et al., 2017).

2.1.2.7 Glacial Earthquakes

Glacier calving can be a dramatic event and, in specific scenarios, can generate seismic waves with a large amplitude and an extended period, known as glacial earthquakes (GE) (Nettles & Ekström, 2010). They are a relatively newly recognised phenomenon, first identified in 2003 (Ekström et al., 2003). GEs are now known to occur from backwards rotating icebergs that capsize at the glacier terminus (Murray, Nettles, et al., 2015; Sergeant et al., 2019). GEs are distinct in their seismic features with a magnitude of ~5 and consist of long-period (T>30s) seismic waves (Nettles & Ekström, 2010). There are both spatial and temporal correlations between major calving events and the occurrence of GEs. Recent observations also indicate that calving events cause abrupt and persistent changes in ice flow velocity (Nettles & Ekström, 2010). For example, at Helheim Glacier, after a double calving GE event, the ice flow velocity increased by ~20% near the calving front (Nettles et al., 2008). GEs have strong seasonality, with the highest occurrence during the summer when the glaciers have retreated to their near-grounded positions. The glaciers flow faster and are also found without a stiff ice mélange (Sergeant et al., 2019). At Helheim Glacier, peak levels of GEs are seen in June-August (Nettles & Ekström, 2010). GE occurrence has quadrupled since the early 2000s; this is consistent with the acceleration of glacier flow in Greenland and the increasing number of glaciers that are in retreat and with increased calving rates (Murray, Scharrer, et al., 2015; Nettles & Ekström, 2010; Sergeant et al., 2019). A total of 8%-21% of mass loss from the GrIS could be from buoyancy-driven calving events that produce GEs (Sergeant et al., 2019), meaning that their occurrence can be used as a remotely measurable proxy for this type of mass loss. It is imperative to understand how calving impacts glacier flow because of its potential to impact the future mass balance of the GrIS.

2.2 Tides

2.2.1 Introduction

Tides are generated from the shifting gravitational effects of the Sun and Moon as their position changes relative to the rotating Earth (Parker et al., 2007). In the oceans, tides are

long waves stretching hundreds to thousands of miles long, as shown by the physical movement of water (hydrodynamics) (Parker et al., 2007).

2.2.2 Tide Range and Frequency

The difference between the high and low tide is known as the tidal range (Figure 2:4). Globally, the tidal range is highly variable from region to region. It is also locally specific (Holden, 2012). The time it takes between one high water to the next high-water event (or low-water event) is the tidal oscillation or period. Successive high tides typically occur over 12.42 hours in most parts of the world, known as semi-diurnal tides. However, there are places with daily periods (diurnal, 24.84 hours) and some specific regions with a mix (Gerkema, 2019; Parker et al., 2007). About the solar day, in a semi-diurnal tide, there are 1.932 cycles per solar day (24 hours) or about a lunar day (24.84) (Parker et al., 2007), showing the dominance of the effects of the Moon.

Many tidal frequencies occur due to various changes in the relative movement of the Moon, Sun, and Earth (Parker et al., 2007). Monthly cycles are not continuous and vary due to an array of variables. For example, there is an 18.6-year lunar cycle, which is much smaller, 5-10% of the average tidal range (Parker et al., 2007). Luckily, because of the fixed nature of the Earth, Moon, and Sun cycles, a region's tidal range and variance are predictable for years into the future with just one month of water level measurements from a gauge (Parker et al., 2007). However, due to astronomical forces, there is variance between the predicted and the observed due to many factors, including the hydrodynamics (length, width and depth of a bay river or fjord), wind (speed and direction), atmospheric pressure, water density changes from salinity to temperature changes, and glacier meltwater runoff (Parker et al., 2007).

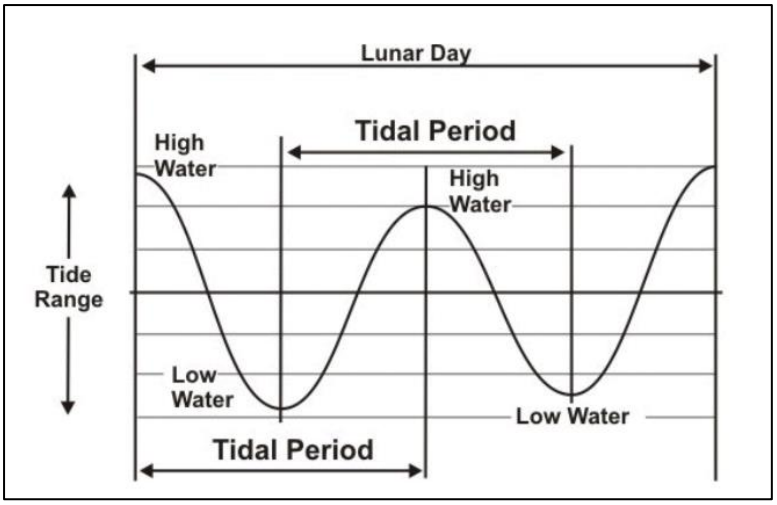

Figure 2:4, Tide curve showing the tidal period, low water and high water and the tidal range in the context of a lunar day (24.84 hours), created by Parker et al. (2007).

2.2.1 How are Tides Generated?

In equilibrium tide theory, tides are the result of gravitational forces from the Moon and the Sun, combined with centrifugal forces due to the rotation of the Earth around the Earth-Moon centre of mass, producing bulges on opposite sides of the Earth (Figure 2:5). The spin of the Earth through these bulges creates the high and low tides of moving into the bulge (high tide) and leaving the bulge (low tide) (Kvale, 2006). This simple explanation would occur if there were no continents (Parker et al., 2007).

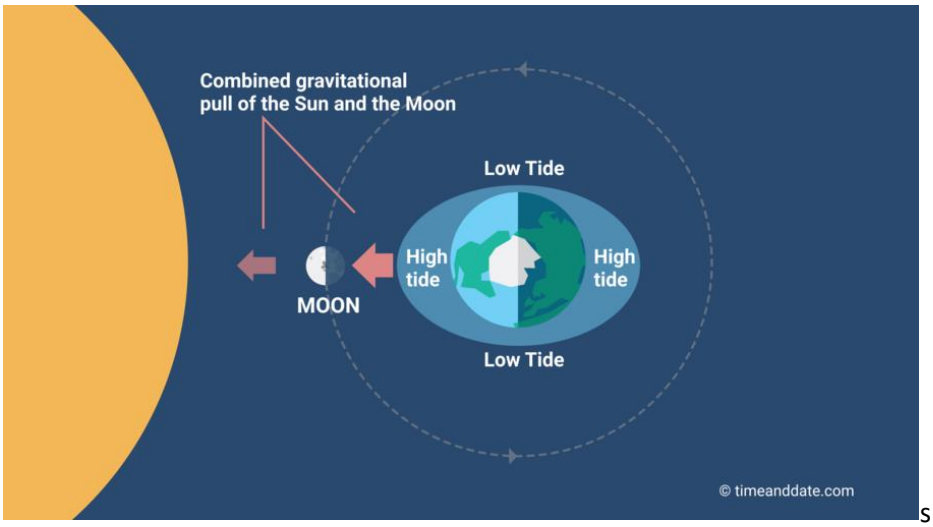

Figure 2:5, Tidal bulges are produced as the Earth spins, specifically a Spring tide with the Sun and Moon's gravitation forces working together. Accessed 22/09/2023 – https://www.timeanddate.com/astronomy/moon/tides.html

The forces in these bulges are too small to be picked up in smaller bodies of water, requiring large oceans that generate long waves with a small amplitude (< 30cm). When these long waves reach continents, the water depth falls drastically, causing the amplitude of the wave to increase (Parker et al., 2007). The tidal range depends on the natural period of free oscillation in the basin and the period of the tide-generating force. Large tidal ranges occur when the natural period of the basin is the same as the period of the tide-generating force (Parker et al., 2007), also known as resonance.

If the orbits of the Moon-Earth and Earth-Sun were circular and aligned with the Earth's equator, there would only be two main tidal frequencies: M2 generated by the Moon and S2 by the Sun. However, the distances between the Earth, Moon, and Sun change throughout the year. These changes are evident in their orbital planes, tilted relative to the Earth's equator. The Moon's orbit angle moves in a 27.32-day cycle (Kvale, 2006), while the Sun's position changes over a year, creating the Northern Hemisphere's summer and winter seasons (Parker et al., 2007).

2.2.3 Dominant Tidal Constituents

By using harmonic analysis, over 100 tidal constituents can be analysed. However, 80% of tidal variability is accounted for by only seven tidal constituents (

Table *2:1*) (Kvale, 2006). On a lunar day (24.8412 hours), two bulges cause the high and low tide twice per day (semi-diurnal tide). The largest semi-diurnal lunar harmonic is M2. It is half a lunar day, occurring 1.9323 times per solar day (Parker et al., 2007). The Earth turns under the Sun exactly once every solar day, which leads to the main solar semi-diurnal tidal constituent called S2, occurring over 12 hours with two cycles per day. Due to gravitational forces, the S2 is usually smaller than M2 (Parker et al., 2007). Spring tides occur when the Moon and Sun are aligned at new and full Moons, producing the largest tidal ranges. Smaller neap-tides occur when the Moon and Sun are in the first and third quarters working against each other (Parker et al., 200). The N2 frequency is from the effect of the 27-day variation of the Earth-Moon orbit, causing increased tidal forces (perigee) and weaker tidal forces (apogee) (Parker et al., 2007).

O1 and K1 represent the diurnal lunar tidal forces from the lunar declination. The combined minimum effect of O1 and K1 occurs every 13.66 days when the Moon is over the equator, with their maximum occurring at maximum declination. The M2 frequency is equal to the sum of O1 and K1. The movement of the Sun north and south of the equator on a diurnal

cycle, characterised by slow modulation called P1 (24.0658 hours). There is also a delay between a new/full Moon and a spring tide, called the phase age (Parker et al., 2007).

Table 2:1, Main Tidal Constituents, their speed, origin, and period in solar hours presented by Kvale (2006).

Tidal constituent	Speed σ (°/h)	Origin	Period in solar hours
M_2	28.9841	Principal lunar	12.42
S_2	30	Principal solar	12
N_2	28.4397	Larger elliptical lunar	12.66
K_2	30.0821	Combined declinational lunar and declinational solar	11.97
K_1	15.0411	Combined declinational lunar and declinational solar	23.93
O_1	13.943	Principal lunar	25.82
P_1	14.9589	Principal solar	24.07

2.3 Tidal Impact on Glaciers

2.3.1 Introduction

Tides have a varied impact on glaciers worldwide, modulating the flow of large floating ice tongues in Antarctica (2.3.4 Antarctica) and floating, lightly grounded, and grounded TWGs in Greenland (2.3.2 Greenland). Tides have also been noted to influence calving activity in Alaska (2.3.3 Alaska) and Svalbard (Holmes et al., 2023). Tidal impacts are not one-dimensional but multifaceted, varying from region to region and glacier to glacier. This section of Chapter 2 discusses tidal impacts in Greenland, Alaska, and Antarctica.

2.3.2 Greenland

Global Positioning System (GPS) measurements on Bowdoin Glacier (Figure 2:6) in Greenland found complex ice speed variations, the highest frequency being semi-diurnal (Sugiyama et al., 2015). Semi-diurnal ice speed peaks were linked with low tides close to the calving front (Podolskiy et al., 2016; Sugiyama et al., 2015). However, on 13 July 2013, heavy rainfall coincided with the fastest ice flow (Sugiyama et al., 2015) indicating many factors affect glacier flow that need to be considered. Atmospheric forcing (air temperature, precipitation) and ocean tides modulate Bowdoin Glacier's horizontal flow. The occurrence of semi-diurnal velocity changes due to low tide implies that hydrostatic pressure acting on the calving front is noteworthy in glacier speed variability (Sugiyama et al., 2015)

At Bowdoin Glacier, observations showed that the semi-diurnal flow speed variations decreased within a few kilometres of the calving front, whereas it can be over 10 km from the grounding line in Antarctica (Anandakrishnan et al., 2003; Gudmundsson, 2006; Murray et al., 2007; Sugiyama et al., 2015). This difference is thought to be due to the large swaths of floating ice in Antarctica, allowing tidal stress amplitude to propagate upstream further, compared to the ice front at Bowdoin Glacier being mostly grounded (Podolskiy et al., 2016; Sugiyama et al., 2015). The magnitude of flow speed-up was faster when low tides occurred in the evening compared to the morning at Bowdoin Glacier (Sugiyama et al., 2015). The most likely explanation is increased meltwater in the glacier bed from surface melt during the day, increasing the effect (Sugiyama et al., 2015).

Bowdoin Glacier has a relationship between ice speed and surface melt rates. Near the end of the observations, temperature correlated with ice speed, and the tidal impact on flow found earlier in the study was smaller. This likely means that basal lubrication later in the season played a dominant role in ice speed variation (Sugiyama et al., 2015). Maximum seismic activity was found on the falling tide (as flow speed increased) and near low tide (peak flow speed). Seismic events at Bowdoin Glacier are strongly correlated with the longitudinal ice stretching rate, controlled by tide height oscillations and air temperature (Podolskiy et al., 2016).

Nioghalvfjerdsbrae (79NG) is the largest of three marine-terminating glaciers fed from the Northeast Greenland Ice Stream (NEGIS) and contains enough ice to increase global sea level by 0.57m (An et al., 2021; Smith et al., 2023). 79NG has the largest floating ice tongue in Greenland at 70km long and 20km wide (Humbert et al., 2023). GPS studies at 79NG revealed a tidal signal only is present in the floating portion, with no tidal signal occurring at the grounded GPS stations (Christmann et al., 2021). The GPS data and glacier flow models showed that ocean tides modify the basal lubrication of the glacier bed ~10km inland of the grounding line.

Jakobshavn Isbrae is another outlet glacier in west Greenland, responsible for the largest source of mass loss from the GrIS in the last 20 years (Khazendar et al., 2019). Since the early 2000s, the glacier has been thinning and doubling in speed (Podrasky et al., 2014). Over 12 days in August 2009, Dual-frequency GPS receivers were deployed on the glacier with a 15-second sampling interval and processed using the GAMIT/GLOBK GPS package (Chen et al., 1998). However, the data contained “obvious outliers” (Podrasky et al., 2014). The data sets were detrended with a best-fit linear model, and data points with more than

one standard deviation from the trend were identified as outliers and excluded. After this, the position data was further smoothed to remove the influence of measurement error using a local quadratic regression filter (LOWESS) with a smoothing window of 8 data points/~2 hours. Furthermore, the position data were down-sampled to 15 minutes, using an interval-averaging routine.

Ice surface speeds at Jakobshavn are highest near the calving front and rapidly decrease upstream, with the maximum speed recorded at $48m/d^{-1}$ due to a calving event identified ~1km from the calving front (Podrasky et al., 2014). It is also noted that there is a pattern of deceleration after a calving event however flow speeds were still greater compared to before. This response has been theorised to be due to large amounts of ice loss after a calving event there is a rearrangement of the glacier geometry in the near terminus, with the fresh ice front having a larger vertical freeboard, resulting in an alteration in the stress state, favouring extensional shear stresses. Other possibilities include the suggestion that large calving events disrupt the proglacial melange causing back-stress reduction (Podrasky et al., 2014).

Tidal admittance is the amplitude ratio between the tidal force and ice speed (Walters & Dunlap, 1987). Tidal admittance at Jakobshavn Isbrae was calculated for the horizontal and vertical planes. Tide height and glacier speed were anti-correlated, during low tide there are higher surface speeds with lower speeds occurring during high tide. Tide-induced vertical motion was found to be in phase with the ocean tides. Tidally modulated variations in surface speeds were 0.4-2.9% of the background speed (Podrasky et al., 2014).

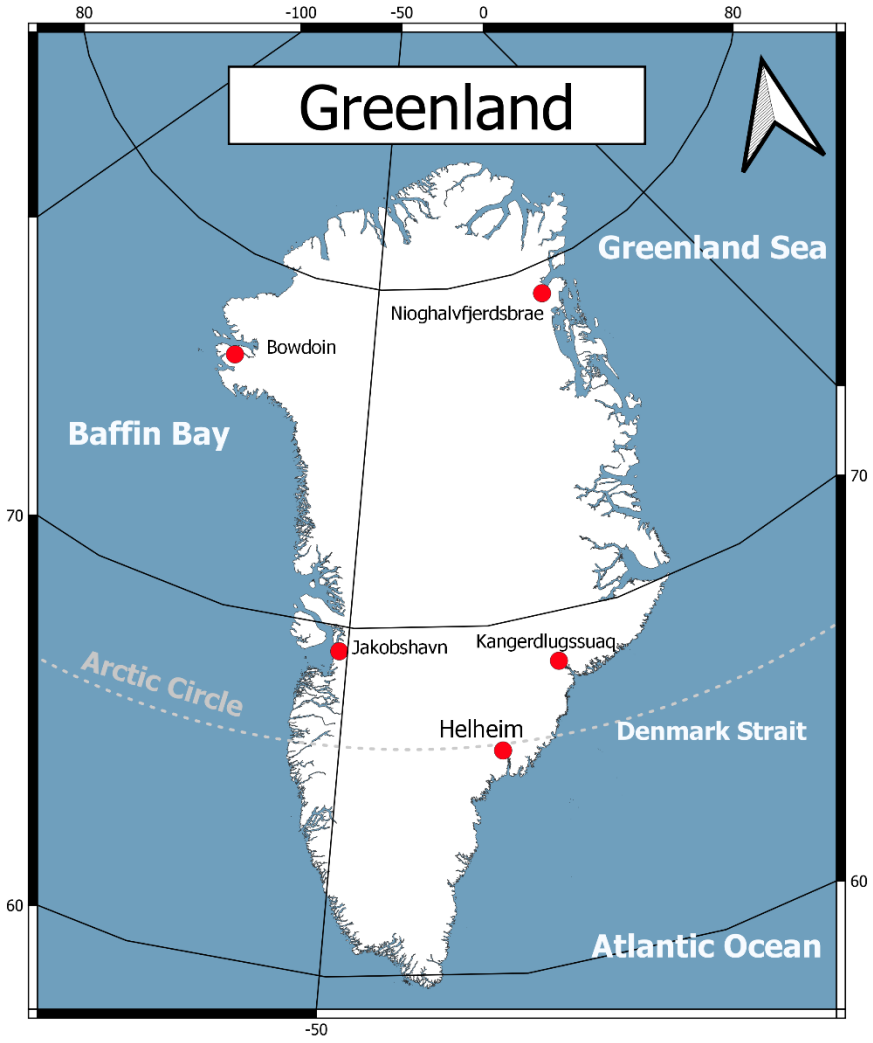

Figure 2:6, Map of Greenland, displaying the locations of Bowdoin, Nioghalvfjerdsbrae, Jakobshavn, Kangerdlugssuaq and Helheim Glacier as red dots, created using QGIS.

2.3.3 Alaska

One of the first studies to find ice flow speed varies with the tide was from Columbia Glacier (Figure 2:7) in 1980, with a tidal admittance of 0.2 m/d per metre of tide height, where the glacier has both semi and diurnal flow variations. It was also found that tidally induced speed changes dampened up Glacier (Walters & Dunlap, 1987).

At LeConte Glacier (Figure 2:7), the effect of tidal forcing is crucial because the terminus is near flotation. A strong correlation exists between calving and the fortnightly tidal amplitude of spring tides with increased calving at springs. In contrast, there is no correlation between the semi-diurnal tides and calving events. A spring tide might cause significant ice flexure at or near the terminus. Then, when this tide falls, there is a

transverse fracture due to forward bending during the fall in surface elevation, causing calving (O'Neel et al., 2003).

At Yahtse Glacier (Figure 2:7), calving events are sensitive to the semi-diurnal tide. Calving events are more likely to occur on a falling and low tide than on a rising or high tide (Bartholomaus et al., 2015). The leading theory is that the deep water in the fjord has a stabilising effect. The M2 tidal signal also correlated with peak calving activity with additional events occurring at Peak K1, O1 and Mm (Moon monthly) tidal signals (Bartholomaus et al., 2015).

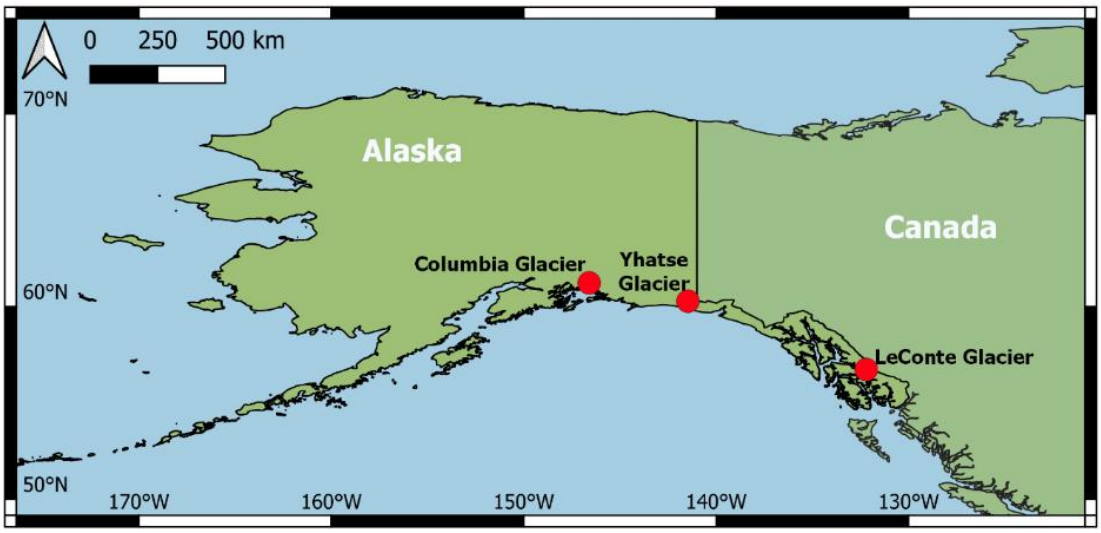

Figure 2:7, Map of Alaska and Canada, displaying the locations of Columbia, Yahtse and LeConte Glacier as red dots. All are in Alaska and created using QGIS.

2.3.4 Antarctica

In Antarctica, most ice streams and outlet glaciers flow into expansive, fully floating ice shelves, enabling the grounding lines to interact with ocean tides (Anandakrishnan et al., 2003). In Antarctica, tides modulate flow in many forms, from daily flow modulation in the Bindschadler Ice Stream (Thomas, 2007), fortnightly variations at the Rutford Ice Stream (Gudmundsson, 2006), horizontal velocity modulation of the Brunt Ice shelf (Doake et al., 2002). Furthermore, variations can be slowly varying (e.g., Rutford Ice Stream (Gudmundsson, 2006; Murray et al., 2007)), but stick-slip motion has also been observed at Whillans Ice stream (Winberry et al., 2009) (Figure 2:8).

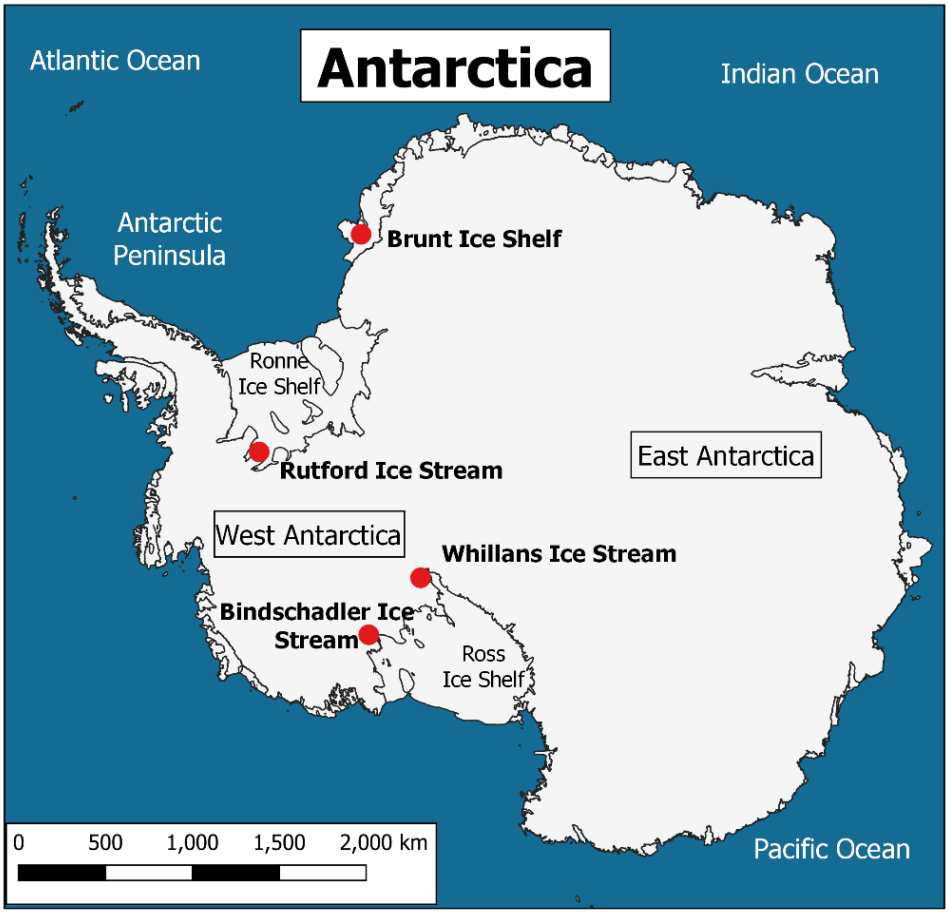

Figure 2:8, Map of Antarctica, displaying Ice Streams and Shelves described in the Literature Review and their locations highlighted with a red dot, created using QGIS.

2.3.4.1 Daily Flow Modulation – Bindschadler Ice Stream (Ice Stream D)

At the grounding line of Bindschadler Ice Stream (Figure 2:8), formally called Ice Stream D (Sergienko et al., 2008), the flow was shown to slow during the rising tide and increase during the falling tide by ~50% (Thomas, 2007). As a result, the velocity at the grounding line fluctuates by ±0.7 m/d^{-1} compared to a mean flow speed of 1.2m/d^{-1}. However, the tides are not synchronous with flow velocity, and there is a significant time lag on the Bindschalder Ice Stream of ~6 ±1 hours from high tide to peak flow velocity. The same modulation occurs during low tide, meaning the Bindschalder Ice Stream is 6 hours out of phase with the ocean tides (Anandakrishnan et al., 2003).

2.3.4.2 Fortnightly Tidal Variations – Rutford Ice Stream

On the Rutford Ice Stream (Figure 2:8), surface velocities vary by about 20% over a fortnightly cycle because of tidal forcing (Gudmundsson, 2006; Murray et al., 2007). Flow velocity increases leading up to a spring tide and then decreases until neap tides, suggesting that peak-to-peak changes in the semi-diurnal tide are related to velocity

changes (Gudmundsson, 2006; Murray et al., 2007). One explanation could be that tidal-induced elastic stress changes the ice stream's basal shear stress distribution. Due to the nonlinearity, a positive change in shear stress is more significant than a similar negative change in shear stress over a tidal cycle. The net imbalance in stress results in an additional forward displacement (Gudmundsson, 2006). It has been proposed that periodic grounding of the ice shelf is the primary driver in translating the vertical tidal motion into horizontal flow (Minchew et al., 2017; Zhong et al., 2023).

The maximum forcing of the ice shelf is at the semi-diurnal frequency; however, the velocity response of the 2-weekly and semi-annual forcing is 30-50 times more sensitive, meaning the impact of flow speed is greater than the amplitude of these long-term variations. At other tidal frequencies, the ice stream flow speed also has little energy, indicating that other forcings that modulate velocity do not notably contribute, like the inverse barometer effect where low pressure causes relative sea level rise, or high pressure causes a drop (Murray et al., 2007; Padman et al., 2003; Wendt et al., 2004).

2.3.4.3 Horizontal Velocity Variation – Brunt Ice Shelf

The western part of the Brunt Ice Shelf (Figure 2:8) flows at ~800 m/yr^{-1} (De Rydt et al., 2019; Thomas, 2007). The horizontal motion of the Brunt Ice Shelf is affected by ocean tides. There are many theories explained by Doake et al. (2002). One leading theory explains this through frictional drag caused by ocean currents or interactions at the grounded zone on the ice front. The average forward velocity would change from 50-100% because of tidal modulation, with maximum forward velocity occurring four hours before maximum tide height. Another theory suggests that a sloping contact with the rumples pinning the ice shelf allows the shelf to move with the tide as it rises and falls, turning vertical motion into horizontal. However, due to data collection methods, it was not possible to distinguish between different theories (Doake et al., 2002).

2.3.4.4 Stick-Slip Motion – Whillans Ice Stream (West Antarctica)

2.3.4.4.1 Introduction to Stick-Slip Motion.

Flow on the Whillans Ice Stream (WIS) (Figure 2:8) is not constant and has stick-slip motion variability (Winberry et al., 2009), characterised by two phases. Firstly, the stick phase, a quiescent period associated with slight motion and a build-up of stress. Secondly, the slip-phase. When the stress during the stick phase increases, the glacier reaches a point where the pressure is released, resulting in a higher flow rate (slip phase). The extreme speed variations could indicate a non-linear ice stream bed (Bindschadler, Vornberger, et al., 2003;

Winberry et al., 2009). In laboratory experiments, frictional instabilities associated with the rheology of the sliding interface cause stick-slip motion (Winberry et al., 2009).

2.3.4.4.2 Stick-Slip Motion Explained on Whillans Ice Stream.

Computer models simulating the stick-slip motion of WIS showed that if there is no tidal cycle, slip events would occur every 12 hours. However, the tidal amplitude disturbs this theorised regularity (Bindschadler, King, et al., 2003). By adding tides into the computer model, the series of slip events and their timings closely matched observations (Bindschadler, King, et al., 2003). A tidally modulated stress regime can explain flow variability on the WIS. There is healing during the quiescence (stick), strengthening the bed, allowing stress to accumulate at lower flow rates, leading to larger intervals between slip events. Longer low rates of stress build over time, leading to more significant slip events (Winberry et al., 2009). A 1 m increase in sea level from tidal forces substantially increases the effective normal stress and is sufficient to cause motion events (Bindschadler, Vornberger et al., 2003). At high tide, the normal stress from the till releases (Bindschadler, Vornberger, et al., 2003). The non-floating portion of an ice stream experiences higher pressure, causing fluctuations in the stress regime (Winberry et al., 2009). During a falling tide, if the tidal flow is parallel to mean ice motion, net basal stress increases to such an extent that it releases the accumulated stress over the ice plain. Lower magnitude slip events occur on fast-falling tides because there is less time for shear stress to accumulate. With a rising spring tide, there is a low accumulation rate of net shear stress, allowing the ice stream to heal over time. More shear stress is required to induce failure when healing occurs, inevitably leading to prominent slip events (Winberry et al., 2009). More research into the causes of stick-slip motion is required for further understanding, including in-depth basal rheology analysis alongside flow analysis with precision to seconds to reveal the initiation of an event.

2.4 Helheim Glacier

2.4.1 Introduction

Helheim Glacier (Figure 2:9 and Figure 2:10) (66.38˚ N, 38.8˚ W) is one of the largest TWG in Greenland concerning ice discharge and total area of ice sheet drainage (Miles et al., 2016). The actual ranking of the largest glaciers in Greenland is up for debate. Rignot et al. (2004) believe Helheim Glacier was the 3rd largest, whereas Enderlin et al. (2014) notes Helheim

Glacier as the 5th largest. The changes in ranking are due to the temporal sampling differences between studies (Miles et al., 2016). The total ice discharge through Helheim Glacier is also variable. Murray et al. (2015) report that Helheim Glacier drains 52,000 km^2 of ice from GrIS, whereas others have noted 48,000 km^2 (Straneo et al., 2016). South of Helheim Glacier is a town called Tasiilaq (Figure 2:9). This town has allowed researchers easy access to the glacier. As a result, Helheim Glacier has been a crucial glacier in multiple ground-breaking studies (Jackson et al., 2014; Juan, 2011; Nettles et al., 2008). Helheim Glacier drains 4-7% of the GrIS through a 6km wide calving margin (Murray, Selmes, et al., 2015; Rignot & Kanagaratnam, 2006; Schild & Hamilton, 2013; Straneo et al., 2016) that is grounded in ~600m of water, terminating into Sermilik Fjord ~100 km away from the ocean (Straneo et al., 2010, 2016; Straneo & Heimbach, 2013).

The region surrounding Helheim Glacier receives some of Greenland's highest levels of snowfall, >1 m/yr (Burgess et al., 2010). Helheim Glacier has gone through periods of thickening and thinning. One cause of this is the sensitivity to temperature changes. Helheim Glacier reacts to slight deviations in sub-surface water temperature (SSWT) and air temperature (Khan et al., 2014). Recently, the ice discharge rate at Helheim Glacier has started to increase. In 2018 the solid ice discharge surpassed the largest glacier in Greenland, Jakobshavn Isbræ (Joughin et al., 2004; Mankoff et al., 2020). Helheim has experienced significant changes in velocity and elevation. These are thought to be from its sensitivity to the terminus position and calving (Kehrl et al., 2017). Past research has also shown that basal lubrication from surface melt plays a role (Stevens et al., 2022).

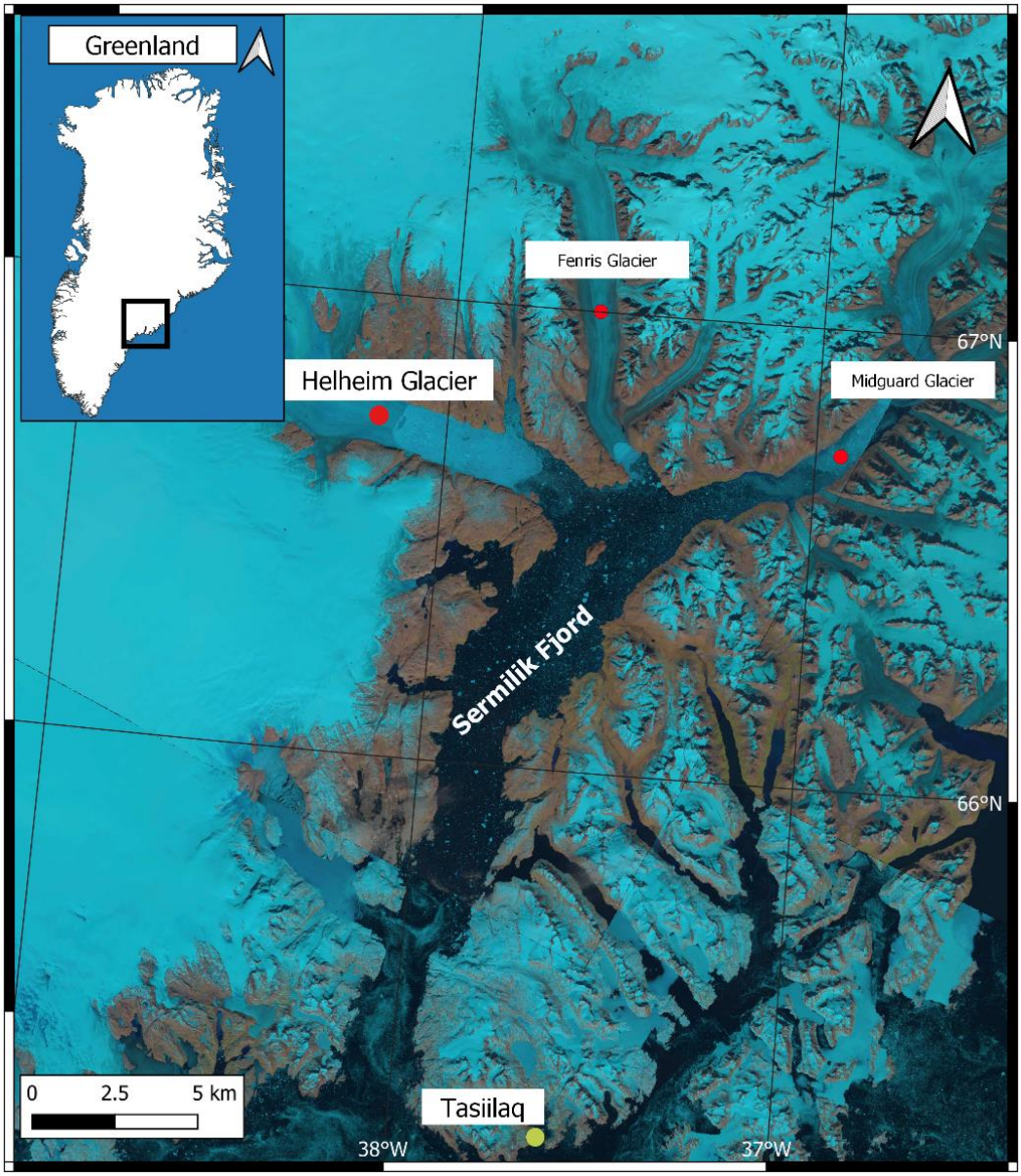

Figure 2:9, Sermilik Fjord and the Glaciers feeding into it (red dots) highlighted in Green is the Town of Tasiilaq (green dot), with an Inset map (top left) showing the location relative to Greenland.

2.4.2 Sermilik Fjord

Helheim Glacier terminates into Sermilik Fjord, alongside Fenris and Midgard (Figure 2:9), two smaller and shallower glaciers that drain only a fraction of the ice sheet. As a result, Fenris and Midgard have been studied less extensively than Helheim Glacier (Vaňková & Holland, 2016). There is no sill (shallow regions commonly occupying the mouth of a fjord (Shoemaker, 1986)) near the front of Helheim Glacier or at the mouth of Sermilik Fjord (An et al., 2019). South of 66°N, the fjord is 800 m below sea level and flat, indicating large

amounts of sediment deposition in the past. North of 66°N, the fjord bed is 600m below sea level (An et al., 2019).

Sermilik Fjord is U-shaped, 100km long, with connections to temperate Atlantic waters from a branch of the Irminger Current, a section of the North Atlantic Current (NAC) (Straneo et al., 2010; Vaňková & Holland, 2016). In the past ~20 years, Sermilik Fjord has been a pivotal area of interest (Straneo et al., 2010; Sutherland et al., 2013). Research has revealed that warm subtropical salty water enters the subpolar basin from the NAC (Straneo et al., 2010), the warm water flows beneath the cold fresh East Greenland current and circulates deep in the fjord (Miles et al., 2016; Våge et al., 2011). The fjord depth varies from 600-900 m. At the surface, temperatures reach ~1°C at 200-600 m below sea level, and temperatures have been recorded as high as ~4°C (Miles et al., 2016; Straneo et al., 2010) and attributed to warm subtropical salty water entering the subpolar basin meeting cold fresh water from the East Greenland Current. The warm water flows beneath the cold fresh water and circulates deep in the fjord (Miles et al., 2016; Straneo et al., 2010; Våge et al., 2011), exposing Helheim Glacier to warm water year-round (Johannessen et al., 2011). The warm water found in fjords causes undercutting of the calving front, leading to enhanced calving rates (Luckman et al., 2015; Motyka et al., 2003; O'Leary & Christoffersen, 2013). Sutherland and Straneo (2012) estimated Helheim Glacier's submarine loss rate at 650 m/yr, equating to ~1.8 m/d^{-1} (Murray, Selmes, et al., 2015).

2.4.3 Helheim Glacier's Mass Balance

Pre-2000s Helheim Glacier's mass balance was positive, gaining ~4 km^3 of ice/year (Rignot & Kanagaratnam, 2006). During the early 2000s, GrIS experienced record ice mass loss (Andresen et al., 2012). As a result, over the past 20 years, Helheim Glacier has seen significant variations in its frontal position. In 2001, Helheim Glacier was stable, by 2003, the ice front had retreated 3.25 km, with an additional ~2 km retreat occurring in the summer of 2004 attributed to multiple calving events (Joughin et al., 2008). In 2005, Helheim Glacier accounted for 5% of GrIS's total mass loss (Rignot & Kanagaratnam, 2006). That year was recognised as the most retreated position on record (Figure 2:10) (Murray, Selmes, et al., 2015). Helheim Glacier was in a state of negative mass balance, losing ~12 km^3 of ice/per year (Rignot & Kanagaratnam, 2006). In this same 5-year period, flow speed increased from 22 to 30 m/d^{-1}, and the retreat of the calving position totalled 7.5 km (Howat et al., 2005). This extreme mass change was not isolated, with many Greenland glaciers also experiencing exceptional retreats (Cook et al., 2014). Many researchers have

hypothesised that this was caused by a singular environmental event, caused by high air and sea temperatures (Joughin et al., 2008; Murray et al., 2010). By 2006, Helheim Glacier flow speed fell by ~30%, becoming more stable (Murray et al., 2010). Since the readvance in 2007, the terminus position has fluctuated ~5 km (Cheng et al., 2022). From 2014-20, Helheim Glacier experienced an acceleration of 2.5-3 km/yr^{-1} near the terminus, accompanied by a 4 km retreat (2014-19), surpassing 2005. These retreats were somewhat seasonal, as some readvancements occurred during some winter seasons, with one outlier during the 2014/15 winter when no readvancement was recorded (Williams et al. 2021).

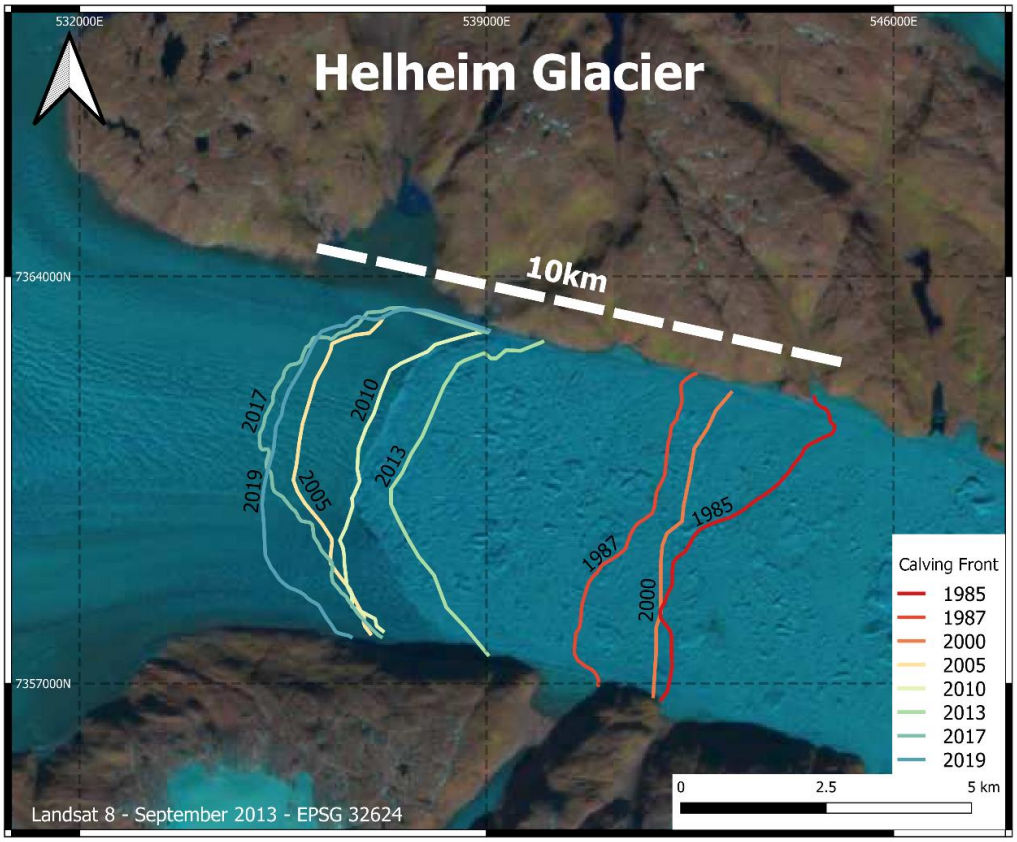

Figure 2:10, Helheim Glaciers varying calving front positions. The 2013 position is ~2km advanced from the 2005 position.

2.4.4 Helheim Dynamics

2.4.4.1 Present Flow

Fortunately, because Helheim Glacier is of high research interest, we have an accurate and good understanding of flow speeds. Vijay et al. (2019) used Sentinel-1 IW-based synthetic aperture radar intensity offset-tracking to calculate surface velocities, noting that Helheim Glaciers average flow speed equated to 6,782 m/year, equivalent to ~19 m/d^{-1}. Using GPS data in 2007, Nettles et al. (2008) state that flow speed at the calving front can be ~25 m/d,

whereas further up the glacier, the flow slows (~12 m/d). The slowest recorded velocity is ~10 m/d, occurring in the middle of the glacier located in a region of Helheim Glacier with a topographic bend, which could increase stress and inhibit flow (Nettles et al., 2008). Helheim Glacier has velocity variations of ~5% due to surface melt fluctuations with a lag of ~1 day (Andersen et al., 2010). Variability in water input drives the dynamic switching between subglacial channels and cavities, causing glacier acceleration (Schoof, 2010; Voytenko et al., 2015).

2.4.4.2 Past Flow

By analysing sedimentary deposits in Sermilik Fjord Andresen et al. (2011) generated a record of calving activity for Helheim Glacier extending back to ~AD1890. The analysis identified that around the 1930s-1940s, Helheim Glacier experienced a period of extended calving activity. During this time, there was a positive phase of the Atlantic Multi-decadal Oscillation combined with low polar-water export, and the period also experienced high summer temperatures. A mixture of these variables likely caused submarine and surface melt increases, producing increased mass loss at Helheim Glacier (Andresen et al., 2012). During the 1990s, Helheim Glaciers' speed and front fluctuations remained small (Luckman et al., 2006). Abdalati et al. (2001) theorised that the maximum thinning rate at the terminus was ~2 m/yr. From 1986 to 1995, the average speed was ~15 m/d. In the early 2000s, flow speed increased to 20-30 m/d, approximately doubling (Bevan et al., 2012; Luckman et al., 2006). Helheim Glacier reached its peak position during the Little Ice Age. Since then, there has been thinning and retreat. Using aerial imagery from the 1930s onwards reveals periods of retreat and advance. These periods have been correlated with fluctuations in atmospheric and oceanic temperatures (Khan et al., 2014, 2015).

2.4.5 Calving at Helheim Glacier

Calving at Helheim Glacier is not seasonal, occurring year-round, in direct contrast with Kangerlussuaq Glacier (Murray et al., 2015). An ice mélange is also usually present in the fjord surrounding Helheim Glacier, created by calving (Schlemm & Levermann, 2021; Vaňková & Holland, 2016). Many mechanisms are at play that induce calving. In the 2013 summer, calving was correlated with buoyant flexure mechanisms caused by ungrounded ice rotating upward. Calving events can also significantly impact glacier velocity in varying time scales from minutes to hours (Nettles et al., 2008; Ultee et al., 2022).

2.4.6 Tides at Helheim Glacier

Previous observations in Sermilik Fjord found ocean tides are predominantly semi-diurnal with a fortnightly modulation (~3 m spring and ~1 m neap tide) from M2 and S2 (Juan, 2011). During the summer (2006-2008), the near terminus ice flow velocity averaged ~25 m/d (Juan, 2011; Voytenko et al., 2015). If there is a vertical response to the tide, these regions are thought to be floating (Juan, 2011). Floating regions show a ~30-40% modulation in the vertical position compared to the tidal range (Juan, 2011). When comparing mean flow speed, Helheim Glacier advances at low tide, then delays at high tide (Juan, 2011; Juan et al., 2010). When Helheim Glacier is floating, the tidal amplitude is greater at the front, reducing further up the glacier. The detachment of the glacier tongue reduces friction and is vital in modulating the tidal response. Admittance analysis shows an hour variation in response to tides, depending on whether the glacier was afloat (Juan, 2011).

Individual tidal constituents have been analysed on Helheim Glacier, finding diurnal variations in glacier flow and evidence for glacier position being in phase with S1; this is a solar diurnal tide occurring once per day. It is driven by the daily variation in insolation (Davis et al., 2014; Ray & Egbert, 2004). Other studies have found that Helheim Glacier moves in and out of phase with the semi-diurnal tides (Voytenko et al., 2015).

Flow at Helheim Glacier depends on the rate of applied stress controlled by the tidal period. During high tide, Helheim Glacier's speed decreases by ~10% (Voytenko et al., 2015). Theoretically, a semi-diurnal tide has a large amount of applied stress compared to a diurnal tide, which could significantly affect glacier dynamics because of its larger amplitude. Bartholomaus et al. (2007) theorised that Greenland TWGs, like Helheim Glacier, could have a linked cavity system. The increased strain from glacial earthquake speeds up increased basal water pressure due to the reduced water storage capacity in the subglacial channels, enabling an enhanced glacier response to the tides due to increased basal lubrication, lasting a few days with flow variation settling down again (Juan, 2011; Voytenko et al., 2015).

2.4.7 Conclusion

Helheim Glacier is a well-known and extensively researched glacier located in Greenland. Over the years, researchers have studied the glacier's various regimes, including periods of slow and fast flow and the impact of tides on its flow. However, previous studies have not used an extensive GPS network to explore the glacier's behaviour. For instance, Davis et al.

(2014) only used one GPS logger and found that Helheim Glacier was in phase with the S1 tidal signal. Juan (2011) used GPS data over three summers each summer with a varying number of GPS nodes from 12-28 overall, covering 1-30km behind the calving front. The current study aims to provide more detailed insights into the tidally modulated flow and its impact right up to the moment of calving through the use of GPS building upon the work presented by Tavi Murray (Martin et al., 2014; Murray, Nettles, et al., 2015; Murray, Selmes, et al., 2015).

Chapter 3 – Methodology

3.1 Introduction

To study how tides impact glacier flow in detail a significant amount of high-quality data is required. Many academic institutions have helped and contributed by providing data and experience to this study. Newcastle University and Swansea University designed and deployed a Wireless Network of GPS nodes in the Summer of 2013. 20 GPS nodes were placed on Helheim Glacier across the calving front (Figure 3:1). Tide gauge data for the same period are from Fiammetta Straneo (University of California, San Diego). All data manipulation and visualisation have been undertaken with Python, a high-level, general-purpose programming language and Qgis (QGIS Development Team, 2009; Van Rossum & Drake Jr, 1995). Both are free-to-use software built to solve a broad spectrum of problems. All code written is available as a GitHub repository (https://github.com/Jcolinese). The following Methodology Chapter is split into two sections. The first section outlines how the data was collected before this thesis and the GPS network (3.2 Previous Work). The second section details the new work and current methods for this thesis (3.3 Current Work).

3.2 Previous Work

The following data has not been collected as part of this thesis and was collected before this thesis started or was produced by other third parties to aid in this thesis.

3.2.1 GPS

The GPS network consisted of 20 on-ice transceiver nodes (Figure 3:1) and four logging base stations (Martin et al., 2014). 2.4GHZ Zigbee transceivers, designed for hostile radio frequency environments, were used, providing a low-cost and powerful wireless network. Each node was powered by solar panels and backup batteries, allowing a continuous recording during cloudy days and night-time at a high resolution because dual frequency GPS equipment can produce position data every second with an accuracy of 1-2 cm in plan and 2-5 cm in vertical (Martin et al., 2014).

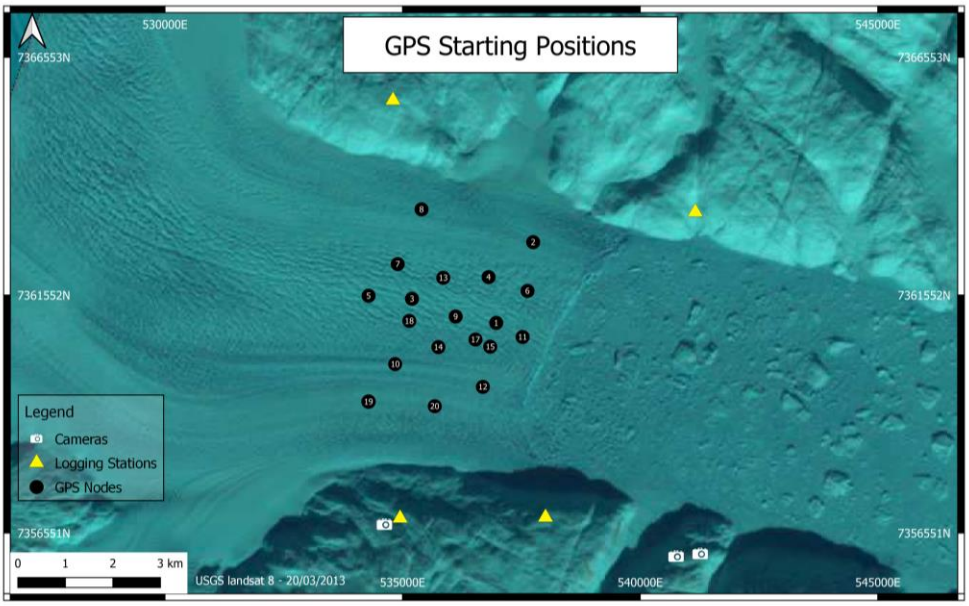

Figure 3:1, Starting positions of the GPS Nodes. Underlay is an image taken by Landsat 8 on 20 March 2013 from USGS Earth Explorer. The Grid is EPSG:32424, WGS 72BE/UTM zone 24N, in meters. Also shown is the location of the logging stations and the field cameras.

Every few seconds, GPS data received from the nodes were transmitted through the Zigbee Transceivers to logging stations located on the nearby bedrock adjacent to Helheim Glacier (Figure 3:1), where they stored the raw data, ready for further processing. The effectiveness of this system was designed post-field trials in 2012 when a smaller network was trialled. During the 2013 season, the GPS nodes were deployed between 11–15 July (day of the year (DOY) 192 and 196). Nodes that survived the whole season were retrieved on 28th August (DOY 240) (Murray, Selmes, et al., 2015). Over 7 million raw GPS position data epochs were recorded, with an observation interval for each node of ~4-7 seconds. Ice node positions were estimated using Track (GAMIT v10.5) carrier phase relative positioning from the GAMIT-GLOBK10.50 GPS Processing software created by Chen et al. (1998).

Of the 20 Nodes, all but one (Node 16) worked, with only 5 surviving the entire season. During the field trials in 2012, it was common for ice nodes to lose their line of sight between the logging stations caused by ice pinnacles as the node moved down the glacier (Martin et al., 2014). To solve this problem, four logging stations were placed on the bedrock, two on each side of the glacier. To avoid data transmission collisions, every node independently transmits to two logging stations, dividing the 20-node network into 5-node subnetworks. Usually, Zigbee transceivers avoid transmission collisions using carrier sense multiple access. However, due to the highly crevassed surface, the nodes can become shielded from each other (Murray, Selmes, et al., 2015). Data collisions within the

subnetwork were therefore avoided through a round-robin scheme, where, in turn, each subnetwork polled each node with a message, with the node replying with its GPS Position.

3.2.2 Calving Events

Calving events have been identified in two manners: using seismic data and hourly photography of the calving front. The advantage of using two forms of detection is that one provides the precise timing of iceberg calving and the other allows identification of the region of the glacier affected and estimation of the volume calved (Murray, Selmes, et al., 2015).

3.2.2.1 Cameras

Cameras were installed on the bedrock (Figure 3:1), capturing photos of the glacier front every hour. External timers were synchronised manually, starting on DOY 194 or 196 and ending at DOY 245 (13/ 15th July to 2nd September). Shortly after the field research, a visual inspection of the photos allowed the identification of calving events. The calving events are identified through "large movement of the mélange floating on the fjord…but also changes in the calving front itself" (Murray, Selmes, et al., 2015). With the date recorded from the cameras, we have an hour time frame of when a calving event has occurred.

3.2.2.2 Seismic Data

The second form of calving identification comes from the use of seismic data. Data from the Global Seismographic Network (GSN) were used to determine the timing and origin of GEs. There are two sets of seismic data. Firstly, the original inspection and then a secondary inspection of the GSN array stacks identified smaller GEs not detected in the original algorithm (Murray, Selmes, et al., 2015). These data sets are combined to try and provide an extensive log of possible GEs and calving events. Data from the GSN provides more accurate timeframes for events, as seismic data is not limited to hourly changes like the camera identification method.

3.2.3 Tidal Gauge

Before any tidal analysis can be carried out, a complete understanding of the tidal regime in the Sermilik fjord is essential. In 2011, a pressure gauge was fitted by Fiammetta Straneo (University of California, San Diego), lasting ~3 years, being recovered on 23rd August 2013. The pressure gauge (SF3_10) was deployed south of Helheim Glacier at a depth of ~15m (Figure 3:2). This dataset provides ample data to extract the tidal constituents and predict

future tidal regimes; however, it is located ~23 km in a straight line from Helheim Glacier (Figure 3:2).

3.2.4 Supplementary Data

Some other Supplementary data have been accessed from many sources. Precipitation data is freely available from the Danish Meteorological Institute (DMI) (https://www.dmi.dk/publikationer/). The data was recorded from the nearby town of Tasiilaq (Figure 3:2).

Air temperature data from Tasiilaq, located approximately 55 miles from Helheim Glacier, is available through the Danish Meteorological Institute (DMI). This thesis has managed to access data from an Automatic Weather Station (AWS) positioned next to Helheim Glacier (Figure 3:2) from Michael Shahin (PhD candidate, University of Kansas).

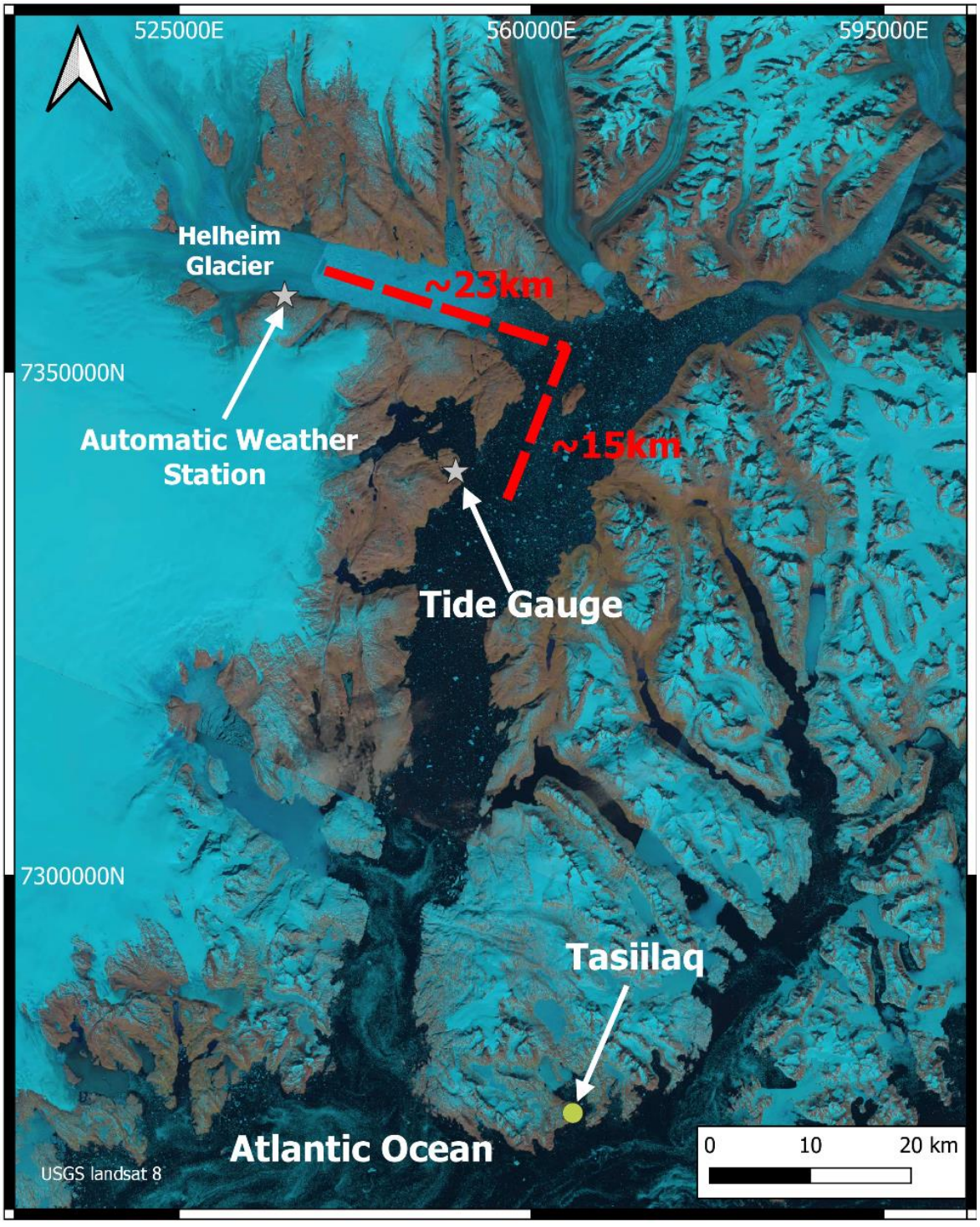

Figure 3:2, Location of the tide gauge, deployed by Fiammetta Straneo (University of California, San Diego) in 2011 and recovered in 2013. Furthermore, Michael Shahin (PhD candidate, University of Kansas) provided the Automatic Weather Station. The coordinate system is EPSG:32424, WGS 72BE/UTM zone 24N, in meters.

3.3 Current Work

The following methodology has been developed directly for this project.

3.3.1 Filtering GPS

GPS data can be inaccurate even before operating in harsh and extreme environments. Many factors cause positioning errors from ionospheric and tropospheric effects, shifts in satellite orbits or calculation and rounding errors (Nyen Thin et al., 2016). Nevertheless, dual-frequency GPS equipment can be highly accurate (Martin et al., 2014). The recorded GPS data have a sampling interval of 4-7 seconds but are not clean as they contain a considerable amount of noise. To combat these, two approaches are used to clean the data (outlined in 3.3.1.1 GPS Pre-Processing and 3.3.1.2 Kalman Filter), enabling the investigation of long-term trends. The two approaches are to remove "bad" data based on statistical variance and smooth the remaining data using a Kalman Filter (KF). A full-flow diagram of the data filtering from the original to the final data set can be seen in Figure 3:8.

3.3.1.1 GPS Pre-Processing

All GPS data are first cleaned based on three factors (Table 3:1). The three factors create a minimum standard of quality every data point must reach. If a piece of data does not meet the criteria of all three variables, it is removed (Figure 3:3). Removing this noise allows better identification of the longer-term trends of the GPS data, allowing the identification of tidal signals that are constantly occurring but are not evident with the noisy variable data.

GPS nodes take observations from multiple satellites to calculate their position. If you take two receivers observing the same satellite and subtract their observation from each other, you remove satellite-related errors/bias. Double difference builds on this by subtracting the observation of one satellite from another, reducing receiver-related errors (Sanz Subirana et al., 2013). For this thesis, the number of double difference calculations acts as a proxy for the number of satellites in view of the GPS node. The more satellites a node is in view of, in theory, increases the accuracy of the measurement. So, any data points with less than four satellites in view are identified as less accurate because a minimum of 4 satellites is required to ensure there is minimised degradation and a robust measurement (Zhang & Zhang, 2009).

A bias that double difference removes is the fractional part of the phase observation, meaning there is an integer number of waves. If these integers can be identified during processing, the resulting position observations are significantly more accurate (Sanz

Subirana et al., 2013). During GPS processing, an attempt to find these integer values is made through a carrier phase ambiguity-fixing procedure (Sanz Subirana et al., 2013). If these integer numbers cannot be found, the observations are not as accurate and are called unfixed biases. We want to keep these inaccuracies to a minimum; therefore, a maximum value of 2 has been chosen.

Lastly, the standard deviation of height has been used to remove any data point where the value is greater than 0.1m (10cm). This is because the GPS data has an accuracy of 2-5cm in height giving a good buffer to ensure poor data is removed and any other variations in height not caught can be filtered by the Kalman filter.

Table 3:1, The three data cleaning variables used. If a data point falls within all these variables, then the data is kept.

Unfixed Biases	<=	2
Double Differences	>=	4
Standard Deviation of Height	<	0.1m

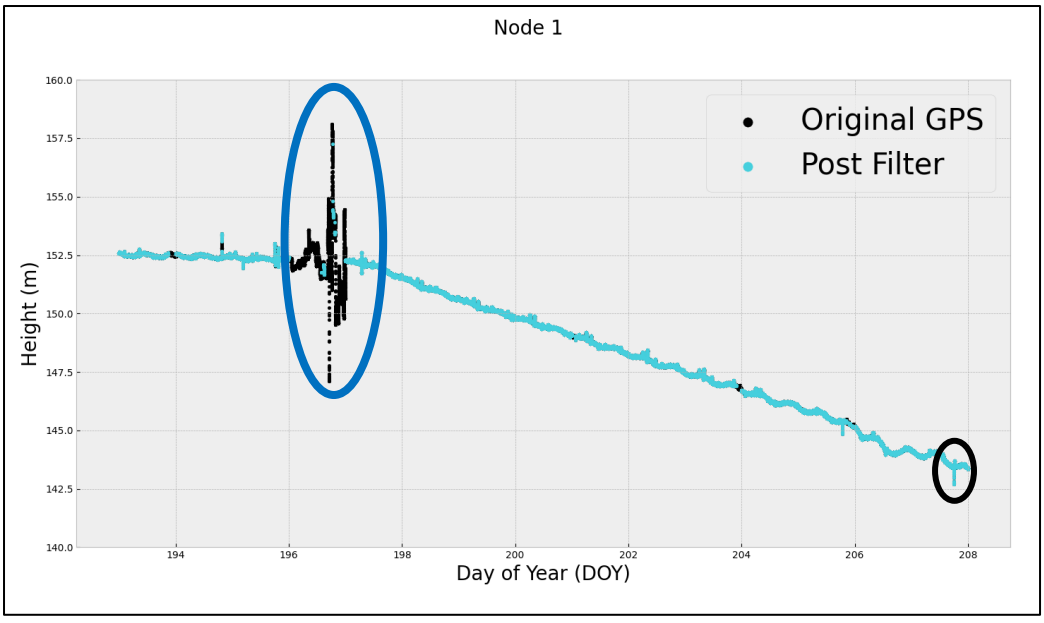

Figure 3:3, Original GPS Data from Node 1, Original GPS data (black) and Post filter (light blue), based on the variables described in Table 3:1. Circled in blue is a significant portion of time identified as incorrect/noisy. Circled in black is a portion of data that needs to be further filtered.

3.3.1.2 Kalman Filter

A Kalman Filter (KF) provides the best estimate of the GPS position, using prior knowledge to predict the past, present, and future state (Chadaporn et al., 2013). It is an algorithm containing a set of mathematical equations providing an efficient way to estimate the state of the GPS data, minimising the mean squared error (Thomson & Emery, 2014; Welch & Bishop, 1995). The functions are to measure, update and predict the GPS Position. The KF incorporates statistical noise and measurement inaccuracies (Kalman, 1960) and has extensive use in the field of navigation (Pearson, 2018).

One of the bBenefits of the Kalman filter is the extreme levels of customisation. You can produce robust data and tailor each data set to achieve the best results. Working with Dr. Christopher Pearson (Newcastle University) on coding the Kalman filter, many ad-hoc approaches have been taken to speed up the process of producing a "good enough" data set. The full code used is available via GitHub. Filtering is always a subjective approach, and the level of filtering depends on the goal of the data investigation. For this Thesis, we were looking to achieve good general filtering keeping in short-term variations in GPS position that came about from calving events whilst also removing lots of noise to reveal the semi-diurnal variations. This also had to apply to 19 individual datasets collected from various regionsdifferent parts of the glacier. Different parts of the glacier experienced different conditions from being at the calving front where the sensor could fall off or crevasses open to being positioned further up the glacier with more stable flow and fewer variations in conditions.

The Kalman filter was also chosen to filter this data set because it is an opportunity to test and try different approaches to filtering GPS Data (other methods include Least Squared Filtering and a 5-point moving average). The Kalman Filter has been widely used in the field of GNSS. Once you have collected the raw Phase data you need to estimate the three-dimensional relative positions of ground stations and satellite orbits alongside other parameters (M. Floyd, 2023). Using **GAMIT** ("**G**NSS **a**t **MIT**") then **GLOBK** ("**Glob**al **K**alman Filter"). Working together with Christopher Pearson (Newcastle University) we designed a simplified version of a KF that allowed the use of real-life constraints on the data with variables that allowed us to increase the filtering to the desired level.

GPS data have three positions: Easting, Northing and Up (ENU). When applied to the correct grid reference (EPSG:32424, WGS 72BE/UTM zone 24N). The position of the GPS node in time can be displayed and analysed like coordinates on a map (Figure 3:1). Some KF will use

all three positions combined (ENU) to calculate one 3-dimensional position. However, writing this algorithm was beyond the scope of this project. Instead, each position is calculated independently as three independent 1-dimensional variables. Then, the Easting and Northing velocities are combined during velocity calculations to get the horizontal flow (3.2.3 Flow Dynamics).

Due to the recorded positions being highly variable (4-7 seconds or more). A, a one-second epoch timeline is most appropriate. Grouping the data into 30-second intervals would result in some data being underestimated or overestimated. In 30-second bins, there could be instances where there are five recordings 6 seconds apart and then in the next group, there could be 12 recordings 3 seconds apart. The variability in the data could lead to skewed periods and times where the data is underutilised. Putting the data into one-second epochs ensures that all the available data is used evenly. During the periods with no data, the position is recorded as NAN (Not a Number) to allow array manipulation in Python. However, the data point has virtually no weighting when processed, meaning the results are not skewed from these missing values.

Sigma Observation	50m
Process Noise Position	5^{-20}m
Process Noise Velocity	5^{-20}m

The KF uses a set of predetermined processing variables (Table 3:2) to predict the position of the GPS nodes based on how accurate the data point is based on past predictions and the processing variables (

Table 3:2). These variables have been identified from trial and error, playing around with many different combinations to visually smooth the data to the required extent. This can be seen in Figure 3:4 where the different sigma observation values result in different levels of smoothing.

Process noise for position and velocity is set to 5^{-20} m to ensure each epoch is not heavily weighted. The filter requires a series of epochs with similar results to alter the KF course, smoothing the final results. Significant deviations from the predicted path require more epochs of data following this new trajectory for the KF to react, smoothing out the short-term variability. In the immediate short-term, GPS position changes might be lost, but this ensures the whole dataset is not undermined by GPS inaccuracies that occur from the

harsh environment while still revealing the longer consistent tidal changes that can be masked by extreme variability.

The sigma value of the observations (sigma observation) plays a crucial role in the KF as it determines the weighting of each observation relative to the filter's prediction. In more complicated KFs, individual epochs are assigned their weighting based on their perceived accuracy. However, for this filter, every epoch with a data point is assumed equally accurate due to the Pre-Processing (3.3.1.1 GPS Pre-Processing). When there is a recorded data point, the sigma observation is 50 m. When the epochs are a NAN, the sigma observation is 999999m. By adjusting the sigma observation, the KF interprets the data differently. A higher sigma observation leads to lower individual observation weights, which results in smoother data. Conversely, a lower sigma observation allows the filter to react more to variations in the observations, leading to a less smoothed output (Figure 3:4).

Sigma Observation	50m
Process Noise Position	5^{-20}m
Process Noise Velocity	5^{-20}m

Table 3:2, Kalman filter processing variables.

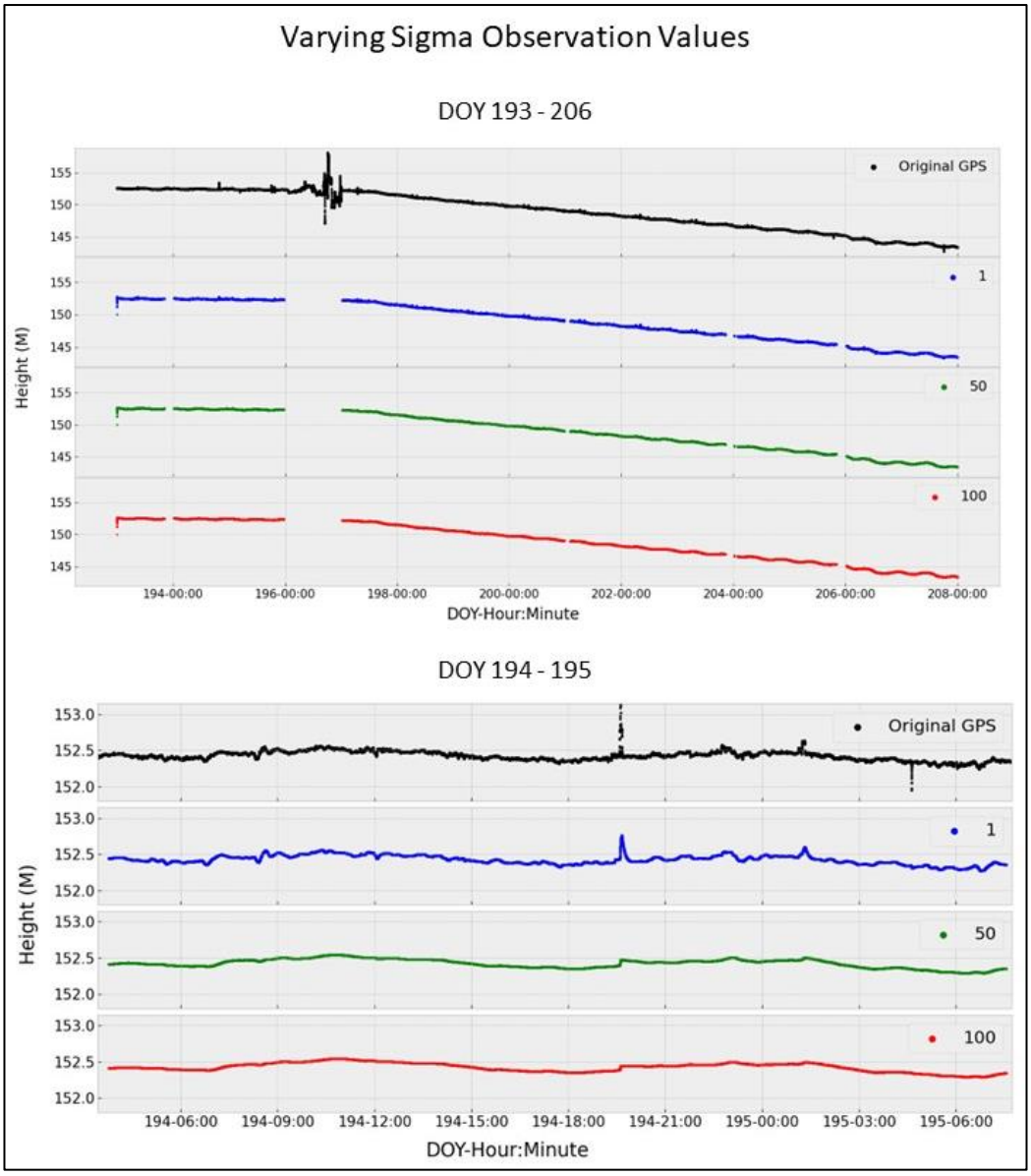

Figure 3:4, Varying sigma observations of Node 1 broken down from the whole data set (DOY 193-206) to DOY 194/195. In black is original data, then the varying levels of sigma observation in this instance looking at height. In blue at 1, following the original data closely. The chosen value in green (50) was picked due to its effective smoothing and reactions compared to red (100), which has a slightly more delayed response and is smoother.

The KF calculates a predicted position (predicted state vector) for each epoch. The predicted position is used with the accuracy of the prediction (predicted state VCM). The KF adjusts the coordinates based on the difference between the observed and predicted position. Over hundreds of epochs, the long-term changes will be picked up and seen in the computed position (corrected state vector). The algorithm is constantly updating and adjusting based on new data. In the beginning, it will take a while (~5 minutes for height) for the KF to smoothen (Figure 3:5). Once the KF has been running for some time with good data, the KF will account for variations and changes in the GPS data. For a more detailed step-by-step explanation of all equations used, see Chapter 7– Appendix for a list of all the

calculations used and the GitHub repository to see the final code (https://github.com/Jcolinese/Kalman_Filter).

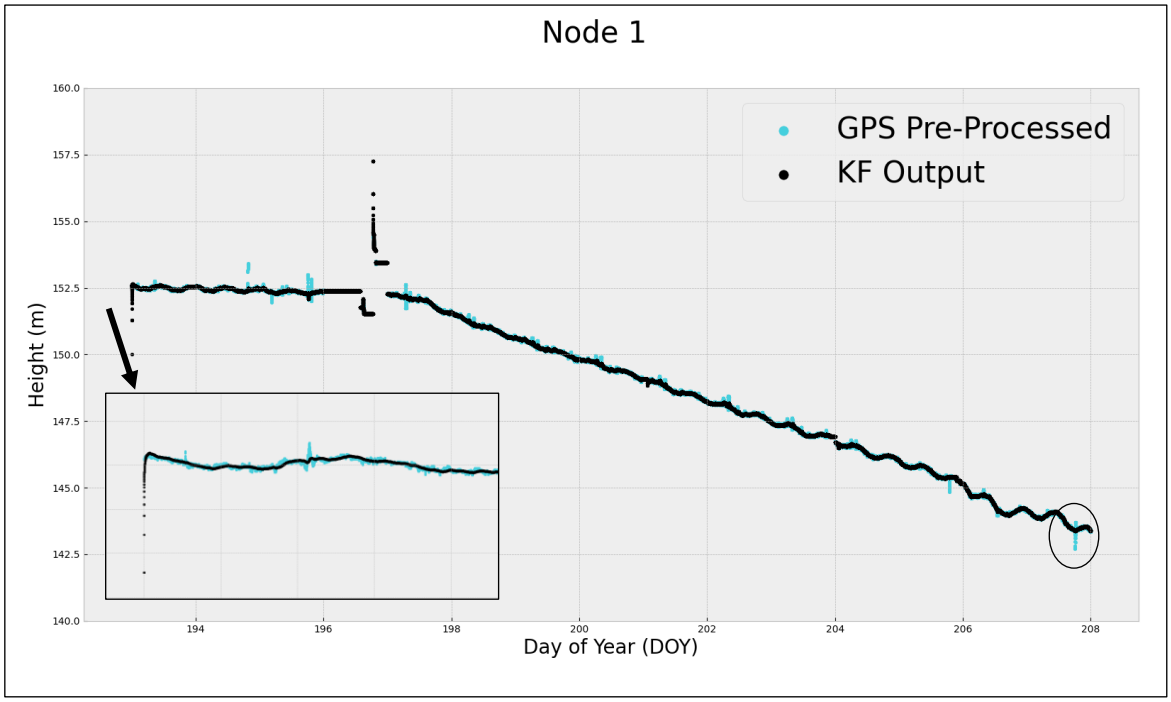

*Figure 3:5, GPS filtering from the Pre-processed data (*Table 2:1*) in light blue. Then, the KF output (black). The box shows a zoomed area of the first part of DOY 193, where the KF is Initiated and takes ~5 minutes of data to adjust. Circled is the same area as Figure 3:3 with the uncaught variability caught and smoothed.*

Another issue arises when there are significant data gaps (> 5 minutes) due to pre-processing or the nodes not transmitting successfully to the logging stations. When this occurs, the node's velocity for height is set to zero because of its highly variable and unstable nature, meaning the predicted state vector is unreliable. Regarding Easting and Northing, these positions are more predictable, so the filter continues to use the predicted state vector with predicted velocities. The Corrected State VCM is reset to its original value, allowing the KF to reset and start again thus ensuring the data is as accurate as possible. Once a "real" data point is identified, it can take time for the KF to re-settle. This is mitigated by removing any data within the 5-minute data gap and removing the next 5 minutes of "accurate" data, removing artificial variability in the GPS position and accounting for "bad" data that has not been captured in the original filtering (Figure 3:6) However, this is not perfect, and variability still gets through but is minimised.

The KF also provides an estimated velocity for height, easting, and northing. The easting velocity and northing velocity are combined to form horizontal flow (3.2.3.1 Horizontal Flow). Unlike their absolute positions after a data gap, there is extreme variation in speed as

it recalibrates and takes longer to level out. For horizontal flow, 20 minutes of data is removed after a 5-minute time gap. There can still be some variability, but this is the best middle ground for an across-the-board application for all nodes to ensure replicability. The beginning of the horizontal flow takes much longer to settle and is manually removed to a sensible point (Figure 3:7).

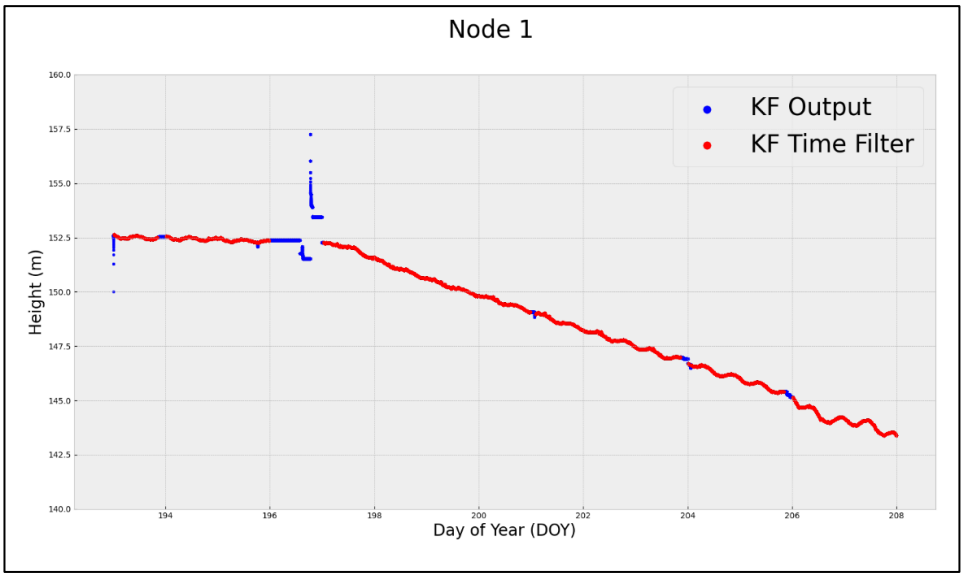

Figure 3:6, final results of Node 1 once large time gaps have been removed from the Kalman filter data (Red) compared to the Kalman filter output with the time gaps (blue).

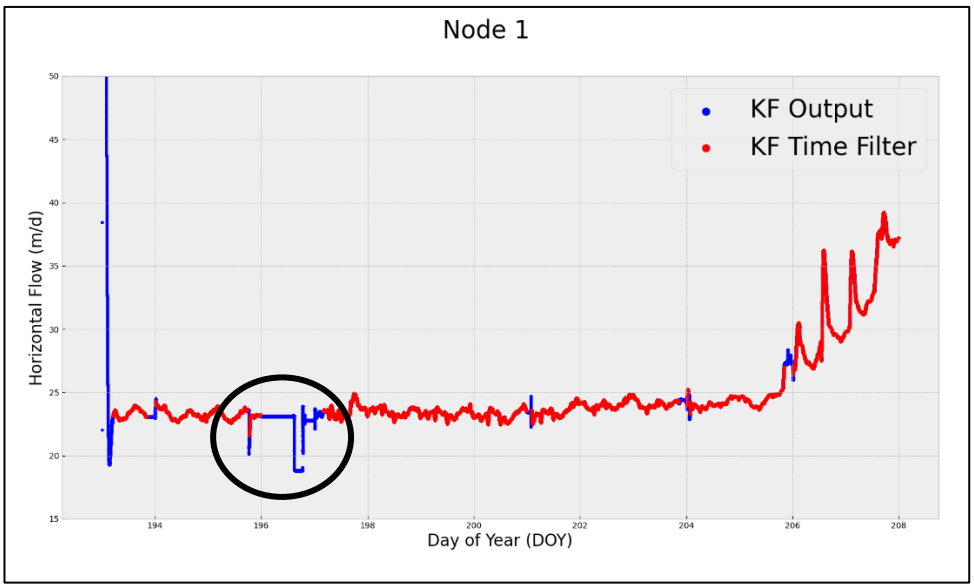

Figure 3:7, Horizontal flow of Node 1, at the beginning of the node's life, there is a significant change in velocity due to KF calibrating. As a result, it is removed. Secondly, circled is an example of time gaps leading to variations in Flow speed, which need to be accounted for and removed because this is from the KF recalibrating.

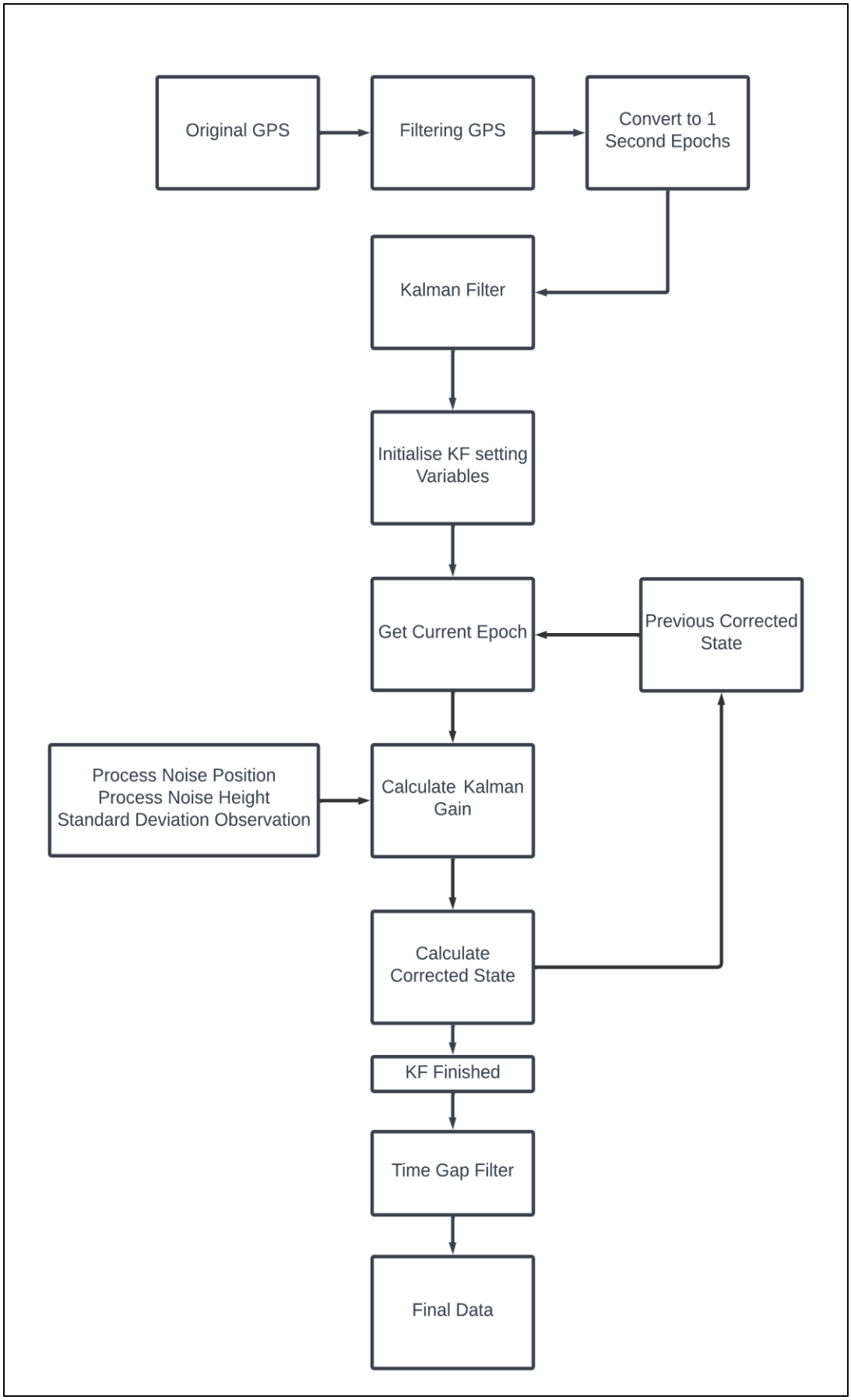

Figure 3:8, A Flow diagram of the GPS filtering process from original to final data.

3.3.2 Tidal Analysis

Harmonic analysis is essential to analyse the tidal constituents in the tide gauge and GPS data. Harmonic analysis is a complex and detailed branch of mathematics that is outside the scope of this Thesis. Fortunately, there are many programs designed specifically for tidal analysis and prediction. For example, T-Tide was developed by Rich Pawlowicz in MATLAB (Pawlowicz et al., 2002), building off T-Tide and subsequent upgrades from Leffler & Jay (2009), U-Tide was written to solve the problems in T-tide (Codiga, 2011). Firstly, U-Tide can handle irregularly distributed data with gaps. Secondly, U-Tide can also manage multiyear analysis. Originally, U-Tide was designed and written in MATLAB Code. However, Wesley Bowman has written a Python-based version (https://github.com/wesleybowman/U-Tide).

Using the Python version of U-Tide, identifying the tide gauge frequencies is simple, and quick and identifies statistically what tidal forcings are at play during short periods and the relatively longer-term trends occurring in the fjord, like the spring-neap cycle. Passing through the filtered GPS data allows the identification of the tidal variation in height and flow velocity (horizontal velocity). After running U-Tide, the program will return many values and components, for example, the tidal constituents (M2, S2), amplitudes of the constituents, signal-to-noise ratio (SNR) and percent energy (PE). The PE is a reconstructed fit of the input data superposing all the constituents, and by default, the elements are arranged by decreasing PE (Codiga, 2011). PE and amplitude can show the changing tidal influence, identifying periods with the strongest tidal signal. For example, over two weeks, the M2 signal will be highly variable due to the glacier conditions and the location of the GPS node. In theory, if the node is on a grounded portion of ice, we would expect little to no tidal influence in height compared to a GPS node on a portion of the glacier that is ungrounded and floating.

3.2.3 Flow Dynamics

Many variables on Helheim Glacier are of interest. The two main variables of interest are: firstly, changes in glacier height. Does the glacier rise and fall in the vertical plain (height) in time with the tides? Secondly, horizontal flow: Does the horizontal flow of Helheim Glacier speed up or slowdown in line with the ocean tides?

3.2.3.1 Horizontal Flow

The KF also outputs the predicted velocity for each flow direction (Easting, Northing and Height). The horizontal flow for each Epoch is easily calculated (Figure 3:9). The KF velocity is based on the same assumptions as the original ENU-filtered positions. As mentioned in 3.3.1.2 Kalman Filter, the horizontal flow requires time to recalibrate after a data gap, so 20 minutes of data after the data gap is removed.

$$Horizontal\ flow\ = \left(\sqrt{Easting_{velocity}{}^2 + Northing_{velocity}{}^2}\right) * 86400$$

Figure 3:9, the equation for calculating the horizontal flow (m/d), using Easting velocity and Northing velocity from the KF.

3.2.3.2 Flow Direction

In Qgis, the flow of the nodes can be plotted allowing visualisation of the flow direction and the general path of each node. However, visually identifying the flow direction in smaller time frames is hard. Flow direction is calculated as a bearing in radians (Figure 3:10) and then converted into an azimuth bearing using the flow chart (Figure 3:11).

$$Bearing = tan^{-1}\frac{\left(\frac{Northing_{velocity}}{Easting_{velocity}}\right) * 180}{\pi}$$

Figure 3:10, The equation used to calculate the bearing between two GPS points. The bearing is in radians.

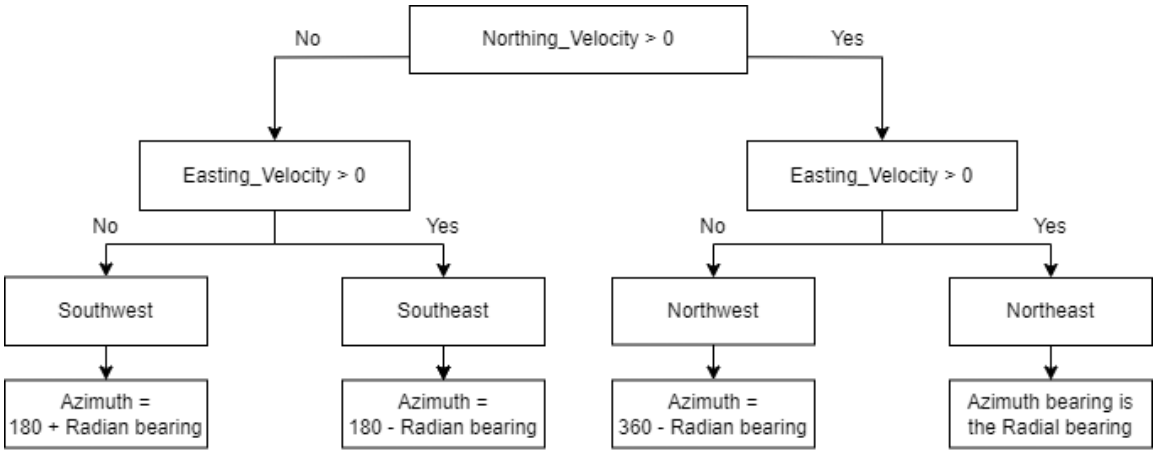

Figure 3:11, Flow chart of how to calculate the flow direction and the conversion of the bearing in radians to azimuth.

3.3.4 Tidal Signal Through Time – Moving Power Graphs

Due to the size and variable characteristics of Helheim Glacier, the tidal signal in the GPS data will change over time as the GPS reaches and then crosses the grounding line. Using a moving power graph allows the identification of periods with strong or weak tidal signals. The KF data is resampled into 1-minute intervals based on the median to speed up the code when running through U-Tide. Then, the first four days of data pass through U-Tide. Identifying the tidal constituents within the four days and their characteristics (i.e., amplitude and percent energy). Then, the time frame of data is moved by an hour and run through U-Tide again, generating another dataset of the constituents for that period, and repeated for the whole dataset for all nodes in both height and horizontal flow. The data is resampled into 1-minute intervals due to data processing constraints. To pass all data through U-Tide would mean passing 345,600 individual data points for every calculation, compared to only 5,760 data points when the values are resampled to 1-minute intervals.

Chapter 4 – Results

4.1 General GPS Results

Of the 20 nodes placed on Helheim Glacier in the summer of 2013, 19 produced usable data despite the adverse conditions experienced on the glacier. Most nodes stopped working for periods, and not all the data collected is of good quality, with some nodes performing better than others.

For all 19 nodes, 337 days of workable data were recorded. The node with the most available data as a portion of its time on the glacier is node 9, which lasted 28.6 days, with 91% of the time with useful data. The node that lasted the longest is node 3, which lasted 44.7 days until its recovery. This node also has available data for 88% of the time spent on glacier. The time between each GPS position varies considerably from node to node and through time, with most nodes recording data every 4-7 seconds (Chapter 7 – Appendix).

The worst performing node is node 18, with only 34% of the time on glacier producing usable data from being on glacier for 35.7 days. After DOY 212 (31st July 2013), the node essentially had no functional data for ~21 days until DOY 233, where data picked up again (Table 4:1). However, this last portion of data is insufficient for any meaningful complete analysis. The shortest-lived node (after node 16, which never turned on) is node 19, lasting only 7.3 days with only 5.7 days of usable data.

Table 4:1, Time the Nodes spent on Helheim Glacier. Highlighted in green are the nodes with available data for >80% of the time on glacier, with the red highlighting showing where <60% of the time there is data, with the final column showing the distance travelled of each node.

Node	Start	End	Days			Distance Travelled (km)
			On Ice	Available data	% Available	
1	11-Jul	26-Jul	15.0	12.0	**80%**	0.32
2	13-Jul	25-Jul	11.8	6.3	**54%**	0.21
3	14-Jul	02-Sep	50.6	44.7	**88%**	1.13
4	12-Jul	01-Aug	19.9	10.1	**51%**	0.43
5	12-Jul	25-Aug	45.0	36.9	**82%**	0.92
6	12-Jul	25-Jul	12.5	9.4	75%	0.26
7	11-Jul	04-Aug	23.5	19.7	**84%**	0.45
8	13-Jul	28-Aug	45.4	40.2	**89%**	0.86
9	11-Jul	09-Aug	28.6	26.0	**91%**	0.63
10	12-Jul	21-Jul	9.0	7.3	**82%**	0.13
11	12-Jul	25-Jul	12.4	10.2	**82%**	0.28
12	12-Jul	25-Jul	12.3	10.3	**84%**	0.24
13	15-Jul	28-Aug	44.0	29.9	68%	1.03
14	15-Jul	07-Aug	23.0	15.4	67%	0.50
15	12-Jul	25-Jul	12.9	10.6	**82%**	0.27
16	NAN	NAN	NAN	NAN	NAN	NAN
17	16-Jul	26-Jul	11.0	6.9	63%	0.20
18	16-Jul	21-Aug	35.7	12.2	**34%**	0.74
19	12-Jul	19-Jul	7.3	5.7	79%	0.10
20	12-Jul	08-Aug	26.5	22.9	**86%**	0.56

4.1.2 Distance Travelled

Each node travelled different distances during the experiment (Figure 4:1). On average, the nodes travelled ~0.5km before being lost/collected. However, node 3 travelled ~1.13 km over its 50-day lifespan, whereas nodes 10 and 19 travelled 0.13 km and 0.1km respectively. Five nodes travelled over 0.7km (Table 4:1).

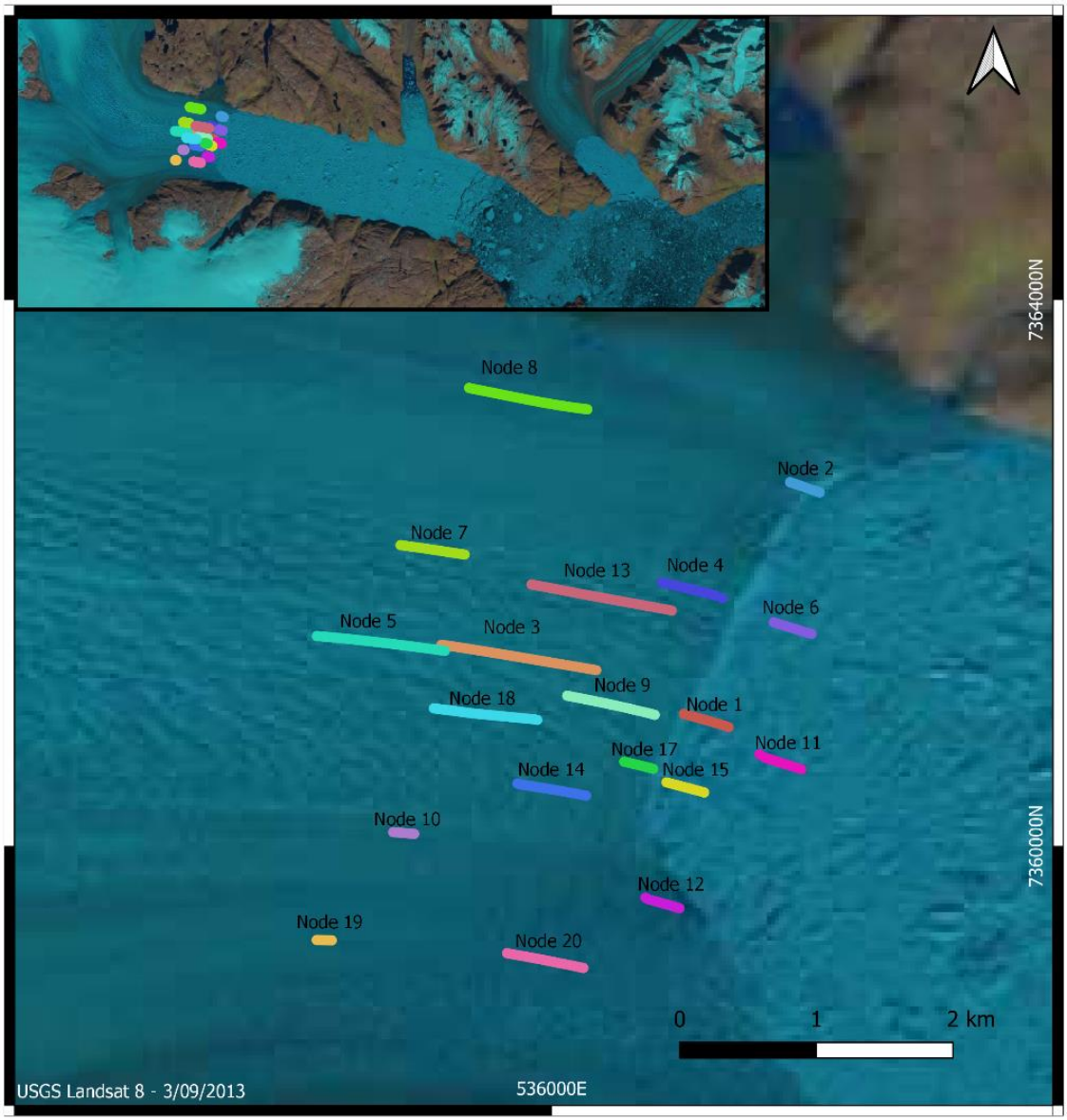

Figure 4:1, All node paths travelled are reprojected onto QGIS using the EPSG 32424 (WGS 72BE/UTM zone 24N) coordinate reference system. Top left, showing the overview of Helheim Glacier and the Fjord.

Flow Direction, occurred as South-Easterly (7.2 Results) flowing down the glacier, with the only identifiable changes being a shift north resulting in the only other identified flow direction being northeast. However, this only occurred in 9 out of the 19 nodes, with eight travelling Northeast less than 0.3% of the time. Node 19 is anomalous with the other nodes because 5.61% of the time, node 19 appears to be travelling Northeast.

4.2 Observations

4.2.1 Tide Gauge

The tide gauge, as expected when run through U-Tide, shows classic tidal signals (Table 4:2A). The data is passed through U-Tide for the whole 3-year period, of which it picked up all the tidal constituents mentioned in Chapter 3, including M2, with an amplitude of 1.04 dbar. Due to the lower sampling period in Table 4:2B, the tidal constituents have larger amplitudes and percent energy than the longer time scales because other long-period forcings are present over the longer time scales. For the complete list of tidal constituents, see Chapter 7 – Appendix section 7.2 Results.

The observed tide gauge agrees reasonably well with the U-Tide predictions with a variation of 0.1 dbar. More considerable variations are in the residual; for example, around the 24th - 26th of July (DOY 205 to 207), many recorded calving events occur, and these correlate to the disagreement between the observed and the predicted tides (Figure 4:2 & Figure 4:3). Not every recorded calving event has an impact on the tide gauge data. For example, around 26th July (DOY 207) at 11 am, an observed calving event was interpreted from the camera images but did not appear on the tide gauge. For example, on 24th July (DOY 205) at ~8 pm, two calving events are recorded by both the cameras and the seismic data. They are causing significant variations between the observed and predicted tide of 0.1 dbar, equivalent to a 10 cm difference in fjord surface elevation.

Table 4:2, The tidal constituents alongside their frequency in cycles per day (CPD), amplitude, phase and percent energy of the tide gauge identified when passed through U-Tide. The table shows the data for the entire recorded period of 734 days(A) and just from the summer of 2013 (53 days) until it was recovered (B). The location of the tide gauge is shown in Figure 3:2.

A	2011-08-20 to 2013-08-23			
Constituent	Frequency CPD	Amplitude	Phase ◦	Percent Energy
M2	1.93	1.04	200.42	79.80
S2	2.00	0.42	238.86	12.68
N2	1.90	0.20	178.22	2.93
K1	0.93	0.15	148.98	1.74
O1	1.00	0.07	113.71	0.39
P1	1.00	0.05	143.74	0.17

B	2013-07-01 to 2013-08-23			
Constituent	Frequency CPD	Amplitude	Phase ◦	Percent Energy
M2	1.93	1.05	200.37	81.17
S2	2.00	0.40	250.03	11.92
N2	1.90	0.23	171.42	3.81
K1	0.93	0.18	163.05	2.31
O1	1.00	0.07	114.20	0.38
P1	1.00	N/A	N/A	N/A

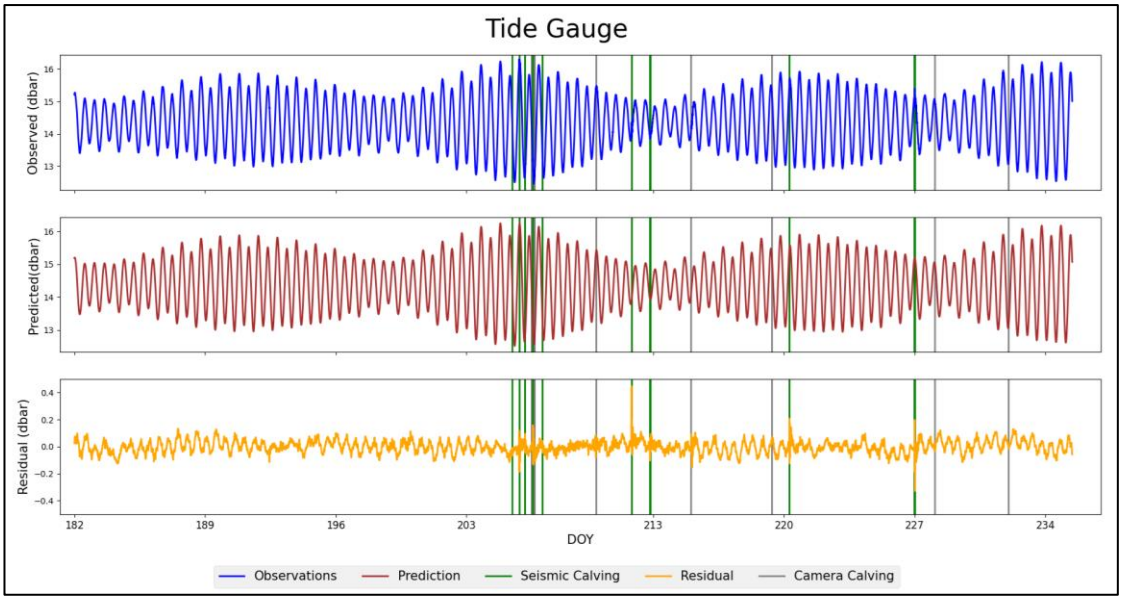

Figure 4:2, Tide gauge results: Blue is the observed and recorded tidal modulation in Sermilik Fjord, Brown is the predicted tides from U-Tide, and yellow is the residual of the observed and predicted tides. Behind the data are also calving events, in green calving events recorded from the seismic record and grey from the cameras.

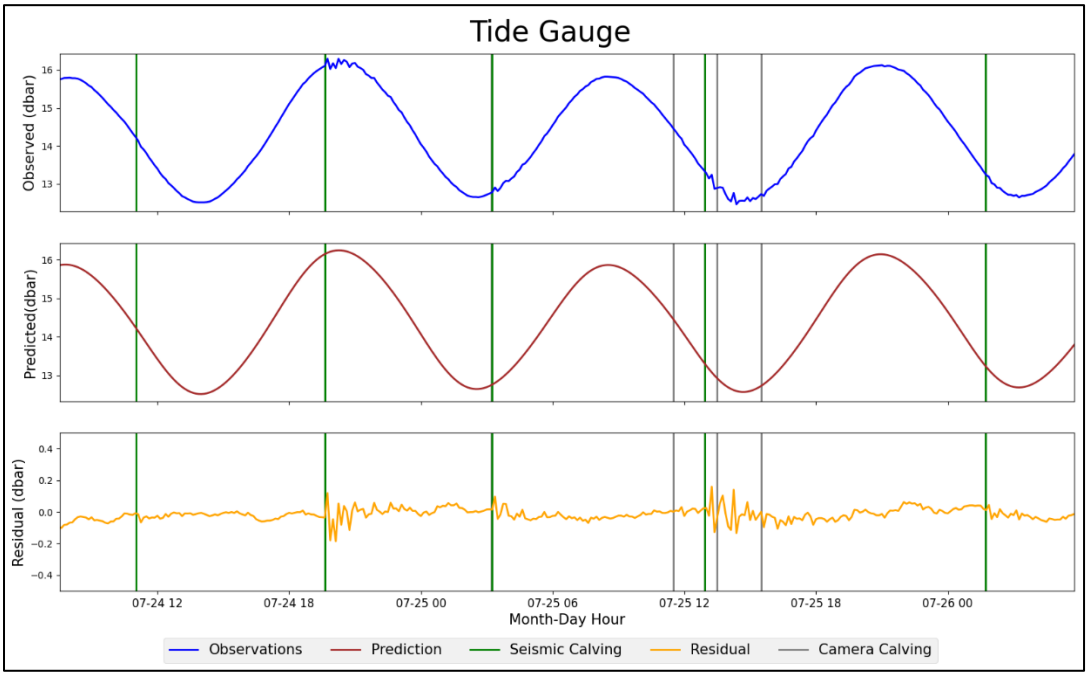

Figure 4:3, Tide gauge result from 24th July to 26th July (DOY 205 to 207), shows the disagreement periods between the observed and predicted tide. Behind the data are also calving events, in green calving events recorded from the seismic record and grey from the cameras. There are higher variations and disagreements between the predicted and observed tide, occurring during calving events.

4.2.2 Weather

Weather data provided by Michael Shahin (University of Kansas) from a weather station located next to Helheim Glacier (Chapter 3 – Methodology) for the period between 10th July and 3rd September (DOY 191-246) shows that the mean air temperature was 7.45˚C with a median temperature of 7.10˚C (

Table 4:3, Figure 4:4). The maximum temperature recorded was 16.3˚C on 25th July at 19:45 (DOY 206), while the lowest temperature was -1.4˚C on 29th August at 06:30 (DOY 241).

Precipitation data (Figure 4:4) from the Danish Meteorological Institute recorded at Tasiilaq, recorded six periods where precipitation was >2mm/12hr. There are also two distinct periods around DOY 220 and 241 where precipitation reaches ~7mm/12hr.

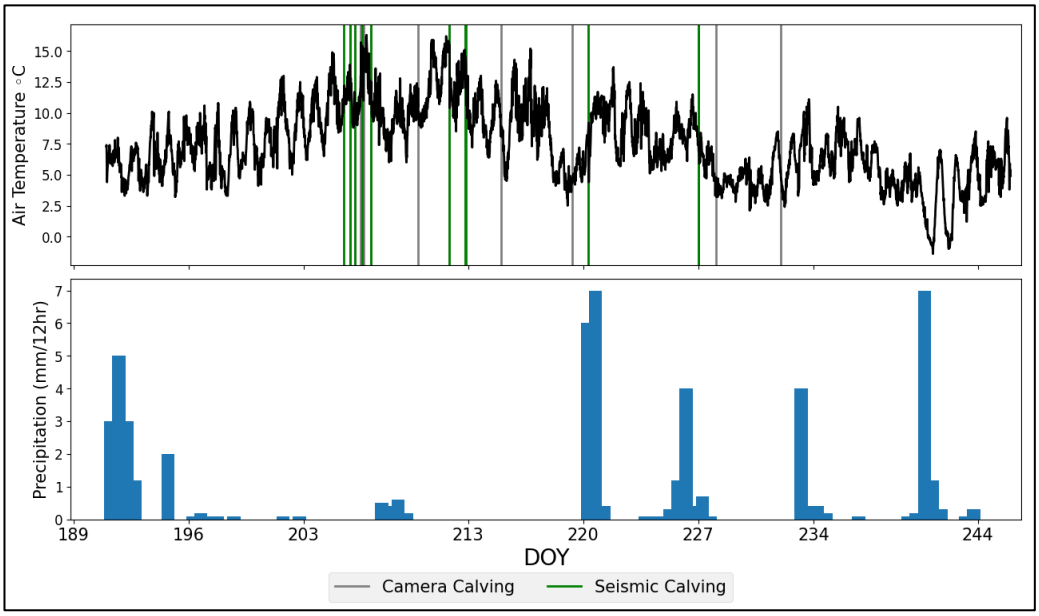

Figure 4:4, Air temperature from Michael Shahin (University of Kansas) in ˚C, and precipitation from the DMI recorded as mm/12 hours. Behind the air temperature data are the caving events picked by the cameras and the Seismic data.

Table 4:3, Basic statistics of the air temperature data from Michael Shahin (University of Kansas) in ˚C.

Air Temperature ◦C 10/07/2013 to 03/09/2013	
Mean	7.45
Minimum	-1.4
25%	5.2
Median (50%)	7.1
75%	9.6
Maximum	16.3
Standard Deviation	3.02

4.3 Long-term Flow and Tidal Modulation

4.3.1 Long-term Changes in Speed

The flow speed of Helheim Glacier varies with location (Figure 4:5). For example, node 11 has the fastest median flow speed at 24.35 m/d, and node 19 is the slowest with a median flow speed of 16.44 m/d (Figure 4:5).

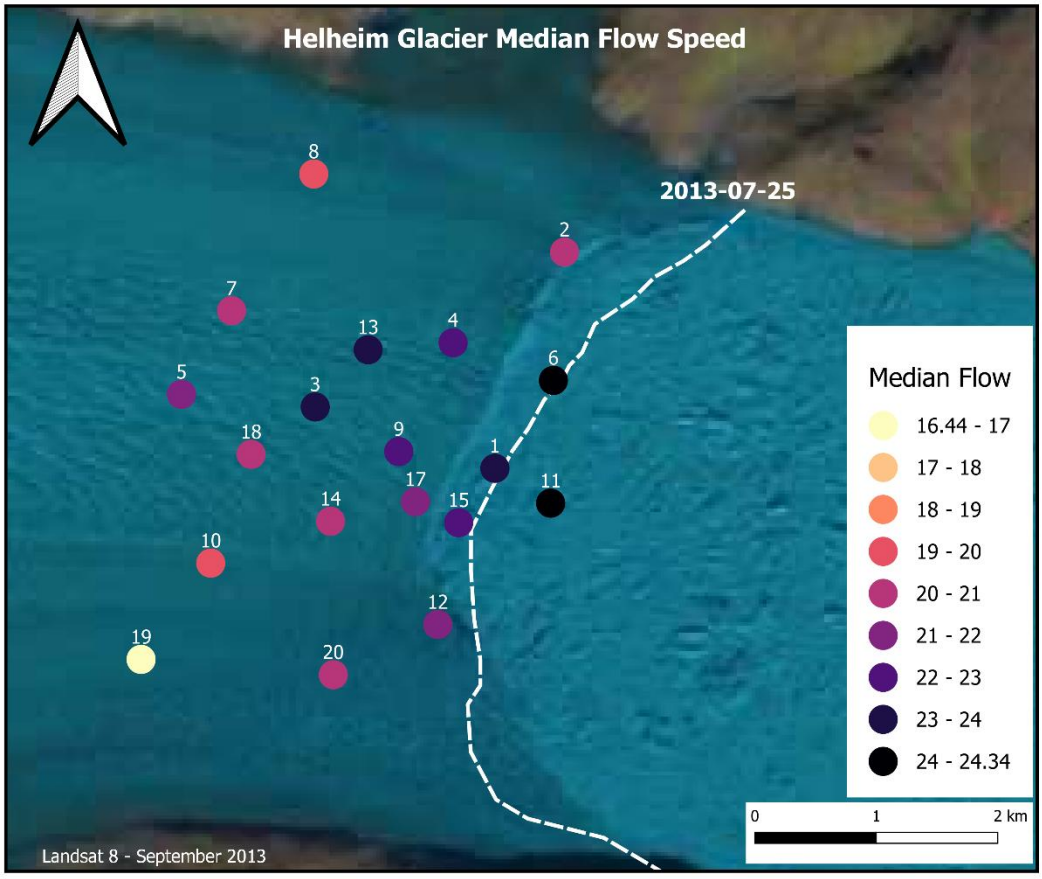

Figure 4:5, Average flow speed (m/d) for each node for the life of the nodes, Nodes 11 and 1 being some of the fastest in the middle of Helheim Glacier very close to the calving front, then node 19 located in a slower area with a comparatively much slower speed.

Tidal signals through time have been identified using the 4-day moving power graphs (Chapter 3 – Methodology). All nodes show tidal modulation of their flow speed throughout the experiment. The largest amplitude is M2 during periods without calving events. Most nodes during periods without calving events have tidal amplitudes ranging between 0.2-0.4 m/d. The most significant amplitudes reached peaks of 0.7-0.8 m/d. Other times, M2 amplitudes have peaked at >1 m/d. These are directly linked to the calving events and

might not result from long-term flow changes. I now discuss examples of the tidal modulation of the flow speed of different nodes.

Node 3 (Figure 4:6

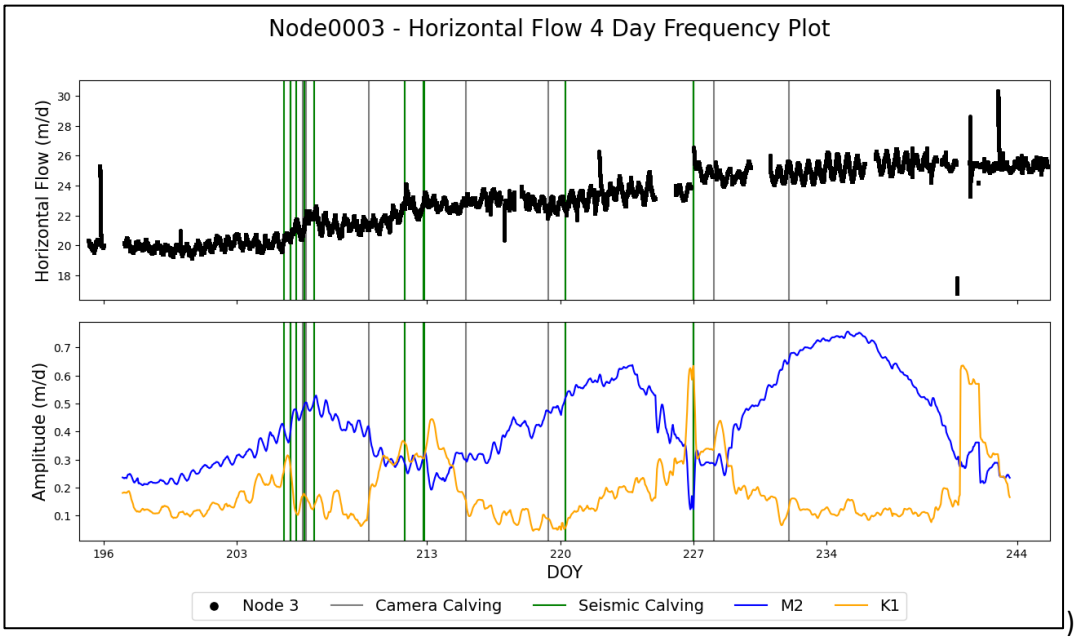

) has a visual semidiurnal modulation through time with horizontal flow starting at 20 m/d. After the calving events around 25th July, (DOY 206) average flow increases to ~21.5m/d; then steadily increases to 26m/d around 22nd August. Node 3 goes through three phases of tidal modulation broken up by calving events disrupting the long-term flow. Firstly, M2 amplitude increases from ~0.2m/d, peaking at 0.5m/d. This amplitude then falls as K1 becomes the key modulation, alongside calving events causing large spikes in flow. The second phase is characterised by M2 returning at 0.4m/d, increasing to 0.6m/d. Then, after the next series of calving events, M2 is at 0.4m/d and increases to 0.7m/d. Then, the data becomes patchier as the node gets closer to the calving front.

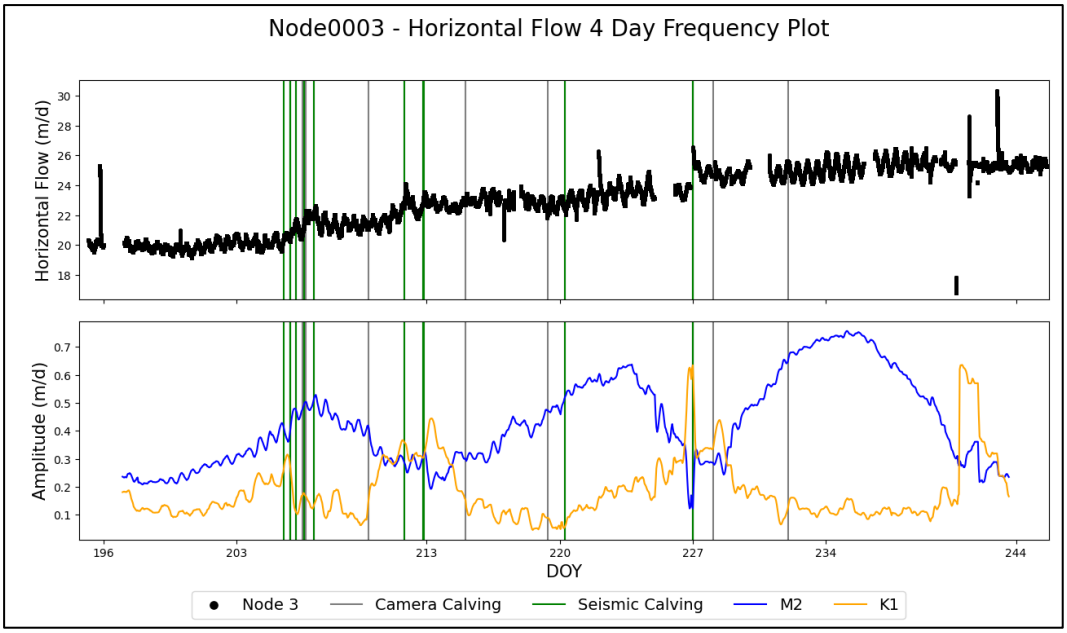

Figure 4:6, Moving power graph for Node 3, showing horizontal flow and the resulting amplitude of the tidal modulation of M2 (blue) and K1 (orange) amplitudes (m/d) from the 4-day moving power graph using U-Tide.

Node 4 does not change flow speed during its lifespan and only lasts ten days; however, it is an excellent example of horizontal flow and the semidiurnal signal that goes alongside it. In Figure 4:7, the moving power graphs show a clear M2 Amplitude of ~0.4 m/d and a percent energy hovering around 90-75%. At times, 90% of the tidal signal U-Tide identifies is from the M2 tide. Passing the whole of node 4 through U-Tide results in an M2 amplitude of 0.42 m/d and a K1 of 0.16 m/d.

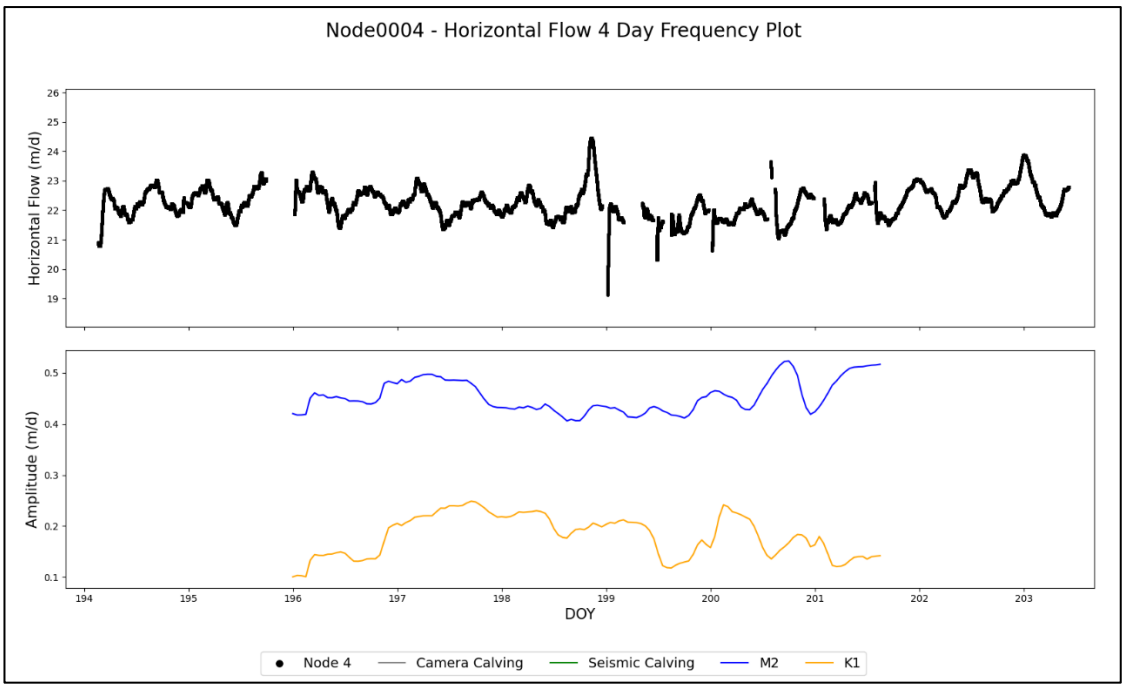

Figure 4:7, Moving power graph for Node 4, showing horizontal flow and the resulting M2 (blue) and K1 (orange) amplitudes (m/d) from the 4-day moving power graph in U-Tide.

Node 8 (Figure 4:8), one of the longest-lasting nodes, has provided ample data over ~1.5 months. It begins by decreasing the flow speed from 17 to 16.5 m/d. Flow then increases back to the starting speed, while a series of calving events around 25th/26th July (DOY 206/207). Horizontal flow speed continues to increase, reaching 19m/d on 31st July (DOY 212), then another calving event occurs at the same time the increase in flow speed levels off. Horizontal flow gradually increases, reaching ~20 m/d until another calving event causes a stepwise increase in speed, causing the speed to jump by 1 m/d. Alongside this, the visual tidal modulation gets larger. Node 8 also goes through the same three phases as node 3 (Figure 4:9), with M2 amplitude increasing from 0.2 to 0.4 m/d, then falling again, growing after calving event 0.25-0.4 m/d and falling back drastically and finally, rising to a peak M2 amplitude of ~0.7 m/d.

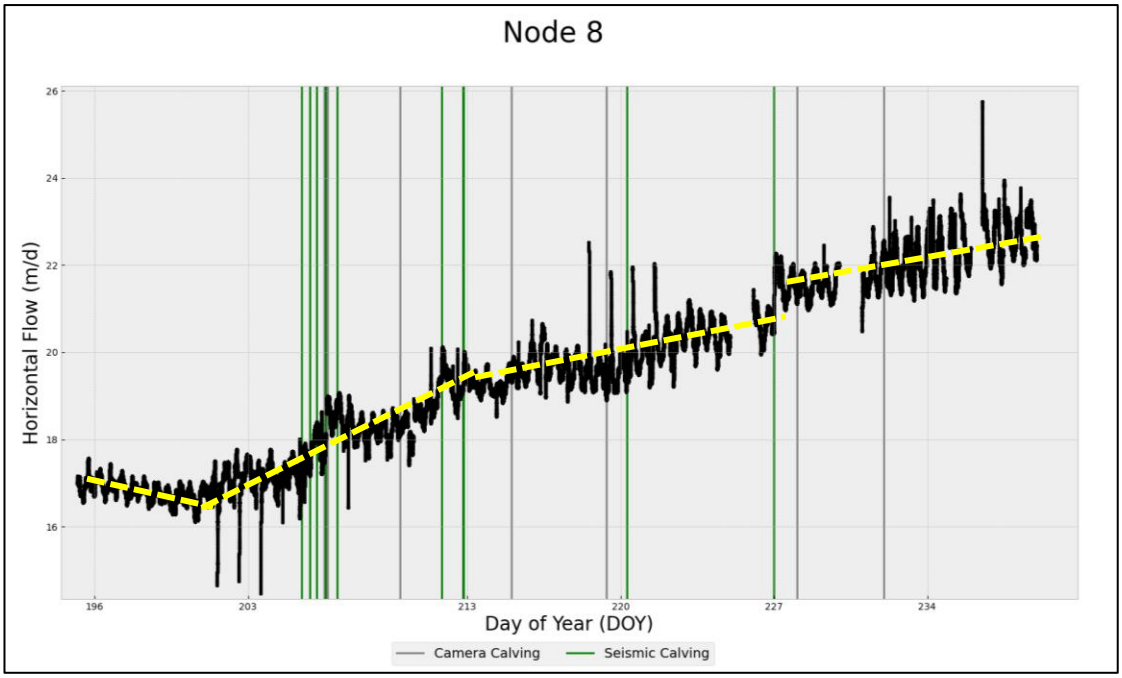

Figure 4:8, Node 8 horizontal flow and the different phases of speed are shown by the dashed yellow lines.

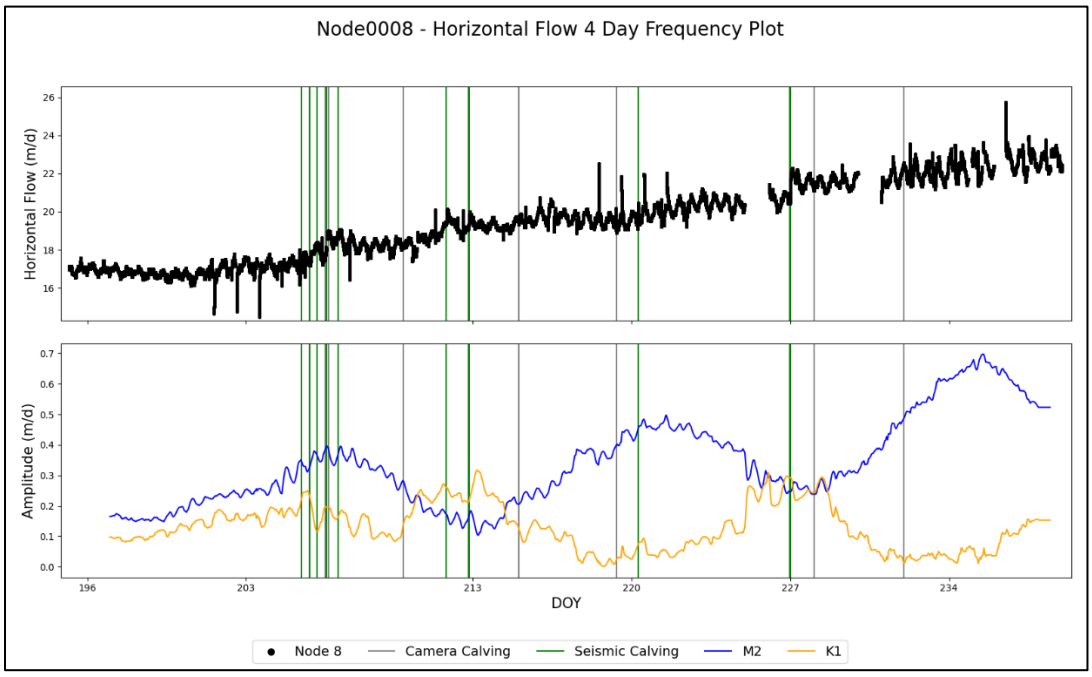

Figure 4:9, Moving power graph for Node 8, showing horizontal flow and the resulting M2 (blue) and K1 (orange) amplitudes (m/d) from the 4-day moving power graph in U-Tide.

Node 9 is another node that increases its flow speed as it gets closer to the calving front (Figure 4:10). The node begins flowing ~21 m/d with an M2 tidal amplitude of 0.5 and a K1 tide around 0.1 m/d. During calving events around DOY 206, the flow speed increases to 22.5 m/d, with the M2 increasing to 0.8 m/d in amplitude and K1 modulation seemingly disappearing. After these events, the M2 amplitude falls back to 0.5 m/d. However, this

coincides with calving events occurring from 210 to 215. Three large spikes in flow occur, as explained below in Chapter 4.4 Glacier Flow and Calving Events. These large spikes in flow occurring nearly daily cause U-Tide to interpret K1 as having a dominant effect with an amplitude of 1.5m/d. After these calving events, there is much noise in the system, and any tidal modulation is lost, as shown in the dramatic fall in K1. Horizontal flow holds steady at 27 m/d with some variation. Then, shortly after, node 9 is lost.

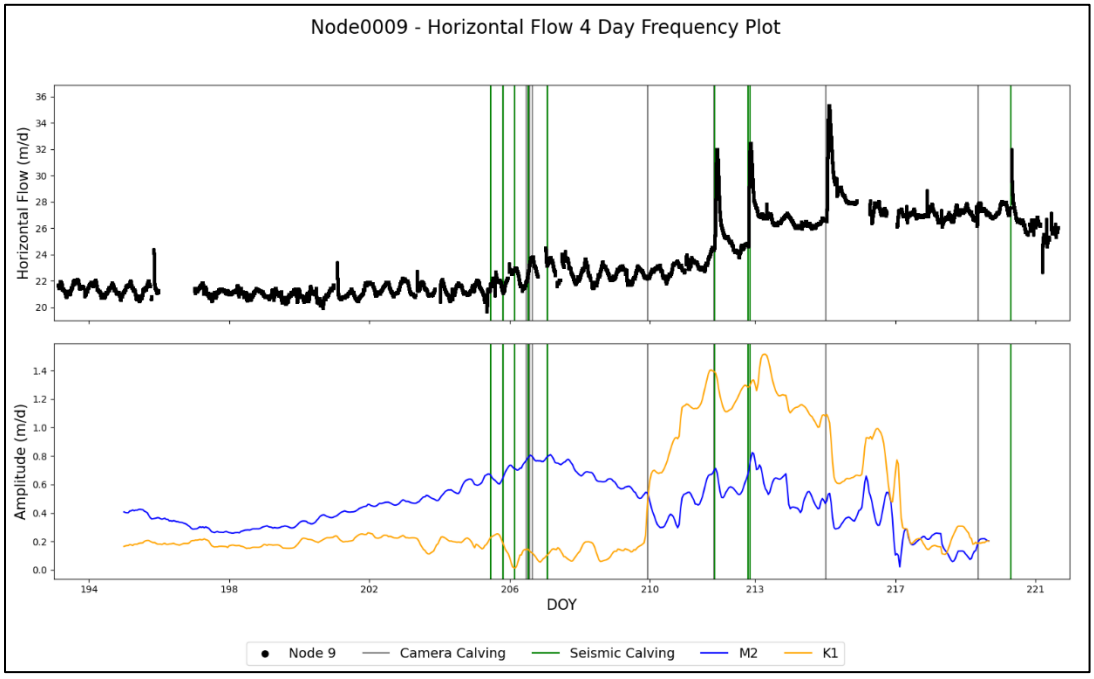

Figure 4:10, Moving Power graph for Node 9, showing horizontal flow and the resulting M2 (blue) and K1 (orange) amplitudes (m/d) from the 4-day moving power graph in U-Tide.

Node 20 presents some curious flow modulation despite the patchy nature of the data. The node begins flowing at ~19 m/d (Figure 4:11). After calving events around DOY 206, flow increases to ~21 m/d. At the same time, the M2 tidal amplitude increases from 0.2 to 0.4 m/d just before the calving events. Around DOY 206, at the same time, K1 is picked up with an amplitude of 0.2 m/d. Flow sharply increased after the calving event on 31st July (DOY 212). Flow speed holds steady at 25.8 m/d alongside the semi-diurnal variations. M2 peaks with the calving events at 0.4-0.6 m/d and then settles to a modulation of 0.4 m/d. Calving events in time with sharp changes in horizontal flow and data gaps can lead to periods where M2 data is erroneous (DOY 210-214). Interestingly, following the calving event on 3rd August (DOY 214), flow begins to slow, decreasing by ~1 m/d until the node is lost. Alongside this slowdown, M2 recovers back to 0.4 m/d and steadily increases to a peak amplitude of 0.7 m/d, and at the same time, K1 falls to 0.1 m/d or less.

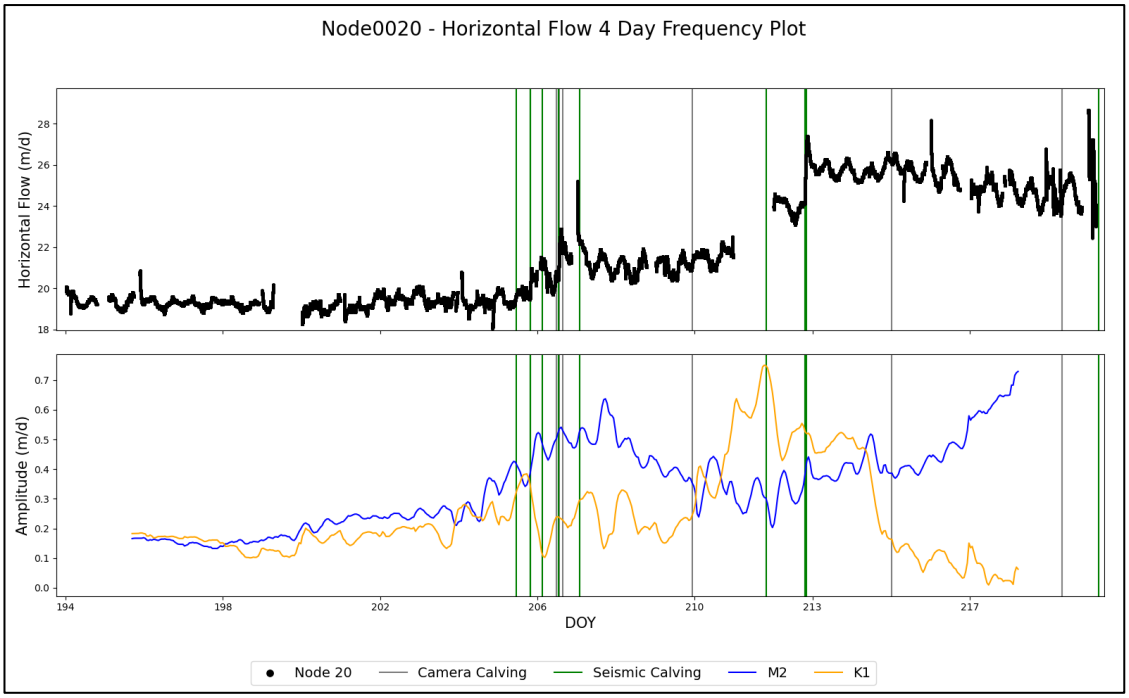

Figure 4:11, Moving power graph for Node 20, showing horizontal flow and the resulting M2 (blue) and K1 (orange) amplitudes (m/d) from the 4-day moving power graph in U-Tide.

Nodes 1 and 11 both only last until DOY 204/206, being the closest to the calving front at the beginning of the study; both show a modulation with M2 tidal signal with an amplitude of 0.4m/d (Figure 4:12 and Figure 4:13) for the whole life of the node up until the calving events that caused substantial increases in flow disrupting the tidal cycle. Both nodes follow the same trajectory, with node 11 being faster, with a median flow of 24.3 m/d and node 1 at 23.73 m/d (Figure 4:14). Before node 11 is lost, the M2 amplitude also increases to 0.5 m/d. Then, during the calving event that leads to its demise, M2 amplitude reaches 0.7; however, this is spurious, and the calving events have likely led to these extreme changes.

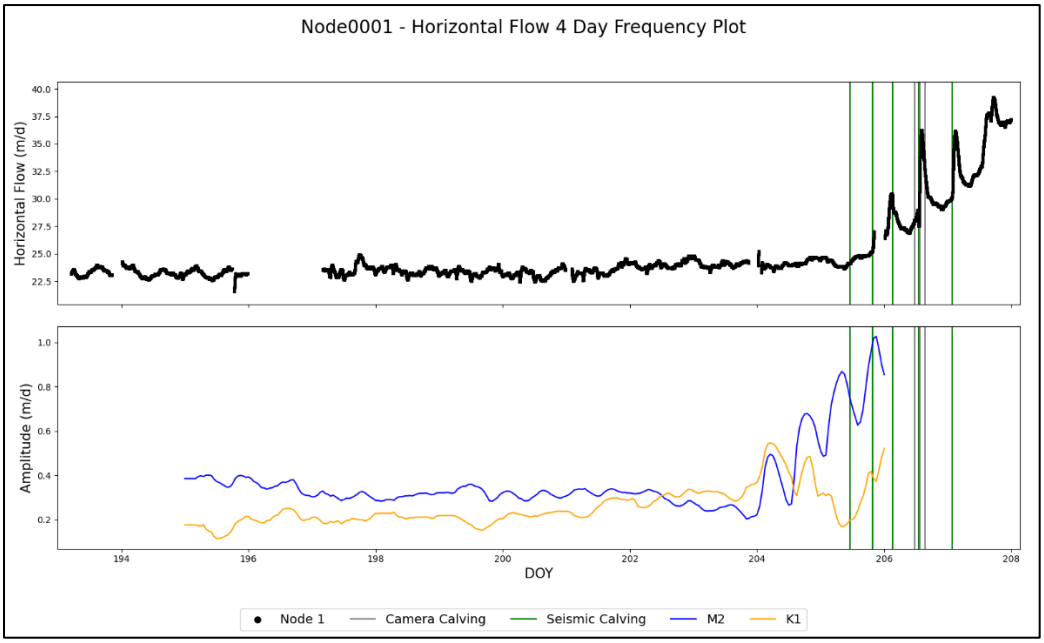

Figure 4:12, Moving power graph for node 1, showing horizontal flow and the resulting M2 (blue) and K1 (orange) amplitudes (m/d) from the 4-day moving power graph in U-Tide.

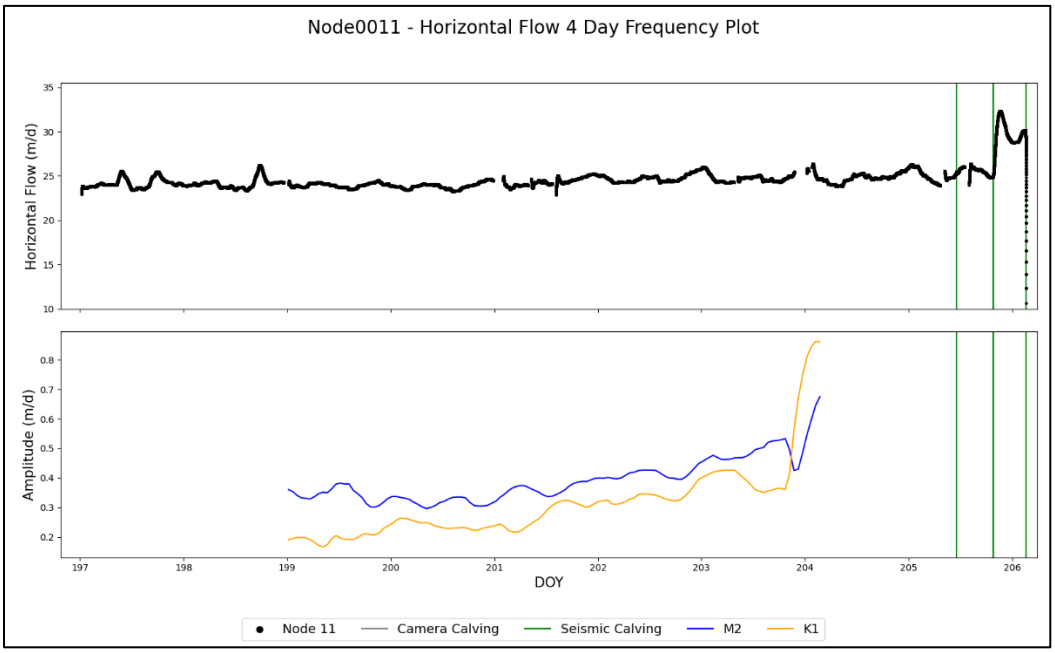

Figure 4:13, Moving power graph for node 11, showing horizontal flow and the resulting M2 (blue) and K1 (orange) amplitudes (m/d) from the 4-day moving power graph in U-Tide.

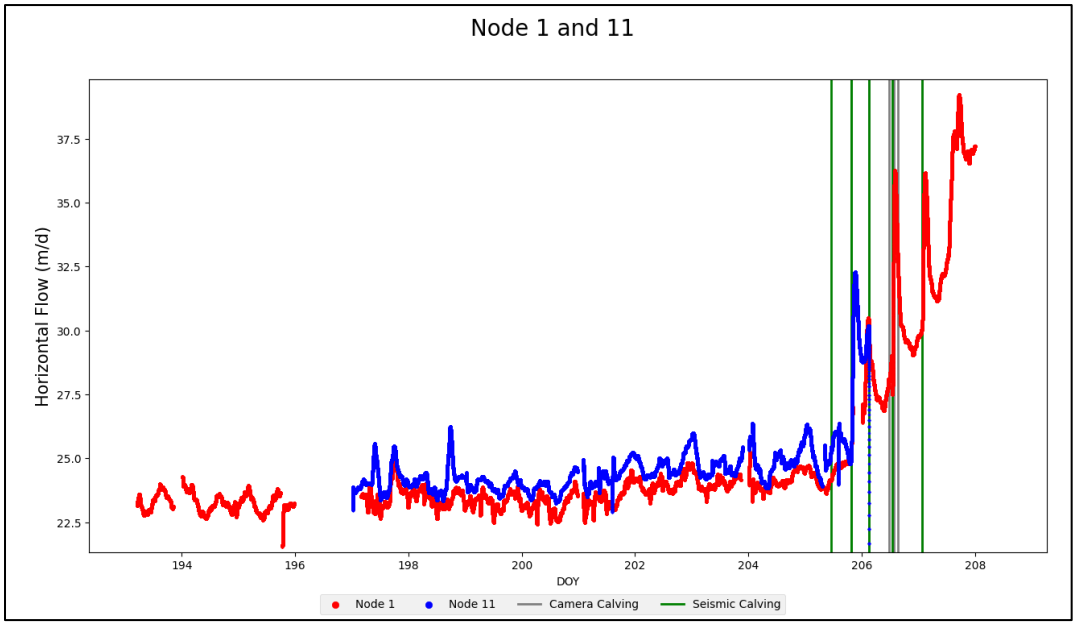

Figure 4:14, Horizontal flow of nodes 11 (blue) and 1 (red), showing how they react similarly, apart from node 11 being faster and reacting differently to the first calving event as it is lost.

4.3.2 Long-term Changes in Height

4.3.1.1 General

Overall, most nodes decrease in elevation over time, starting at various heights, consistent with the downslope flow of the glacier. The highest node (19) started at 228.3 m (above ellipsoid WSG84) and flows downslope at 0.36 m/d vertically. The lowest nodes initially are 11 and 17, starting at 138 m. However, they showed different regimes with node 17 constantly flowing downslope at 0.65 m/d, whereas node 11 increases in height. Tidal forcing from the tide gauge shows an M2 amplitude of 1 d-bar equivalent to ~1 m.

Visually, eight nodes show a semi-diurnal height modulation with varying amplitudes and over different time frames. Tidal modulation in height is minimal when it occurs and split into three categories, where U-Tide picks up no discernible modulation with amplitudes <1 cm. Then small, with M2 modulation between 2 and 5 cm, the largest amplitudes >5 cm, many nodes show small amplitudes, with nodes 7, 10, 12, 19, and 20 showing <1 cm M2 tidal amplitude. When there is a discernible M2 modulation, most nodes vary within the 2-5cm range. An amplitude of 2-5 cm is difficult to identify visually. These amplitudes are not constant and vary, e.g., at calving events. Nodes 2, 3, 4, 5, 8, 14, 15, 17 and 18 all fall into this category, showing not much information; however, U-Tide at specific periods was able to differentiate an M2 signal.

Node 11 is an excellent visual example of semi-diurnal modulation (Figure 4:15). Data gaps plague the beginning of the node (DOY 194-197) and vary due to GPS inaccuracies and pre-processing, removing insufficient data. Post DOY 197, there is a tidal semi-diurnal modulation of height slowly increasing as it travels down the glacier with an M2 amplitude starting at 0.08 m, which on DOY 203 reaches an amplitude of 0.17 m. Then, by DOY 206, a calving event causes a 3 m increase in height, and M2 amplitude increases further in line with the calving event, maxing out at 0.25 m. Then, the node is lost during this calving event, showing the potential uplifting of the new glacier front. From DOY 193 to 205, the height increased at a rate of 0.31m/d.

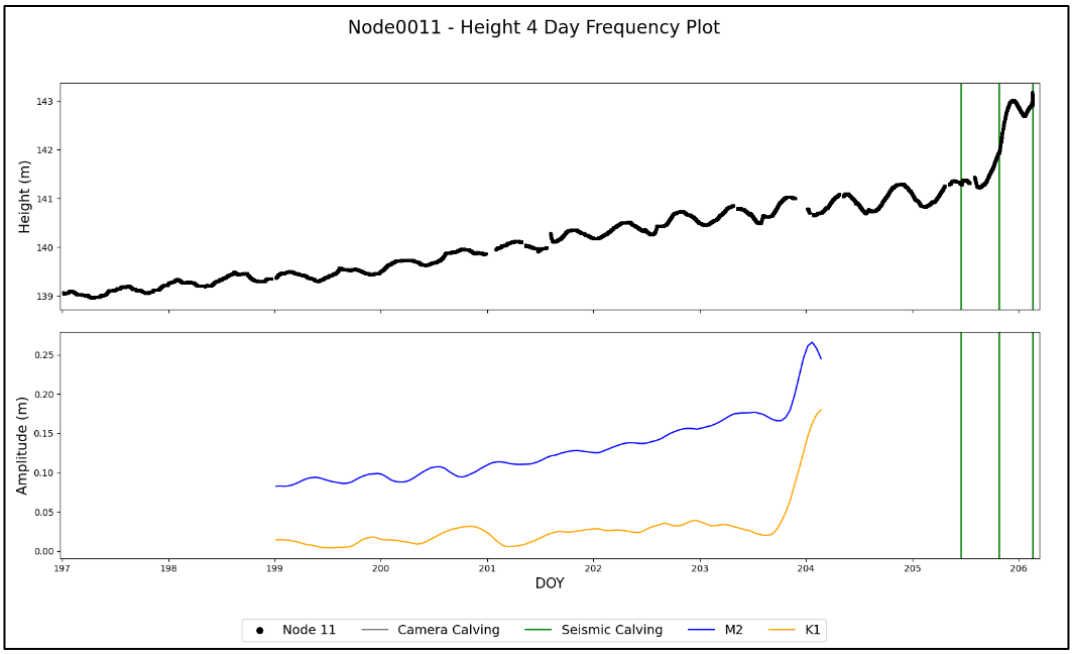

Figure 4:15, Moving power graph for node 11, showing the height data (black) and the resulting M2 (blue) and K1 (orange) amplitudes (m) from the 4-day moving power graph in U-Tide.

Nodes 1, 15, and 6 have a similar pattern of changes in height (Figure 4:16). All three-show no change in height at the beginning, then around DOY 196/198, begin a progressive fall in GPS height until they are lost. Node 15, being at the lowest elevation of the three at ~151 m, falls to ~141 m, then node 1 is only slightly higher, starting at ~152 m and falling to ~143 m. During the next 9-10 days, all three nodes drop between 0.8 to 1 m/d. Node 6 also falls off the glacier, seen in the sharp decline in height at the end of the node's life and represented by an increase in GPS height beginning on the calving event on DOY 206 at 3 am, leading to the uplift of ~0.9 m, then a drastic fall coinciding in time with the calving event.

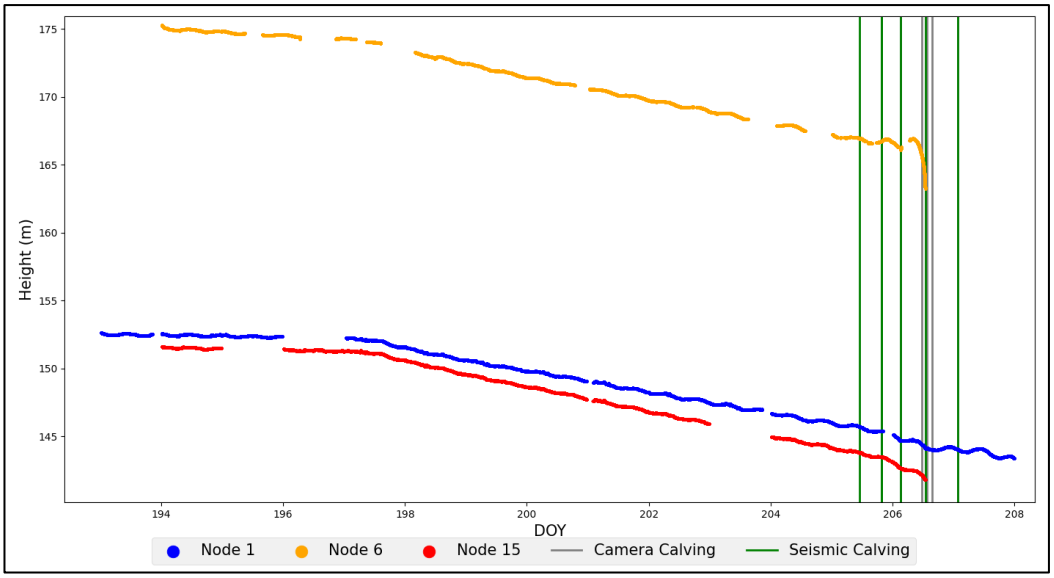

Figure 4:16, GPS height data for nodes 15 (red), 1 (green) and 6 (yellow) all decreasing over time.

Nodes 1, 6 and 15 also show similar tidal modulation in height starting around DOY 198 (Figure 4:17). Nodes 1 and 15 have an M2 amplitude of 0.05 m, and Node 6 at 0.07 m. Nodes 1 and 6 slowly increase M2 amplitude, reaching 0.14 m (node 1) and 0.15 m (node 6). Node 15 does not increase as much but slowly increases, reaching 0.75 m before peaking at 0.1 m. In all three nodes, K1 only appears at the beginning, where there are large amounts of data gaps or at the end, where the nodes either see significant decreases in height or stop working.

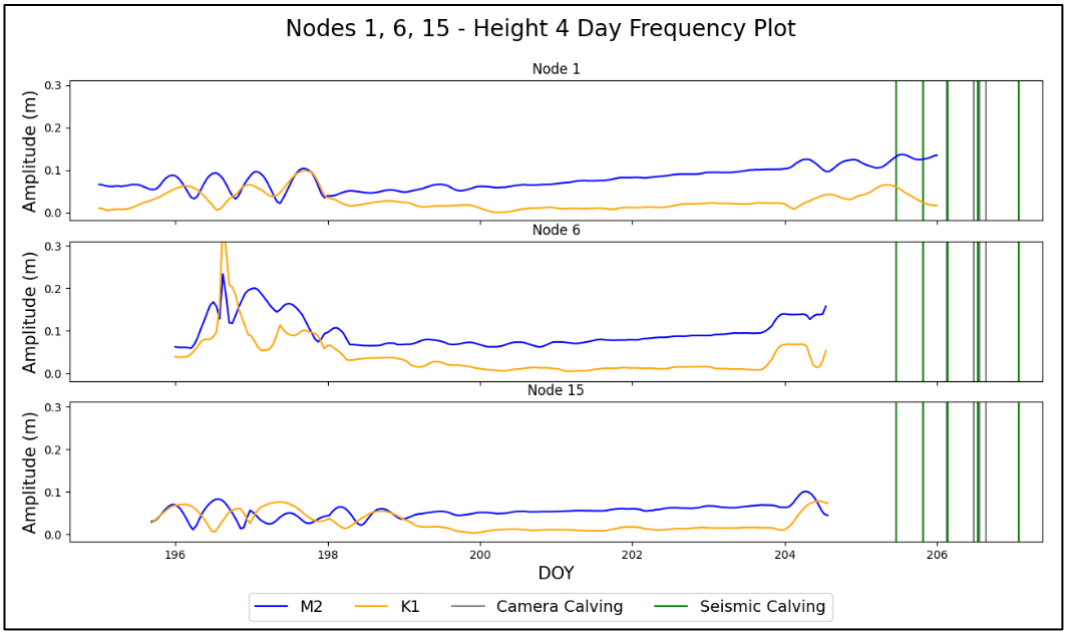

Figure 4:17, Moving Power graph for Nodes 15, 6, and 1, each graph showing each node, in blue the M2 and orange K1. Note that the K1 spike in node 6 is spurious and from the data gaps.

Node 8 goes through 3 long-term phases (Figure 4:18). Initially, the elevation falls from 183.3 m to 117.8 m over 17 days, coinciding with a calving event picked up by both the cameras and seismic data. During this period, node 8 is falling at a rate of 0.3m/d. When the calving event on DOY 211 arrives simultaneously, there is a stalling where height stays relatively the same for the next 17 days. Node 8 height is dropping on average by 0.1 m/d. Then, around DOY 231, another phase of increased lowering occurs until the loss is around DOY 237, with a final height of 172 m. The final stage saw a decrease in the height of 1.5 m/d. The tidal amplitude for node 8 is variable. It goes through 3 stages in time with the calving events and height state changes (Figure 4:19), with the maximum M2 amplitude occurring at the end at 0.03 m, but there is a considerable amount of inclusion of other constituents and is not clear compared to other nodes, e.g. 1, 6, 9. For example, K1 is consistently below M2, and then during the calving events around DOY 210-213, K1 becomes the dominant forcing but changes regularly.

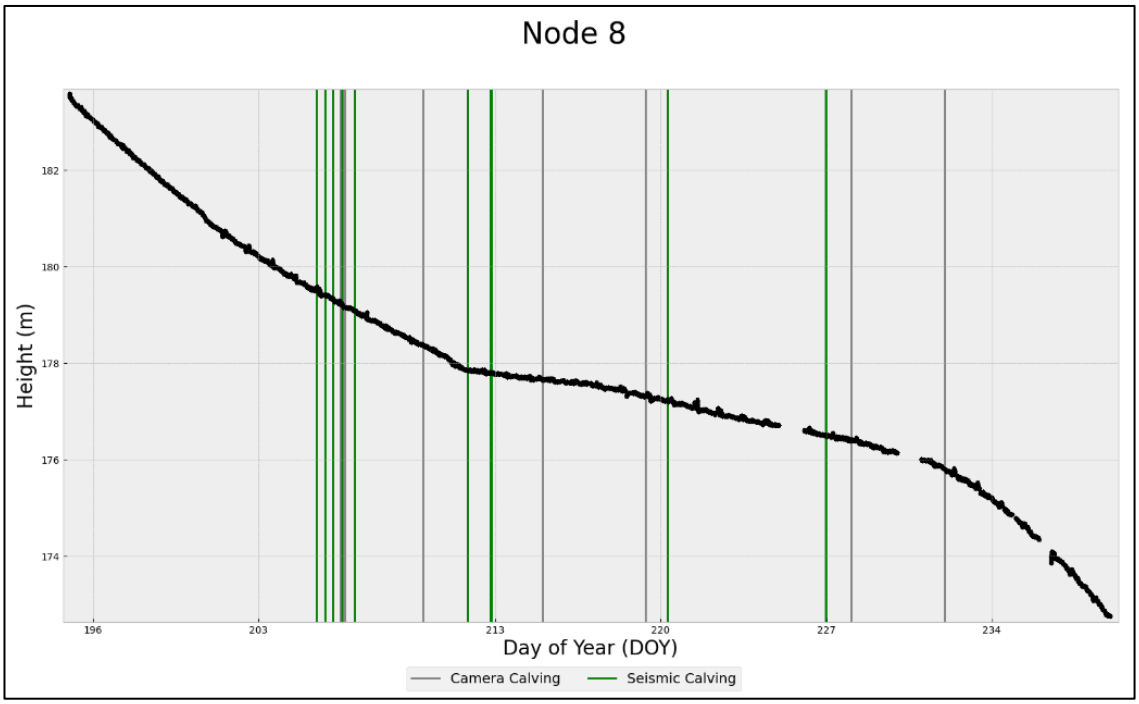

Figure 4:18, Node 8 height for the full-time period spanning 45 days, alongside the camera and seismic calving events.

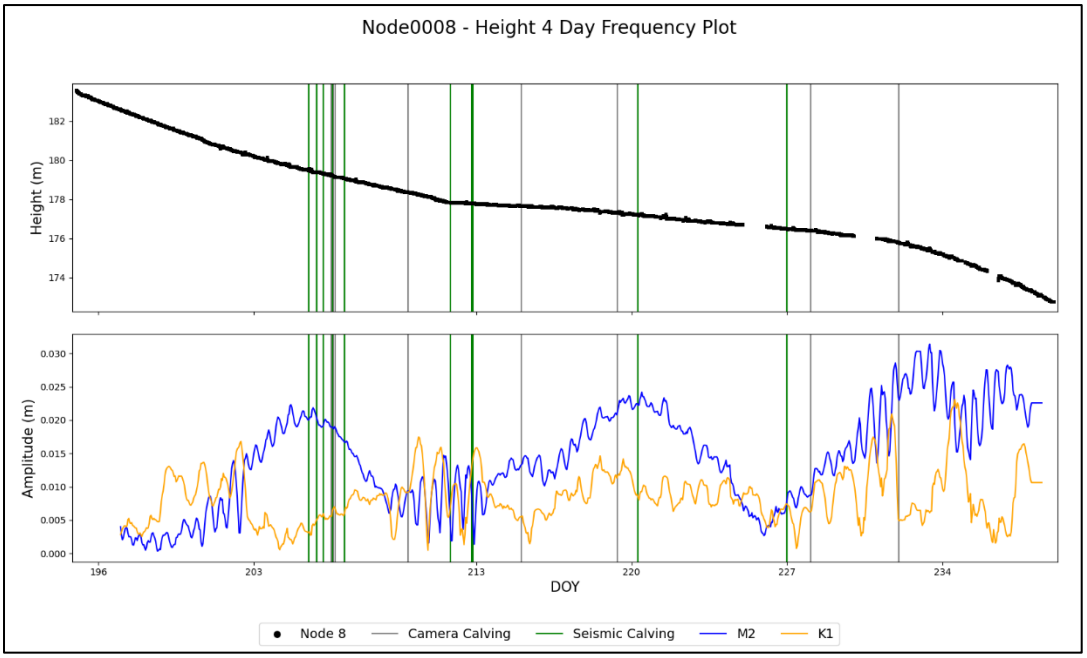

Figure 4:19, Moving Power graph for node 8, showing height (black) and the resulting M2 (blue) and K1 (orange) amplitudes (m) from the 4-day moving power graph in U-Tide.

Node 9 has proven to be very interesting and has been discussed extensively by Murray et al. (2015). Unlike nodes 1 and 6, node 9 has a prolonged existence with multiple calving events altering its height regime (Figure 4:20). It undergoes two main phases: an initial phase starting at 152.2 m with a consistent decrease in height until a calving event on DOY 211, resulting in a 4.7 m lowering over 18 days (0.26 m/d). Following this, a second phase begins on DOY 212, characterised by continuous height increase synchronised with a tidal signal, raising the height by 4.2 m over seven days (1.6 m/d increase). A seismic event on DOY 219 coincides with a 0.9 m height decrease the next day. Another calving event causes a significant stepwise height increase, from 151 m to 153.5 m over a single day.

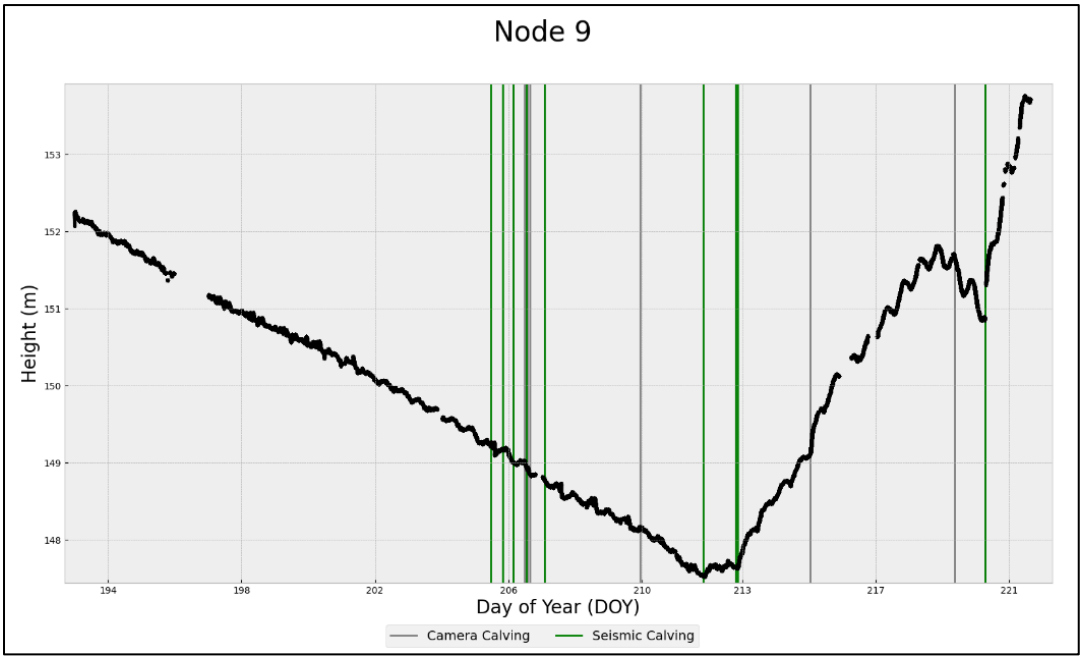

Figure 4:20, Node 9 height for the full-time period spanning 45 days, alongside the camera and seismic calving events.

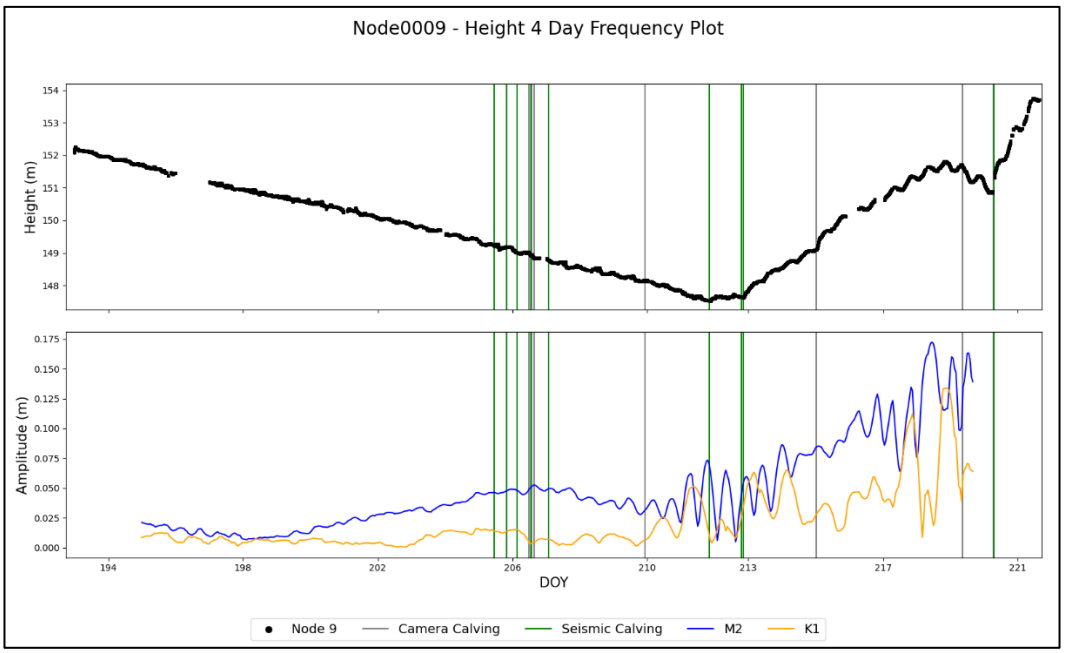

Figure 4:21, Moving power graph for node 9, showing height (black) and the resulting M2 (blue) and K1 (orange) amplitudes (m) from the 4-day moving power graph in U-Tide.

Contained within these changes in height, node 9 has a clear tidal signal (Figure 4:21) starting at DOY 198 and progressively increasing in amplitude. From DOY 202, a small visual semi-diurnal modulation, reflected in U-Tide, from DOY 198 M2 amplitudes increase from 0 to 0.05 m, followed by a period of amplitude decrease. In line with the changing state of height, from falling to stable. Once the height increases from DOY 214, M2 has a clear signal

with an amplitude of 0.07 m, rising over time and peaking at 0.17 m. However, the calving event of DOY 220 introduces variation, leading to increased noise in U-Tide's output.

Node 13 goes through 3 phases: rising and lowering and then rising again (Figure 4:22). Firstly, from DOY 197 to 211, the node increases from 175.1 m to 175.7, an increase of 0.6 m over 14 days. Then, the second phase starts around the calving event in DOY211. Height lowers from 175.7 to 171 m over 18 days, ~20 cm per day. The final stage sees a rise back in height to ~171 m until the node is lost. Over the whole period visually, there is a visual daily tidal signal with a low frequency.

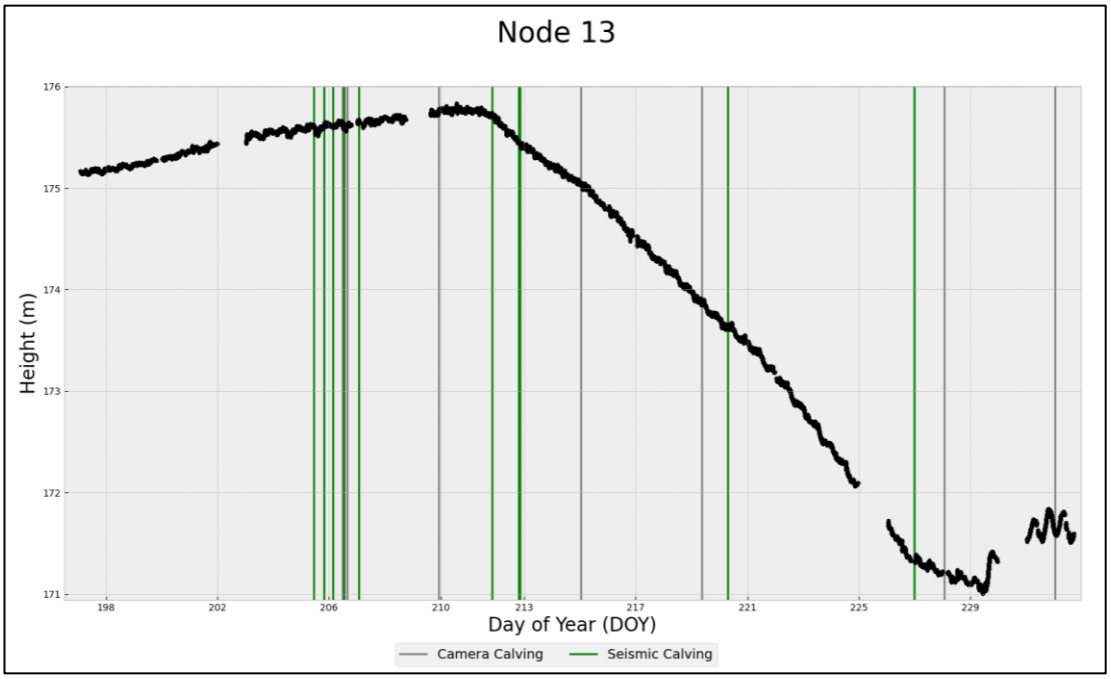

Figure 4:22, Node 13 height data in red is the cleaned Kalman filter data and in black is the original GPS data with the preprocessing variables removed.

Node 13 starts with an M2 amplitude of 0.01 m (Figure 4:23). As it increases in height, the amplitude also increases, peaking at 0.02 m alongside K1, peaking at 0.01 m. As time passes, the tidal modulation falls around DOY 210-216. There is no discernible modulation of a specific constituent apart from a brief period where K1 has an amplitude of 0.02 m. From DOY 217, M2 is again discernible, starting at 0.01 m and slowly increasing to 0.03 m, and the node falls in height. K1 is also evident at ~0.01 m. During the calving events around DOY 228, many data gaps are causing a significant variation in U-Tide outputs; however, from day 231, visually, there is a clear semidiurnal signal, and U-Tide shows this M2 signal has a peak amplitude of 0.13 m.

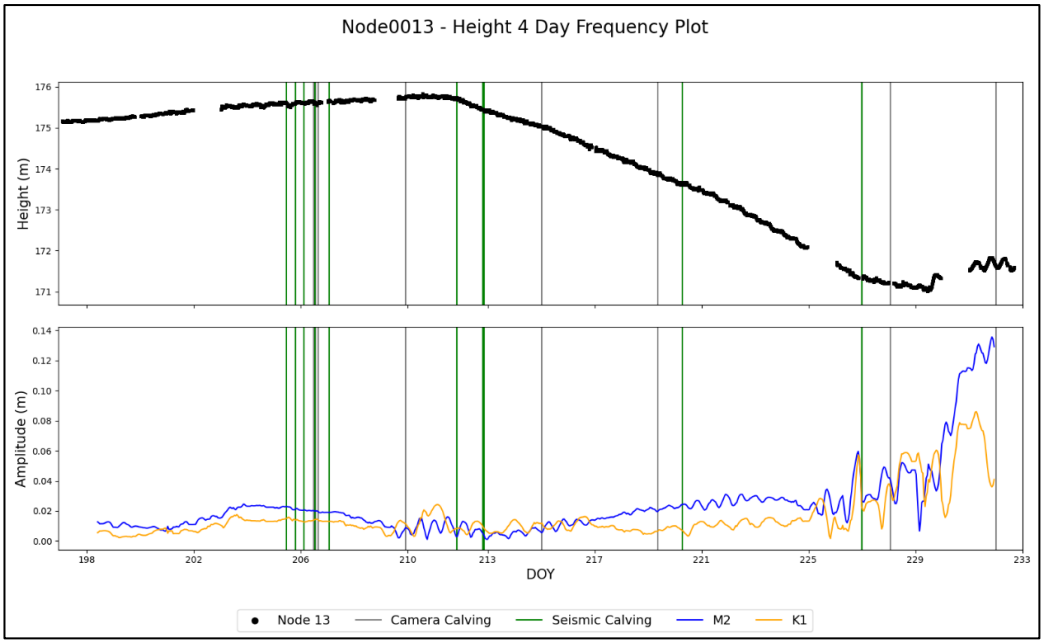

Figure 4:23, Moving power graph for Node 13, showing the original height data after pre-processing (black), the cleaner data (red) and the resulting M2 (blue) and K1 (orange) amplitudes (m) from the 4-day moving power graph in U-Tide.

Node 20 has 2 phases (Figure 4:24); DOY 194 to 211 height reduces 14 m over 17 days (0.8m/d decrease). The second phase starts DOY 212 at 176.3 m, falling to 157.6 m on DOY 220, totalling 18.7 m over eight days, the fastest reduction rate in height at 2.3 m/d. There is also no visual tidal modulation. Node 20 is also the only node where M2 has no discernible control in height. The periods with large amplitudes occur during data gaps and calving events that disrupt the long-term flow.

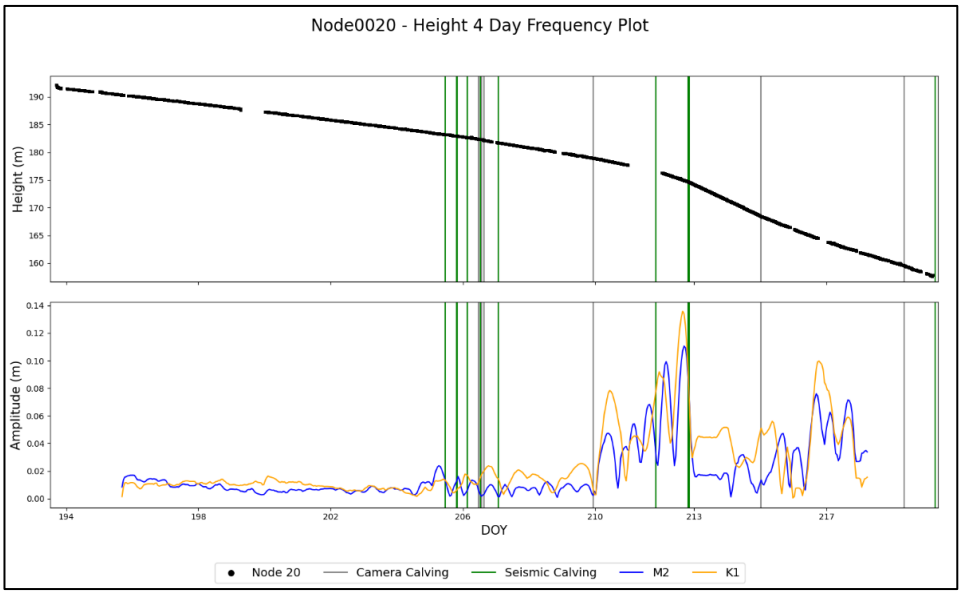

Figure 4:24, Moving power graph for node 20, showing the height data (black) and the resulting amplitudes (m) from the 4-day moving power graph in U-Tide.

4.3.3 Fortnightly Tidal Signal

When the nodes last long enough, there is an apparent amplitude on the M2 signal varying on a fortnightly time scale, this is found in both the Horizontal velocity and the Height data. Figure 4:6 shows increasing and decreasing M2 amplitude cycles for horizontal velocity. When comparing just nodes 8 and 3 (Figure 4:25), the longest-lasting nodes, you can see the changing M2 signals align with each other over a fortnightly cycle. This a~~A~~pparent signal is also evident in most nodes, (

Figure 4:26, Figure 4:27), with some not showing the cycle (node 9); however, this node is highly affected by the calving events. The amplitude of the M2 signal is largest at spring tides when the forcing is bigger (springs) and lower when it is lower (neaps).

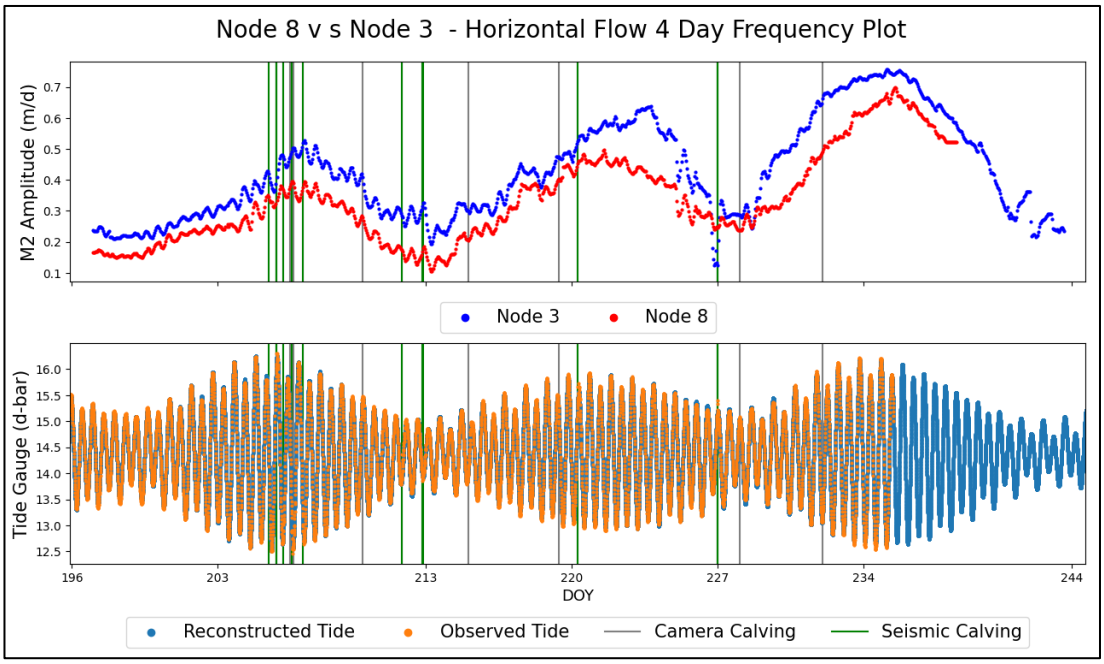

Figure 4:25, Horizontal flow velocity M2 amplitude of node 8 (red) and node 3 (blue) alongside the predicted tide gauge (blue) and the recorded (orange), showing a potential spring neap cycle of M2 amplitude.

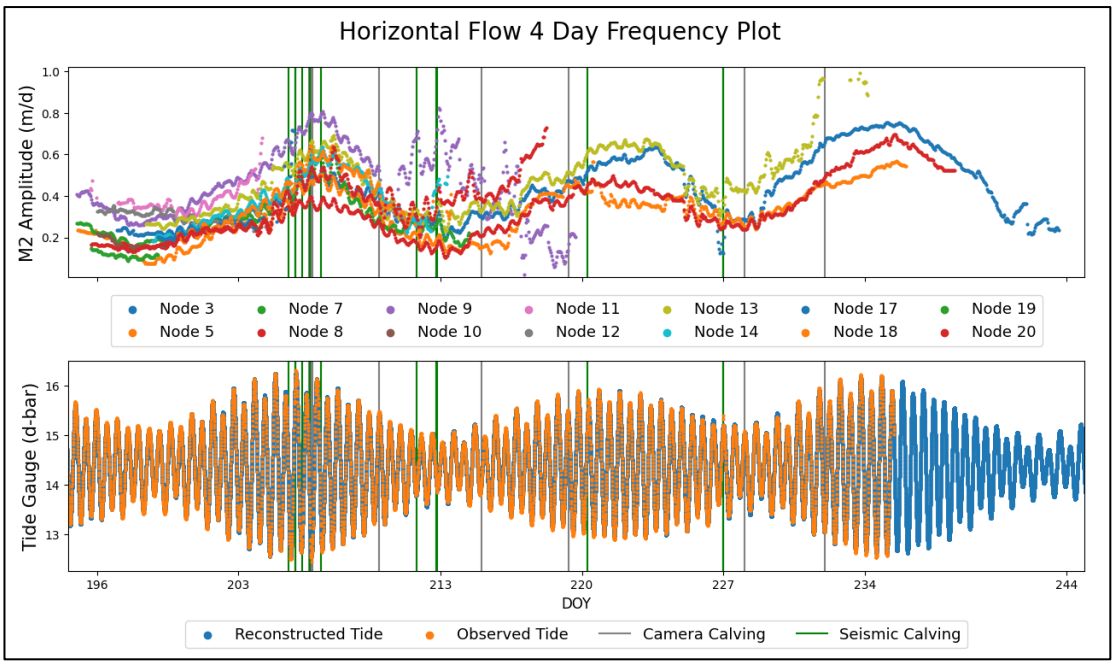

Figure 4:26, Horizontal flow velocity M2 amplitude of GPS nodes alongside the predicted tide gauge (blue) and the recorded (orange), showing a potential spring neap cycle of M2 amplitude.

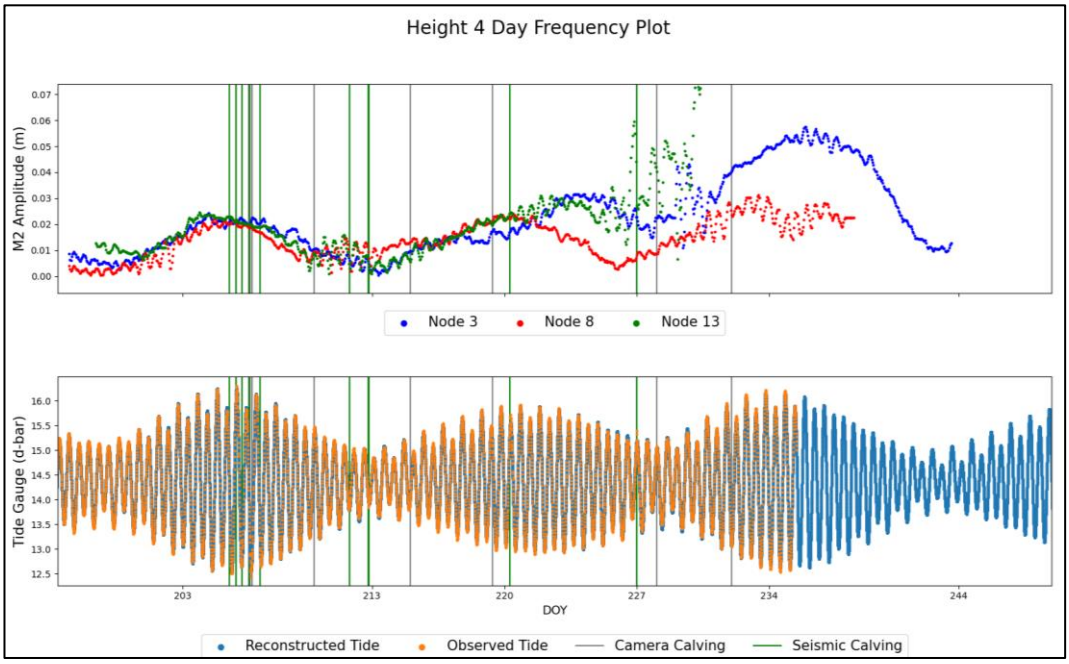

Figure 4:27, Height M2 Amplitude of node 8 (red), node 3 (blue) and 13 (green) alongside the predicted tide gauge (blue) and the recorded (orange), showing a potential spring neap cycle of M2 amplitude.

As a result of the findings, a test was conducted on the original tide gauge data set. This test revealed apparent fortnightly amplitude variations in the M2 signal, following a pattern similar to the spring-neap cycle (Figure 4:28). The 4-day window methodology as described in "3.3.4 Tidal Signal Through Time – Moving Power Graphs", was designed to isolate the M2 tide. However, the observed fortnightly variations in M2 amplitude in both the GPS and

original tide gauge data indicate a limitation of the 4-day window approach. This methodology is not able to accurately separate tidal constituents, although it does identify the presence of the semi-diurnal signal.

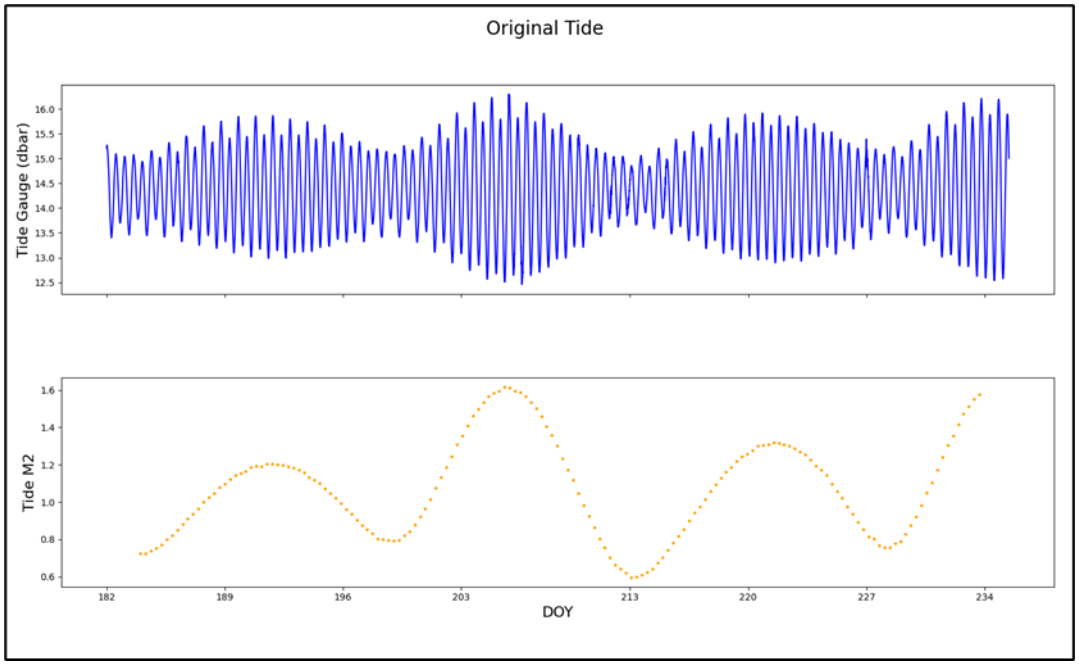

Figure 4:28, Tide Gauge Data (top) and the resulting varying M2 Signal (bottom) from the 4-Day Moving Power Graphs.

4.4 Glacier Flow and Calving Events

4.4.1 Introduction

Fourteen of the 20 GPS nodes recorded usable data during calving events. The first identified calving event recorded alongside the GPS network occurs in DOY 205, with the final calving event occurring on DOY 232. There are two main periods where calving events affect flow on nodes across the network. The first is around DOY 205-207 with eight events, tThree identified from cameras and five from the seismic, which are not independent. The three-camera calving events cluster around one seismic calving event on DOY 206. The second critical period they occurred was around DOY 211-215, with three independent calving events picked up from the seismic data.

4.4.2 DOY 205-207

4.4.2.1 Distance from terminus.

The GPS node's distance from the calving front is determined using terminus position data from (Goliber et al., 2022), enabling an understanding of how close each node is to the glacier front. Nodes 4, 17, 10, 11, 12, 19 stopped data collection before DOY 206. The rest either stopped working during this first period or continued. Node 11 stopped data collection during the third recorded calving event (Figure 4:13) and was the closest node to the calving front until it stopped operating (Figure 4:29). Nodes 6 and 15 also stopped data collection during this period. During this period, the tidal gauge records the highest peaks and lowest troughs of high and low tide associated with the spring neap cycle.

25/07/2013	
Node	Terminus distance (km)
11	-0.6
6	-0.15
1	0.046
15	0.056
9	0.9
14	1.12
20	1.13
13	1.74
18	1.94
3	2.03
7	2.61
5	2.93
8	3.1
2	n/a
4	n/a
10	n/a
12	n/a
17	n/a
19	n/a

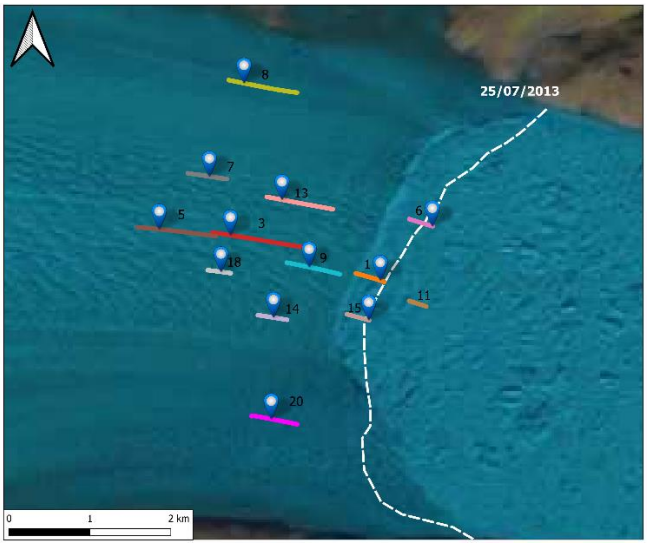

Figure 4:29, Surviving nodes as of 25th July 2013 (DOY 206), in the coloured lines, are their total path, and the pins show where the nodes are at the end of the day (18:00) on 3rd August 2013 (DOY 213). Furthermore, a Table of Each node's approximated distance from the calving front, identified from TermPicks (Goliber et al., 2022) and from the calving front on 25th July 2013 (DOY 206) at ~2 pm from Landsat 7 highlighted in green are the nodes that are beyond the calving line, this is likely due to the ~100m error in terminus position identification (Goliber et al., 2022) and the difference between the accuracy of the GPS data.

4.4.2.2 Calving event – DOY 205

Two calving events occurred on DOY 205, the first at 11 am, identified through the seismic data with no nodes reacting to this event (Figure 4:30) occurring during the falling tide. In the second calving event at 19:40, Nodes 1, 6, 11 and 15 show significant flow speed increases at high tide. Node 1 stopped working ~30 minutes after the calving event. Node 11 has the most extensive reaction to the calving event, with a 28.5% increase in flow from before to after the calving event. Node 11, from the recorded point at 18:00, begins to decrease in flow speed. The increase in flow speed from the calving event start becomes 30%. At the same time, the height for node 11 increased from 141.8 m to 143 m at 22:45,

~45 minutes after flow speed peaks. Five hours after node 11 settles to a flow of 28.8 m/d, a 9.2% increase in flow speed compared to before the calving event.

Nodes 6 and 15 have similar responses to the calving event, with increases in speed at 17.6% (node 6) and 20.8% (node 15) (Table 4:4). Node 15, with the faster response, also peaks earlier than node 6 by ~1 hour and begins to decrease in flow speed before there is a data gap. Once the node is again producing reliable data, flow is ~8.9% larger than before the calving event. Node 6 takes longer to peak but does not see a decrease in flow speed afterwards, only falling to 18.27 m/d. The calving event has led to a 16.3% increase in horizontal flow compared to horizontal flow before the caving event. Nodes 15 and 6 showed no significant changes in height during this time (Figure 4:31).

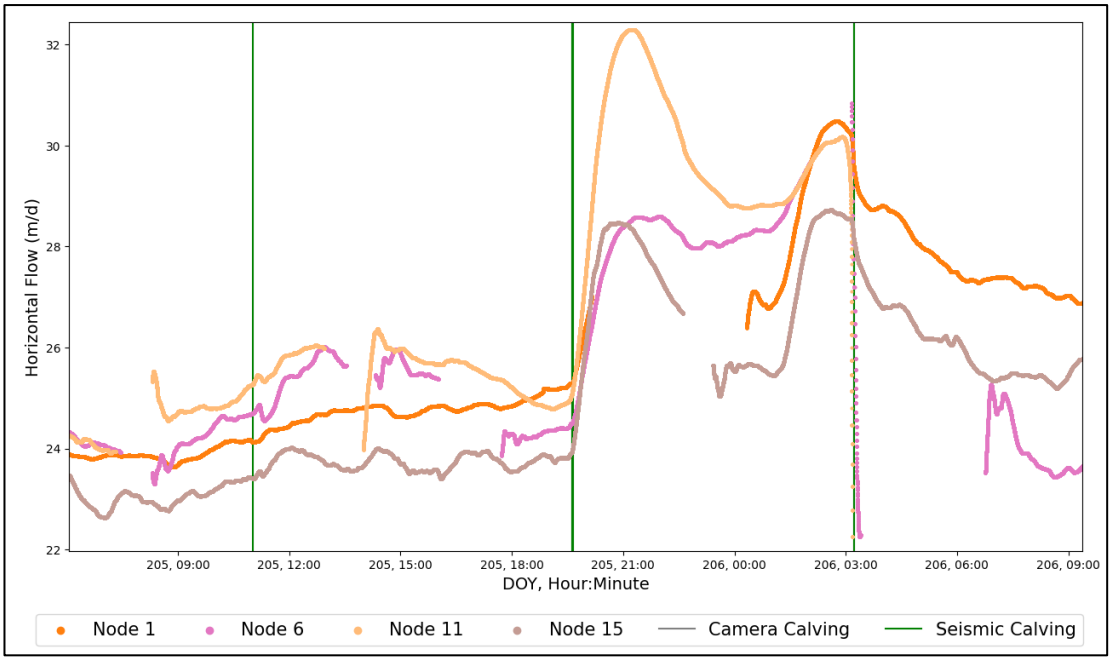

Figure 4:30, Calving events on DOY 205 and morning of 206, showing the horizontal flow (m/d) of nodes 1, 6, 11 and 15, the closest nodes to the calving front.

Table 4:4, Node horizontal flow before the DOY 205 calving event, peak flow speed recorded after the calving event alongside the time it takes to reach peak flow. Then the flow speed (m/d) is 5 hours after the calving event.

Calving event 205				
Node	Before	Peak flow speed		5 hours after calving
	Horizontal flow Speed - 18:00	Time to peak flow (Hour:Minute)	Horizontal flow Speed	Horizontal flow Speed - DOY 206 00:25
1	24.8	n/a	n/a	27.1
6	24.3	03:57	28.6	28.27
11	25.2	03:12	32.4	28.79
15	23.5	02:52	28.4	25.6

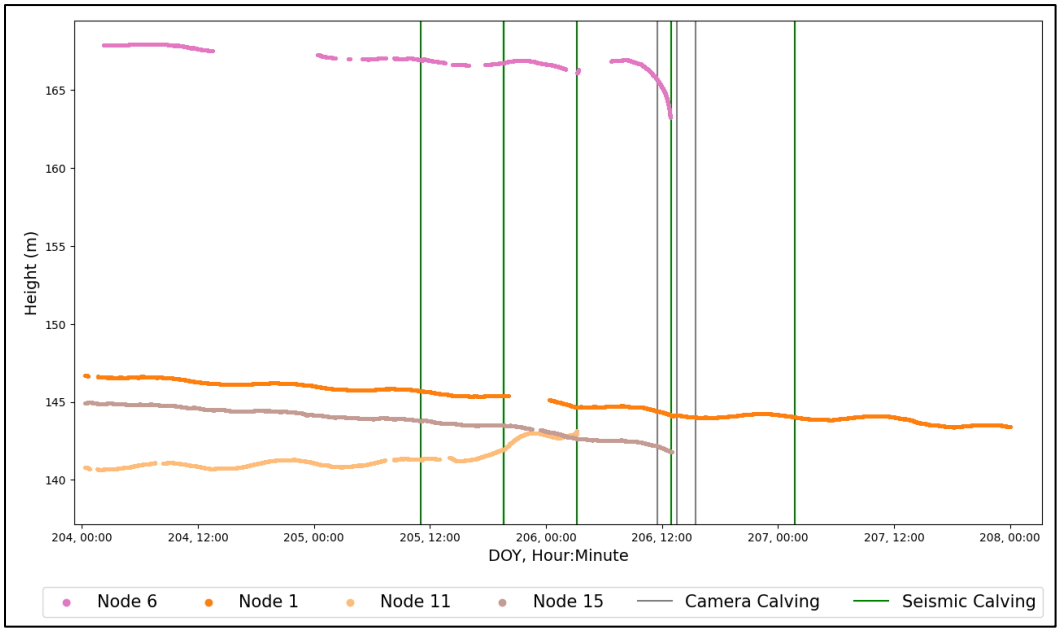

Figure 4:31, Calving events on DOY 205 and morning of 206, showing the height (m) of nodes 1, 6, 11 and 15, the closest nodes to the calving front.

4.4.2.3 Calving event – DOY 206

After the calving event of 205 on DOY 206 at ~00:30, Nodes 1, 6, 11 and 15 all begin to increase flow speed, peaking at 02:40 (Figure 4:30), then start to fall just at the initiation of the first calving event of DOY 206, resulting in the loss of node 11, which speeds up from 28.8 m/d to 30.1 m/d 10 minutes before the calving event that leads to its demise, you can also see the changes in height falling before its loss during the calving event at 03:15. Nodes 15 and 1 (25.4 – 28.7). Node 1 saw a 14.2% increase in speed leading to the calving event, and node 15 (13%). The remaining nodes bottom out at ~9 am, with node 6 being ~1 m/d slower than the calving events before DOY 205. The calving event associated with this occurred at the end of low tide.

There is a camera calving event recorded at 11:30 (occurring during the middle of the falling tide), of which there are no drastic immediate changes apart from the start of the data nodes 1, 6 and 15 all begin increasing in flow. By the second calving event identified by the seismic network and cameras, all three nodes had peaked flow and sharply slowed down (occurring closer to low tide). Node 6 peaked at 39.4 m/d 10 mins before the calving event, and flow slowed drastically until node 6 stopped communicating two minutes before the recorded calving event. Node 15 also peaks and drastically falls before also being lost. Node 1, on the other hand, is flowing slower at ~29 m/d at its peak, dropping to 27.6 m/d at the calving event, then drastically increasing flow speed, peaking at 36.21 m/d as the node

increases in flow speed. Then, as flow falls, another camera calving event is recorded with no impact as the flow continues to slow, levelling out at 29m/d (Figure 4:32).

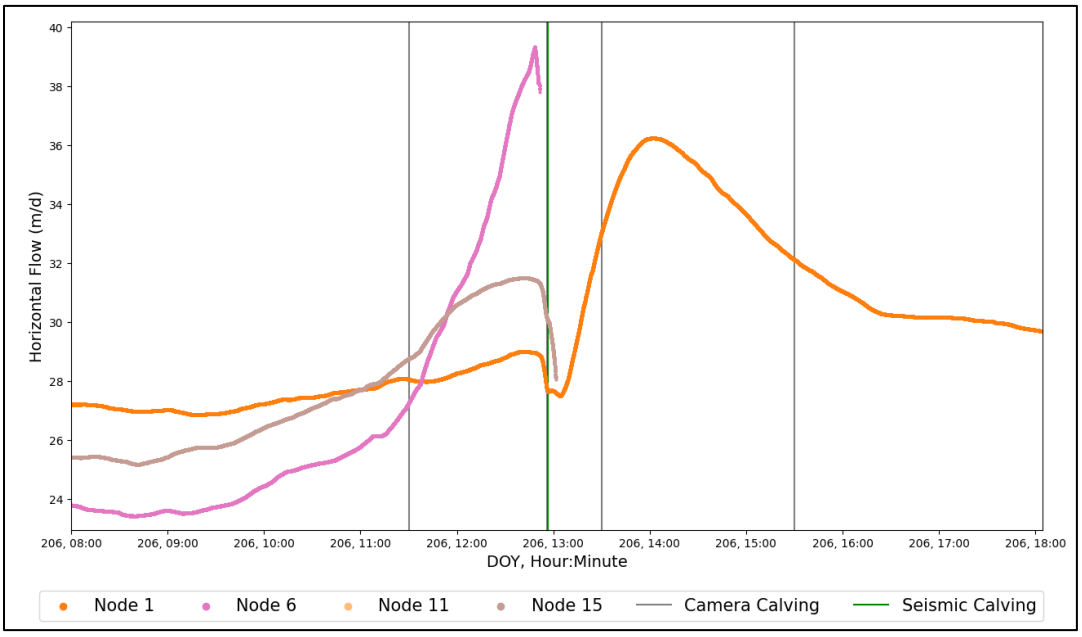

Figure 4:32, Calving events on DOY 206, shows the horizontal flow (m/d) of nodes 1, 6, 11 and 15, the closest to the calving front.

4.4.2.4 Calving event – DOY 207

The next calving event occurred on DOY 207 at 01:43. After the dramatic loss of nodes 1, 6, and 11 over the previous two days occurring just before low tide. Node one is the closest node to the calving front (~180 m). After dropping out to 29 m/d, node 1 slowly speeds up to 30.2 m/d. Node 1 again drastically increases flow speed by 02:50, peaking at 36.1 m/d, a 19.5% increase in flow speed over ~1 hour (Figure 4:33). Like the previous calving events, flow speed slowly decreases to 31 m/d over the next 6 hours. Node 1 then increases to 39.2 m/d. Then, it stops sending data. This last increase is unexplained in terms of calving events. The height for node 1 appears unaffected by the calving events (Figure 4:31).

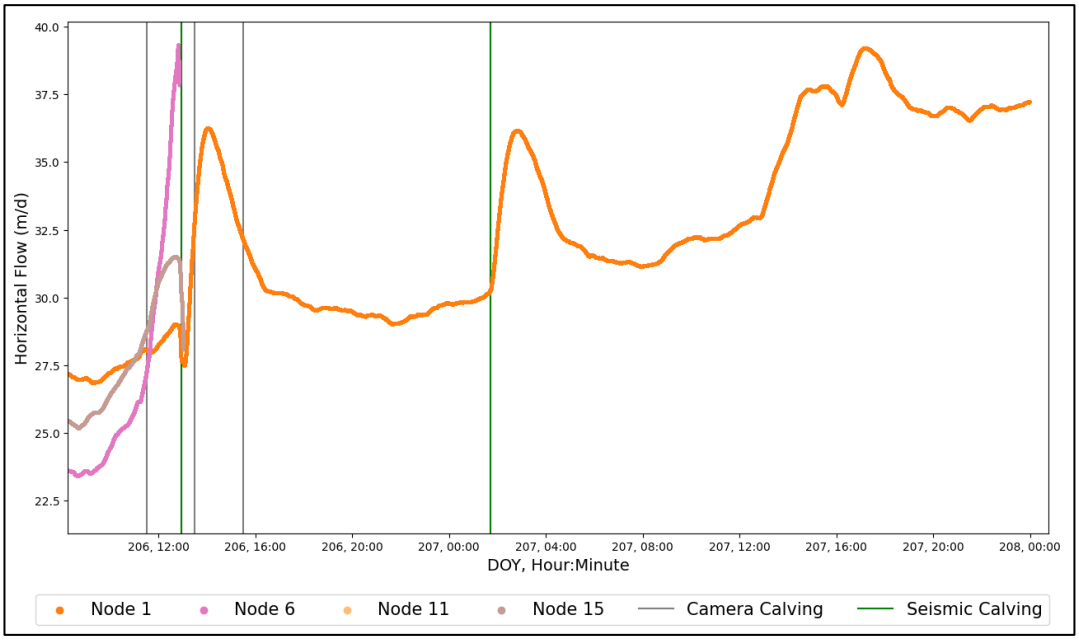

Figure 4:33, Calving events on the morning of DOY 206 and DOY 207, showing the horizontal flow (m/d) of nodes 1, 6, 11 and 15, the closest nodes to the calving front.

4.4.3 DOY 211-215

4.4.3.1 Distance from terminus.

After the first period of calving events where nodes 1, 6, 15, and 11 were lost, many others stopped working, leaving only seven (3, 5, 7, 8, 9, 13, 20) (Figure 4:34). A second set of calving events occurred on DOY 211 (30/07/13), 212 (31/07/13) and 215 (03/08/13) (Figure 4:35). As with the previous calving events, many nodes stop working during these calving events. Of the surviving nodes, node 9 was the closest to the calving front on DOY 213 and virtually in Helheim Glacier's centre (Figure 4:34). Before being lost, it was ~150 m from the calving front as of DOY 215. Node 8 was the furthest from the calving front at ~2.23 km. All nodes that survived also showed some reaction to these calving events with varying magnitudes. Node 18 became functionally useless after DOY 211. This period identified by the tide gauge is during the neap portion of the tidal cycle associated with smaller peaks and troughs of high and low tide.

03/08/2013	
Node	Terminus distance (km)
9	0.15
20	0.62
13	1.07
3	1.26
7	1.69
5	2.00
8	2.23
19	n/a
18	n/a
17	n/a
15	n/a
14	n/a
12	n/a
11	n/a
10	n/a
6	n/a
4	n/a
2	n/a
1	n/a

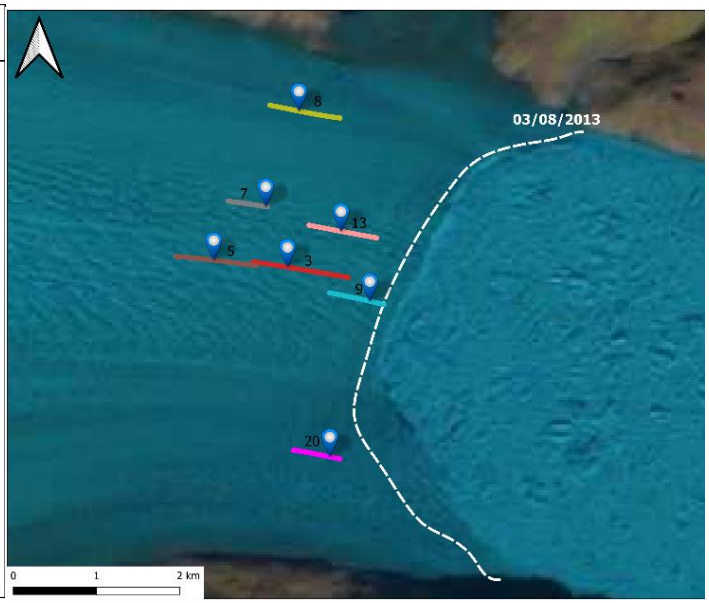

Figure 4:34, Surviving nodes as of 3rd August 2013 (DOY 213), in the coloured lines, are their total path, and the pins show where the nodes are at the end of the day (18:00) on 3rd August 2013 (DOY 213). Furthermore, a table of each node's approximated distance from the calving front was identified from TermPicks (Goliber et al., 2022) and the calving front on 3rd August 2013 (DOY 215) at ~2 pm from Landsat 7.

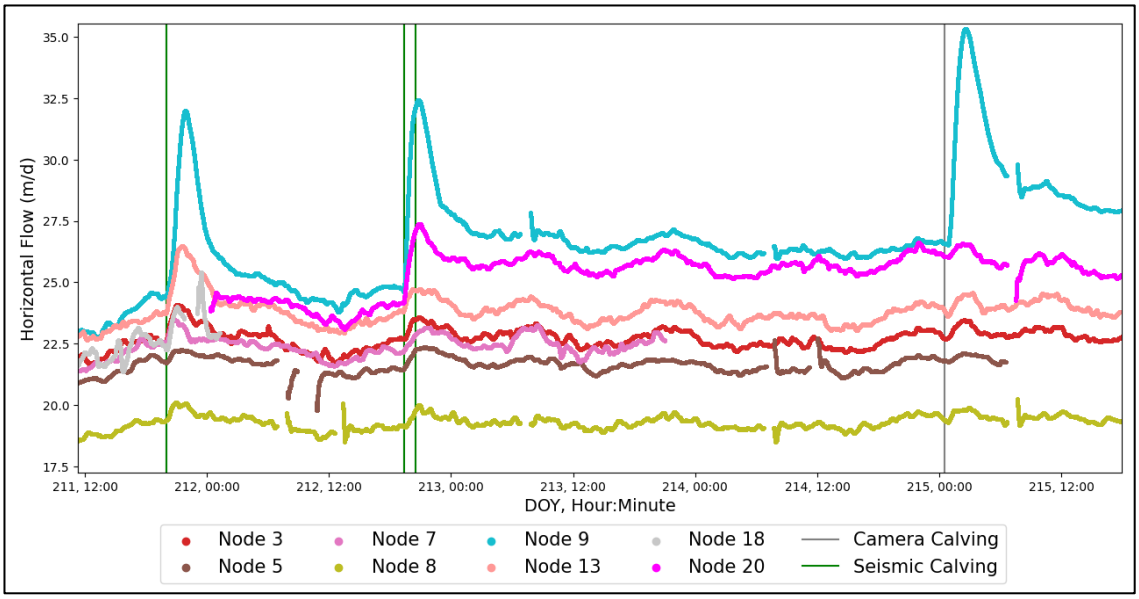

Figure 4:35, Horizontal flow (m/d) around DOY 211 - 215, showing the three calving events. Each coloured line shows a different node. Some work well most of the time (node 8 - green), and others have gaps. For example, node 20 (light purple) is missing in the first calving event (DOY 211) but turns back on shortly afterwards.

4.4.3.2 Calving event – DOY 211

The first calving event on DOY 211 is identified in the seismic data at 20:01 and recognised by the cameras at 20:00. In order of response to the calving event, nodes 9, 13, 3, 7, 18, 5 and 8 show some increase in flow speed as a direct result of the calving event (Figure 4:36), occurring soon after low tide.

Node 9, the closest to the calving front, had the fastest horizontal flow at 24.5 m/d (Figure 4:34 and Figure 4:35). Its flow speed also had the highest percentage change during the calving event, with peak flow speed increasing by 30.6%. The subsequent most significant increase in flow speed is node 13, with 11.6%. Nodes 3, 7 and 8 also show direct increases in flow speed. However, much less (4.4% - 8.1%). Nodes 5 and 8 show much lower increases again. There are still increases in the flow of 2.3% (node 5) and 3.6% (node 8). Nodes 9, 13 and 3 saw longer-term increases in flow speed 9 hours after the calving event (3.2% - node 9, 1.52% - node 13 and 2.22% - node 3). Nodes 8 and 7 show virtually no change, with an increase of 0.5% and node 7 not changing. Node 5, however, saw a fall in flow speed compared to the pre-calving flow speed with a 2.3% decrease (21.7 m/d to 21.2 m/d).

Table 4:5, Node horizontal flow before the DOY 211 calving event, peak flow speed recorded after the calving event alongside the time it takes. Then the flow speed (m/d), 9 hours after the calving event.

Calving event 211				
Node	Before	Peak flow speed		9 hours after calving
	Horizontal flow Speed - 19:55	Time to peak flow (Hour:Minute)	Horizontal flow Speed	Horizontal flow Speed - DOY 212 05:00
9	24.5	01:48	32	25.3
13	23.74	01:32	26.5	24.1
3	22.5	01:02	24	23
7	22.5	00:44	23.5	22.5
18	22.2	01:00	24	n/a
5	21.7	01:31	22.2	21.2
8	19.4	00:53	20.1	19.5

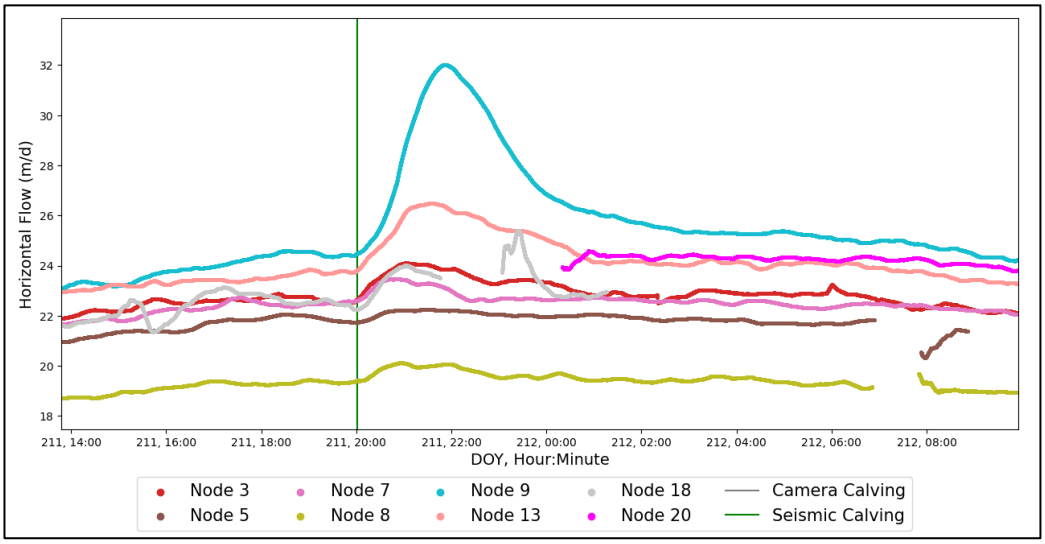

Figure 4:36, Horizontal flow (m/d) around DOY 211, after the seismic calving event, node 9 has the sharpest increase in flow, with node 20 missing data at the calving event and node 18 losing data after the calving event.

4.4.3.3 Calving event – DOY 212

Two calving events occurred on DOY 212, first at 19:21, then another at 20:28 (Figure 4:37). This first calving event occurred just before low tide and the second just after. All nodes show increased flow speed at the first event; however, the second appears to cause no sharp increases in flow. Much like the calving event in DOY 211, Node 9 sees a 31% increase in flow speed, peaking 1 hour 30 minutes after the first calving event, with a slight undulation occurring after, potentially because of the second calving event. Node 20 had the second most significant increase in flow speed (13.5%), taking roughly the same time to peak as node 9, the second fastest node. The rest of the nodes saw increases ranging between 3.6-4.7%. Nodes 13 and 3 levelled out to pre-calving event speeds, with nodes 20 at 7% and Node 9 seeing a 9.3% increase in flow speed (Table 4:6). There appears to be a relation between calving event speed increases and distance from the calving front because nodes 20 and 9 are in front of the rest and saw the most significant increases in flow.

Table 4:6, Horizontal flow before the DOY 212 calving event, peak flow recorded after the calving event alongside the time it takes. Then, horizontal flow 9 hours after the calving event.

Calving event 212				
Node	Before	Peak flow speed		9 hours after calving
	Horizontal flow Speed - 19:15	Time to peak flow (Hour:Minute)	Horizontal flow Speed	Horizontal flow Speed - DOY 213 04:20
9	24.7	01:29	32.46	27
13	23.7	00:53	24.71	23.7
3	22.7	00:58	23.53	22.7
7	22.2	02:22	23.1	22.4
5	21.5	02:04	22.3	21.6
8	19.1	01:39	20	19.3
20	24.1	01:34	27.36	25.8

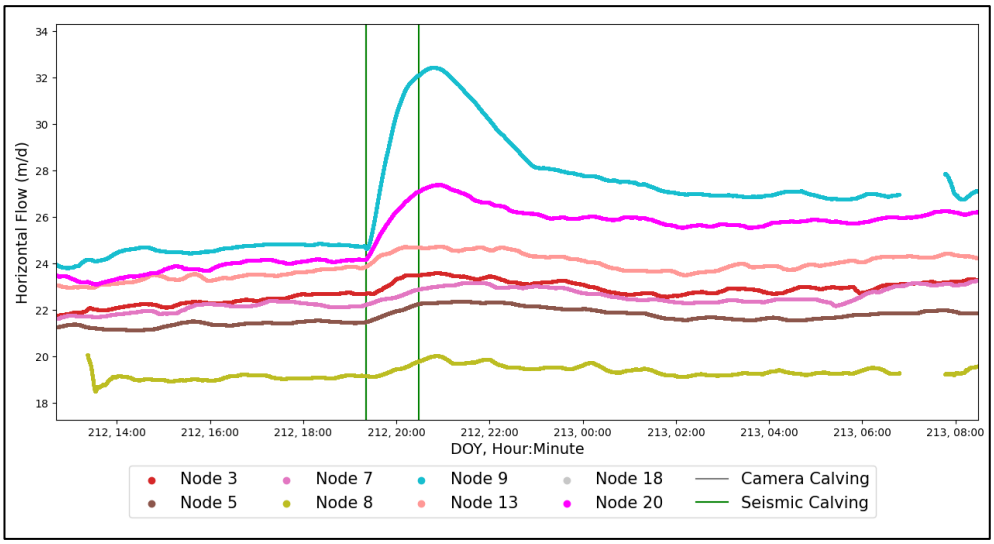

Figure 4:37, Horizontal flow (m/d) around the two seismic calving events on DOY 212, clearly node 9 (light blue) has the sharpest increase in flow, with node 20 (purple) also increasing flow speed.

4.4.3.4 Calving event – DOY 215

The calving event on DOY 215 differs from the previous events found in DOY 211 and 212, in which no seismic data recorded a calving event; the calving cameras identified this event at 12:30 on 3rd August (DOY 215) (Figure 4:38). This calving event occurs after low tide. Interestingly, speed decreases then suddenly increases in response to the calving event. Unfortunately, there is missing data for node 7 at the beginning and node 5 at the end of the calving event. Node 9 sees its most significant increase in flow speed yet, with a 32.7% increase in horizontal flow from pre-calving event to peak flow. With the rest hardly increasing flow speed. After the calving event, node 9 increases flow speed by 8.27%, whereas the rest either marginally increases by <2% or slows down by <1% (Table 4:7).

Table 4:7, Horizontal flow (m/d) before the DOY 215 calving event, peak flow recorded after the calving event alongside the time it takes. Then, horizontal flow 9 hours after the calving event.

Calving event 215				
Node	Before	Peak flow speed		9 hours after calving
	Horizontal flow Speed - 00:00	Time to peak flow (Hour:Minute)	Horizontal flow Speed	Horizontal flow Speed - DOY 212 09:00
9	26.6	02:33	35.3	28.8
13	23.9	03:16	24.5	24.21
3	22.9	02:26	23.4	23
5	21.85	02:22	22.1	n/a
8	19.5	02:56	19.9	19.5
20	26.1	02:10	26.5	25.89

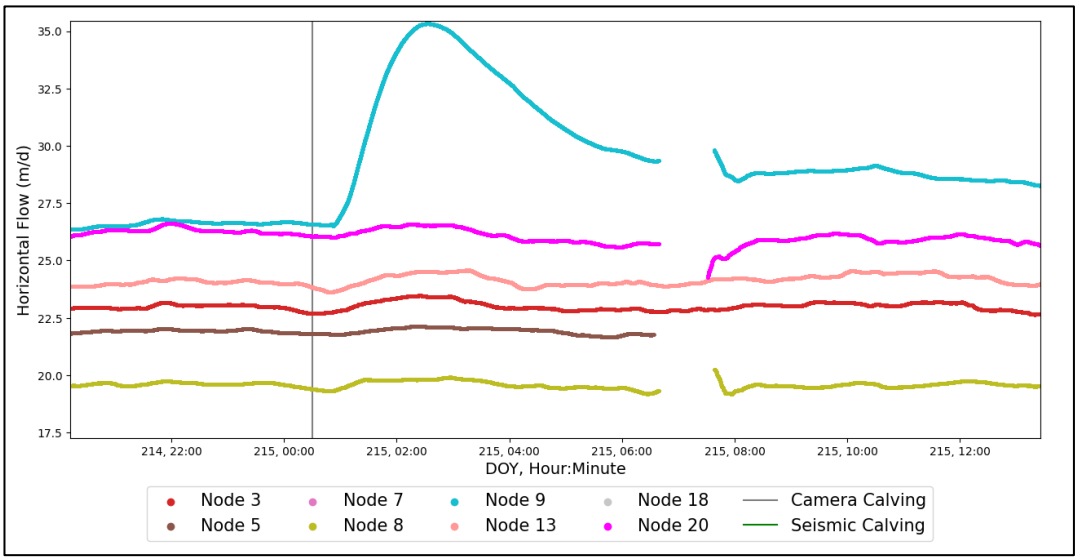

Figure 4:38, Horizontal flow (m/d) around the one camera calving event on DOY 215 node 9 has the sharpest increase in flow, with the other nodes reacting much less.

4.4.3.5 Other Calving Events

On 14th August (DOY 226) at ~11:45, calving events were recorded by the seismic data and the calving photos, occurring at the peak of the neap tidal signal at high tide. Unfortunately, nodes 13 and 3 had data removed during the pre-processing (3.3.1 Filtering GPS). Nodes 8 and 5 had increased flow speed (Figure 4:39). Five hours before the calving event, both nodes slowed down. Flow speed was 22.8 m/d (node 5) and 21 m/d (node 8) (Table 4:8). These values increased at the calving event by up to 8.6 and 9% (nodes 5 and 8, respectively). The horizontal flow never drops back down.

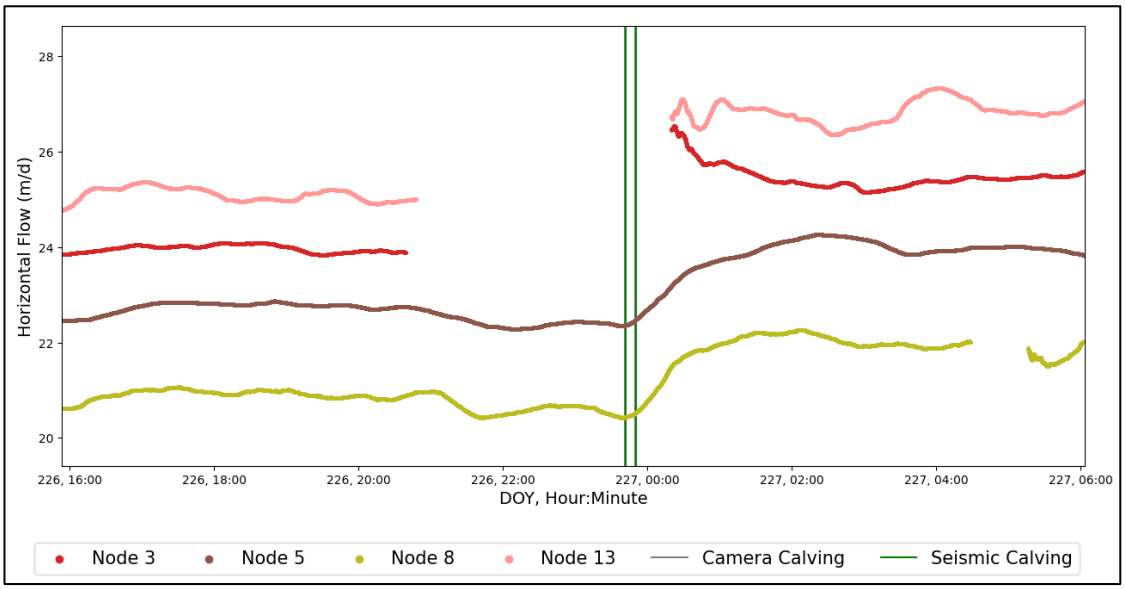

Figure 4:39, Horizontal Flow (m/d) around the seismic calving events on DOY 226, nodes 13 and 3 (pink and red) have data losses; however, nodes 5 (brown) and 8 (green) both show dynamic increases in flow speed.

Table 4:8, Horizontal flow before the DOY 226 calving event, during the initiation of the calving event, then the peak horizontal flow and the time taken since the calving event.

Calving Event 226-227				
Node	Before (m/d) - DOY 226, 19:00	During (m/d) - DOY 226, 11:45	Peak	
			Time to peak flow (Hour:Minute)	Horizontal flow Speed (m/d)
5	22.8	22.35	02:40	24.27
8	21	20.44	02:28	22.275

4.5 Summary of Results

- Helheim Glacier's horizontal flow shows a strong, clear semidiurnal signal.
- Tide Gauge showed classic tidal signals (M2, S2, N2) through U-Tide analysis.
- Different GPS nodes show varying patterns of height changes over time, influenced by glacier flow. Tidal modulation in height occurs, with some nodes showing none and others showing varied amounts of tidal signal.
- Several calving events occurred throughout the study. Depending on the distance to the calving front has led to some nodes exhibiting significant increases in flow speed during calving events.

Chapter 5 – Discussion

5.1 General Results

Deploying GPS nodes at the margin of Helheim Glacier and analysing the results is not easy and there were many challenges around data quality and availability. Despite these challenges, Martin et al. (2014) were able to get 19 out of 20 GPS nodes to collect usable data. The pre-processing and filtering undertaken in this study means that a robust and high-quality data set has been produced. This produced valuable insights into the flow dynamics of Helheim, giving a picture of the dynamics of the marginal area of large outlet glaciers in Greenland and allowing insight into behaviour around calving events and the influence of the tides on terminus behaviour. Node 9 provided the best availability of usable data, lasting for 28.6 days with 91% data availability. Node 18 presented the lowest data availability due to an extended period of data loss (Table 4:1). In the past, other researchers have deployed extensive GPS networks on Helheim Glacier (Juan, 2011; Nettles et al., 2008), focusing on the whole glacier, with only a sparse network of GPS nodes at the calving front.

Helheim Glacier, during the 2013 season, had an average horizontal flow velocity of 16 to 24 m/d at the calving front, with most nodes around 19-22 m/d, aligning with the findings from Nettles et al. (2008), who state that Helheim Glacier's flow can reach ~25 m/d at the calving front. Vijay et al. (2019), also noted that Helheim Glacier has an average flow speed of ~19 m/d.

5.2 Height changes

5.2.1 Height and the Tide

Tidal modulation of height occurs at Helheim Glacier under specific conditions. The tidal modulation increases in amplitude as the distance from the calving front decreases. When looking at node 11 detrended and compared to the tide gauge, visually, there is a correlation, with high tide coinciding with an increase in height; this is slightly delayed with peak height occurring ~2 hours after high tide (Figure 5:1). This is evident across the study, first appearing in Nodes 1,6 and 15 which were close to the calving front (Figure 5:2). After these nodes were lost other nodes took their place at the glacier font and the tidal modulation was still evident. Node 9 shows tidal modulation through both a phase of falling

height (Doy 202-211) and during uplift (213-219) (black periods in Figure 5:3). An explanation for the floating nodes showing semi-diurnal variation in height peaking ~2 hours after high tide could be explained through buoyancy forces and the floating nature of the glacier at the time. As shown in Figure 3:2, the tide gauge is a considerable distance away from the glacier, and there could be a phase delay between the high tide at the tide gauge and the actual high tide occurring at the glacier front.

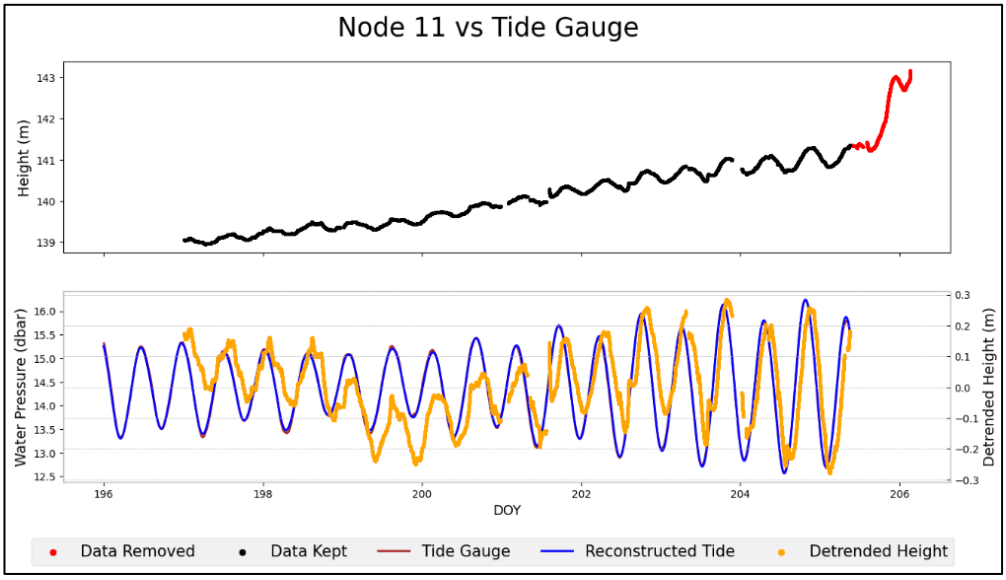

Figure 5:1, Tide gauge data compared to the detrended node 11 height (black), precise semi-diurnal modulation with peaks in height occurring ~2 hours after high tide from DOY 199 – 205 before calving events disrupt the long-term variables.

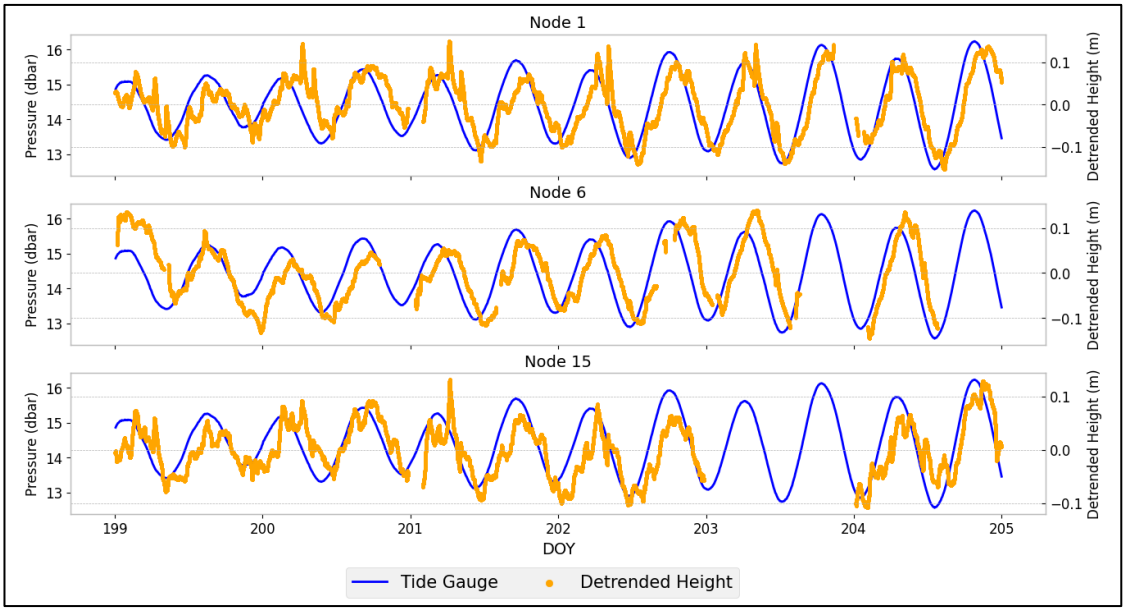

Figure 5:2, Tide gauge data compared to the detrended height for Nodes 1, 6, and 15, showing semi-diurnal modulation with peaks in height occurring ~2 hours high tide from DOY 199 – 205 before calving events disrupt the long-term variables.

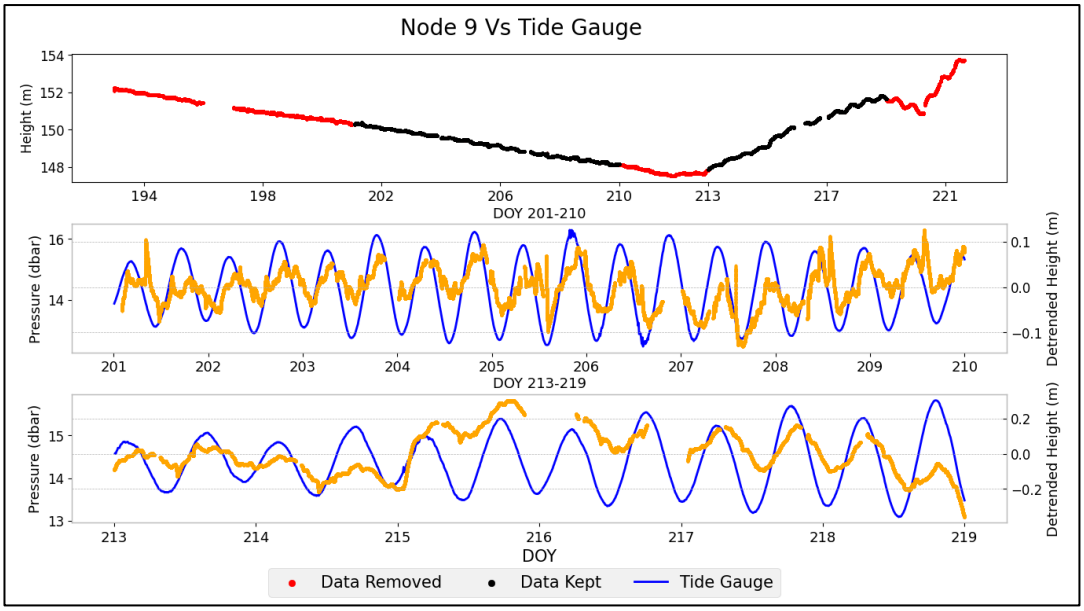

Figure 5:3, Node 9 height (red) split into 2 sections (black) as DOY 201-210 and 213-219. These periods are detrended and compared against the tide gauge in the subsequent graphs. There is precise semi-diurnal modulation with peaks in height occurring during high tide.

The fact that the elevation of Node 11 increases from 139 m to 141.5 m before the calving events (Figure 5:1) while the node is at the front of the glacier, indicates that this potion of ice is probably uplifting (Murray, Selmes et al., 2015). In contrast, nodes 1, 6 and 15 are all on a portion of ice which is flowing downhill and are positioned upglacier of node 11 (Figure 4:29). One explanation for this behaviour is that node 11 is downstream of a flexion zone which leads to backwards rotation of the ice block causing uplift at the very front (Murray, Selmes, et al., 2015). Node 9 also shows a similar regime of height continuously falling until it reaches the front of the glacier and begins to uplift with height increasing from DOY 213. At the same time, the tidal signal increases. These factors suggest that another flexion zone has opened, causing ice downstream of the flexion zone to uplift from buoyancy forces (Murray, Selmes et al., 2015).

5.2.2 Is Helheim Floating

Previous research has indicated that Helheim Glacier has undergone many phases relating to its vertical response to tidal forcing. In 2006 it was identified that a portion of the glacier was floating, this was short-lived as the 2007 and 2008 seasons did not produce data showing variations in height, it was suggested that the glacier tongue was grounded (Juan, 2011). Figure 5:4 displays the M2 Amplitude output from the U-Tide for each node's variation in height. There is a clear distinction between the centre portion of the glacier consistently showing M2 Amplitudes >0.04m. We can infer that these areas are likely floating or semi-floating. Additionally, the remaining nodes were likely grounded at the time

of study. I suggest that during the 2013 study period, Helheim glacier was ungrounded and floating at specific locations where there is tidal modulation in height.

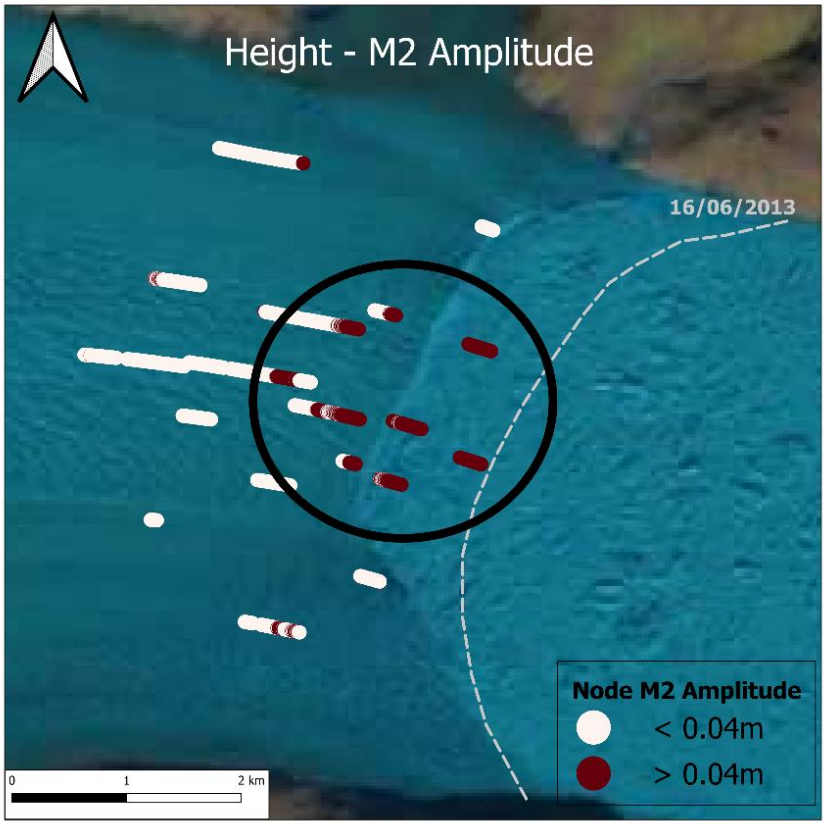

Figure 5:4, Semi-diurnal M2 moving power amplitude for height for each node. Split into two categories, <0.04m and >0.04m, indicating where the glacier is grounded and ungrounded.

5.3 – Horizontal Flow Velocity Changes

Across the GPS network, there is a visual semi-diurnal variation in horizontal flow. U-Tide shows M2 tide as the primary tidal constituent during times with minimal data gaps and periods without calving events disrupting the flow. The M2 amplitude varies in three ranges; the nodes with little to no tidal signal have amplitudes from 0.2 to 0.4 m/d; the nodes with strongest signals during long periods of consistent flow have amplitudes of 0.7-0.8 m/d. The times when M2 amplitude increases beyond 1 m/d correlate with calving events causing large spikes in flow speed in short time frames; these also occur during periods when the nodes are closest to the calving front in the centre of Helheim Glacier, regions where it is theorised that the glacier is floating.

Most nodes see gradual speed increases as they travel down the glacier closer to the calving front. Around calving events, horizontal flow speed increases in the short term, either coming back to baseline or seeing increases in longer-term speed compared to the

pre-calving event. Node 9 is an excellent example of tidal modulation increasing as it progresses closer to the calving front; however, once it is at/near the calving front, the quality of data reduces, and the tidal signal is reduced, indicating that other forces are at play not just a long-term tidal modulation. Nevertheless, what exactly is causing these changes is unknown.

Horizontal flow velocity is out of phase tide at the tide gauge. The glacier flows faster at low tide and slower at high tide. Figure 5:5 shows the horizontal flow for node 9, and in yellow, the chosen time frame (in black) that has been detrended and passed through U-Tide, resulting in clear M2 and K1 signal with an amplitude of 0.36 m/d (M2) and 0.18 m/d (K1). From DOY 193 to 203, there is a clear tidal signal, and horizontal flow follows the same path as the time with high and low tides correlating with the speed changes. This is also very clear in Node 3 (Figure 5:6) the primary tidal constituents are M2, S2, and K1 with amplitudes of 0.39, 0.16, and 0.15 m/d.

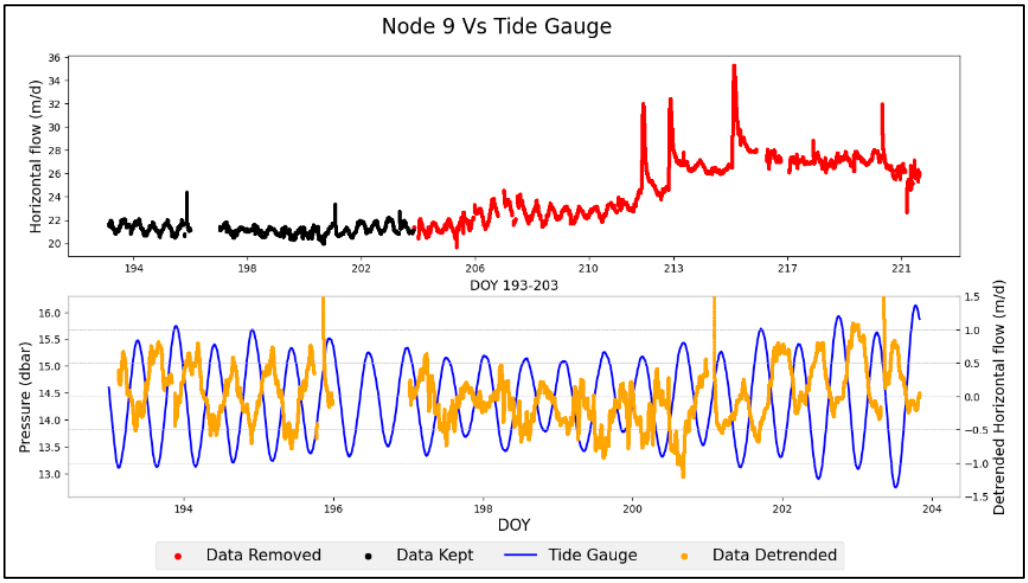

Figure 5:5, Horizontal flow from node 9 (red) and the chosen period from DOY 193 to 195 (black), this period is detrended and laid over the tide gauge with the recorded tide gage (blue). Note that the X axis is Day of the Year but not the same scale.

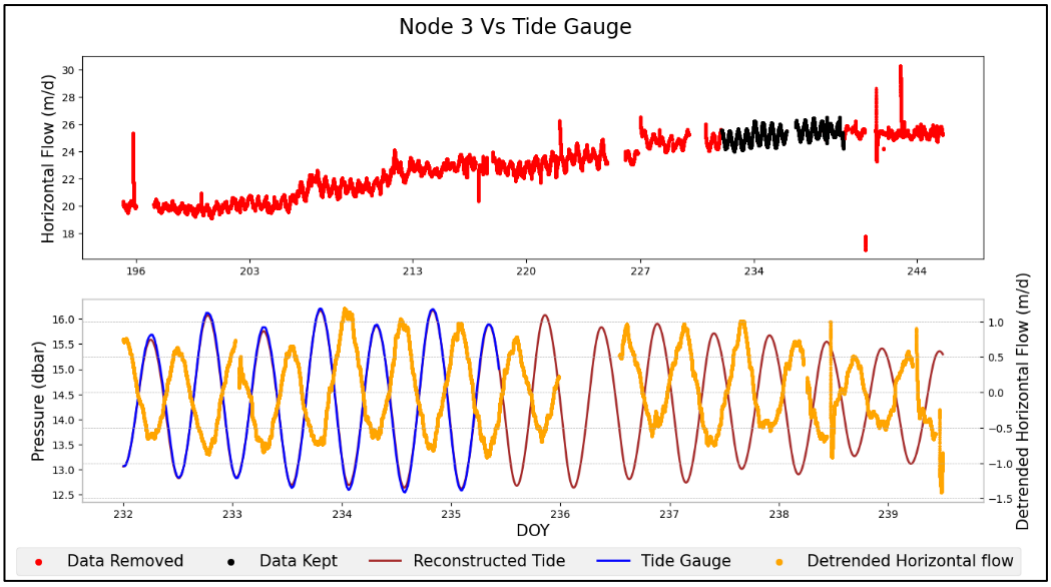

Figure 5:6, Horizontal flow from node 3 in black, is the detrended data with the last spike in flow removed (red) to ensure we look at the longer-term forcing. These seven days are detrended (orange) and laid over the tide gauge (blue). Then, when the tide gauge runs out, the reconstructed tide from U-Tide is used (brown). Note that the X axis is Day of the Year but not the same scale.

Many researchers have found similar results. Juan et al. (2010) stated that the along-flow motion of Helheim Glacier is advanced at low tide and slowed at high tide. They theorised that the cause of this is a result of the stress variations on the glacier terminus due to variations in hydrostatic pressure, as noted by Anandakrishnan & Alley (1997) on the Kamb Ice Stream (Ice Stream C). The premise is that during high tide, the water essentially buttresses Helheim Glacier, slowing the flow. This leads to an uplift at the front floating portion of the glacier. Then, as the tide falls, this pressure is released, allowing increased flow down the glacier as there is less force from the water holding the glacier back. Voytenko et al. (2015) looked at tidal forcing in Helheim Glacier in August of 2013, noting that the Helheim Glacier velocity moves out of phase with the semi-diurnal tides by ~8 hours while the ice mélange is in phase (based on vertical motion). These results are in line with the findings of this thesis.

At Store Glacier in Northwest Greenland, Walter et al. (2012) noted that ice flow fluctuations occurred at low tide but were linked with maximum daily air temperature. In our data comparing mean air temperature to the detrended horizontal flow, there is no evident modulation of flow based on temperature with peak flow velocity occurring at the maximum and minimum daily temperature at Helheim Glacier (Figure 5:7). However, further research into the K1 (diurnal flow peaks) and its interaction with air temperature should be undertaken to understand these processes fully. Davis et al. (2014) stated that Helheim Glacier experienced non-tidal variations at sites close to the terminus with peak-

to-peak variations in flow speed ~0.7 m/d and hypothesised this was due to the peaks in lubrication of the glacier bed from diurnal solar heating causing the surface melt. Bowdoin Glacier has also been recognised to have semi-diurnal speed peaks coinciding with low tide and subsequently attributed the role of hydrostatic pressure caving on the calving front (Sugiyama et al., 2015).

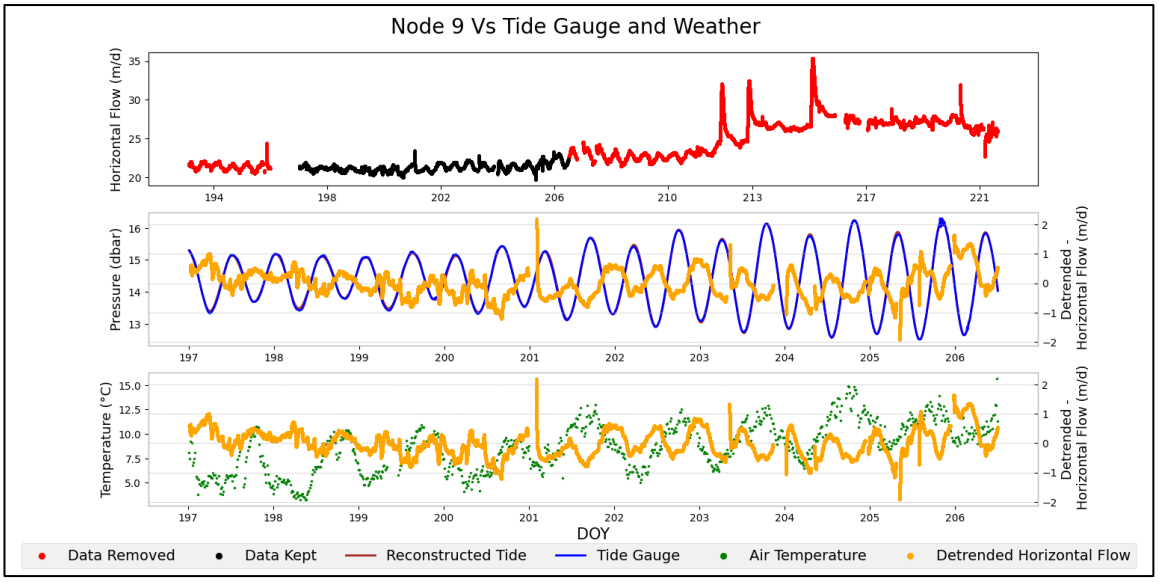

Figure 5:7, Horizontal flow of node 9, in black, is the chosen period to detrend, then in orange, the detrended result overlain by the tide (blue) or air temperature (green).

5.4 Calving Event-Induced Variations

Several calving events occurred during the 2013 summer. Reactions measured by the GPS sensors to these events are not linear across the whole glacier but regionally specific varying from the location of the calving event and the sensor distance from the calving front. Generally, the closer the GPS nodes are to the calving front the greater the flow increase after an event (Figure 5:8). Figure 5:9 shows substantial amounts of ice being lost between calving events on DOY 206 which also leads to the demise of node 11. Substantial amounts of ice loss likely reduced back stress, allowing increased flow. Benn et al. (2017) noted that ice loss leads to increased ice discharge because when ice is lost, there can be a reduction in resistance to ice flow from up the glacier.

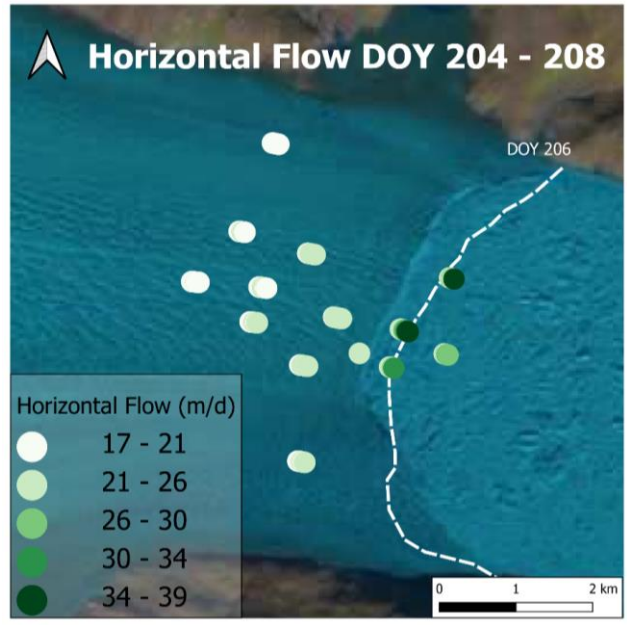

Figure 5:8, Horizontal flow velocity (m/d) of the nodes from DOY 203 – 208, showing the largest speeds occurring at/near the calving front during (green) and slower speeds further back (white). The Landsat 8 image is from 03/09/2023 (DOY 246).

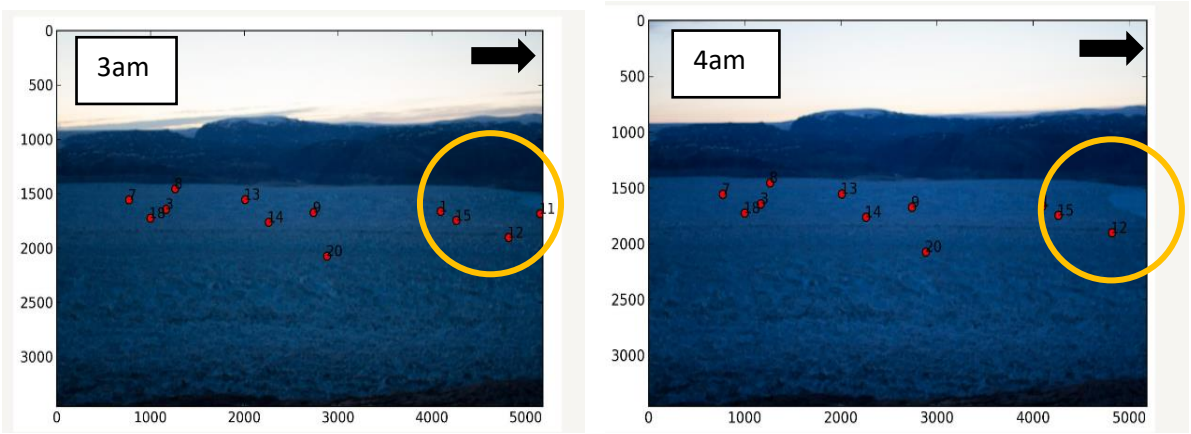

Figure 5:9, Photos of Helheim Glacier and the GPS node's positions from DOY 206, note the distortion between the closest node and the farthest node. The image at 3 am shows node 11 at the front. Then, at 4 am, node 11 is lost, and a substantial amount of ice is missing (circled), and the black arrows show the flow direction.

This speed-up in calving observed at Helheim Glacier has been observed previously. Juan (2011) states that in the 2007 and 2008 summers, calving events and the glacial earthquakes that come alongside correlated with sudden increases in glacier flow. The results also confirm the conclusions made by Nettles et al. (2008) that large tidewater glaciers like Helheim Glacier have a clear link between their flow speed and calving events. Juan (2011) notes that these speed changes can recover to pre-calving levels after the calving event, as demonstrated in my results. However, nodes at the calving front did not always track back to pre-calving flow but saw increased flow until the nodes were lost.

Helheim Glacier was semi-floating during 2013, with the circled portion in Figure 5:4, an estimation of where there is at least partially floating ice. However, if it is semi-floating, then there is an explanation for the tidally modulated changes in height and the occurrence of GEs. This differs from the period Juan (2011) looked at in 2006 because no GEs were found in 2006, but there was still an identifiable tidal signal to glacier height.

5.4.1 Calving and its impacts on long-term flow.

Sermilik Fjord partly controls the horizontal flow velocity of Helheim Glacier with a clear and pronounced semi-diurnal modulation from the M2 tidal signal. Calving events can disturb this through short-term increases in flow speed. The tidally-driven signals that cause dynamic changes in horizontal velocity or height changes can be overwhelmed by the signal from calving events that cause increases in horizontal flow. In most instances, the impact of calving is short-lived and the tidal signal returns after ~1 day. However, if the node is close to the calving front, the calving event can cause the loss of the node. The dynamic impacts of calving events do not propagate up the glacier that far, with nodes ~2 km away from the front experiencing no changes in flow, indicating that these short increases in flow only influence the glacier front potentially due to longitudinal stretching in these zones. There are nodes with no short-term changes to flow dynamics during or after calving events. These nodes continue to show tidal signals during the calving event, showing that the signal is still present despite being masked by the larger impacts of glacier calving on nodes close to the glacier front. In regions where the glacier is inferred to be grounded, tidal modulation of horizontal flow velocity still propagates up the glacier.

5.5 Fortnightly Cycle

The results presented in “4.3.3 Fortnightly Tidal Signal”, show an apparent M2 amplitude varying fortnightly and following a similar path to the spring neap cycle. A 4-day time series is too short for an analysis designed to separate multiple constituents with frequencies close to 1 or 2 c~~C~~ycles per day, which provide the most significant contribution to the tide in Sermilik Fjord. For a specific ocean location, the amplitude of a singular tidal constituent should not vary with time. The observed water level represents the sum of all the tidal constituents scaled by their amplitudes which remain constant. We cannot label the results as the M2 tidal constituent, but we can identify a semi-diurnal influence acting upon the glacier. This indicates that a 4-day analysis using a T-Tide or U-Tide approach is not appropriate when trying to separate the semi-diurnal amplitudes and it would not be

appropriate to draw inferences about the linearity of the glacier's response to the tides from individual tidal constituents.

5.6 Improvements

This research has used high-quality GPS data to measure the horizontal flow of Helheim Glacier, identifying the spring-neap cycle in the M2 tidal forcing and identifying portions of the glacier that are floating/semi-floating. Using KF to "clean" the data and remove outliers has been crucial in this research project and shows the benefits of its use and application across multiple GPS nodes in the same network. It allows replicability by putting each node through the same filter with the same parameters. At the same time, allowing the data quality to influence the smoothing level, identifying the best data set for each node possible while maintaining replicability across the board. The use of U-Tide has also been crucial in identifying the tidal signals seen in the GPS data whilst also being able to compare, contrast and predict the tide of Sermilik fjord compared to the tide gauge deployed by Straneo (Straneo, F., pers. comm., 2022).

However, like all research, there are caveats. Many parts of the research are not ideal/optimised. Firstly, considering this is a master's thesis, it was considered impractical to write a more complex KF due to time constraints. More in-depth filters that consider more variables, like using all three dimensions simultaneously can theoretically provide better position estimations. For example, the KF can consider different variables from epoch to epoch and alter the weighting of each position, e.g., if there are five satellites in one epoch, the likelihood that the position is more accurate than an epoch with only three satellites. However, it is easy to overcomplicate, and the purpose of using the KF was to filter the data better than in previous research where least squares were used (Juan, 2011; Juan et al., 2010; Murray, Selmes, et al., 2015). The KF can also potentially create a time delay between the observed and the predicted data because it requires multiple epochs of data to affect a change, meaning short-term sudden changes might be slightly out of time with the actual time frame. However, this is a worthwhile trade-off in the overall benefits of smoothing out "bad" data from errors in the GPS. Future research with GPS data should continue using KFs (King, 2004) and potentially integrating all three dimensions.

Secondly, the GPS network consisted of 20 nodes in a relatively small area compared to Juan (2011), which had a more comprehensive spatial distribution of GPS nodes across the length of the Helheim Glacier going far up the glacier over 3 years with 12-28 GPS nodes on

the glacier. In the future, another network like this should be deployed on other glaciers. A mixture of the two would be ideal, and the ability to compare how the M2 amplitude changes further up the glacier would be beneficial for modelling the flow of tidewater glaciers in different climate scenarios.

Thirdly, the longest time nodes left on Helheim Glacier was ~44 days over the summer. Placing the GPS nodes on the glacier earlier in the season, i.e., in May/June or even year-round through the winter would lead to more data being collected. If this is done alongside a wider distribution of nodes, one could track the movement of ice from the near beginning to the end of the glacier over a longer time.

Fourthly, the tide gauge is positioned relatively far away from Helheim Glacier. If there were also gauges closer to the glacier, you could identify if there is a phase lag between high tide at the gauge compared to the calving front of Helheim Glacier.

Fifthly, the GPS nodes are vulnerable to the uneven and changing surface of the Helheim Glacier (Figure 5:10). The nodes can fall over or dislodge due to crevasses opening and surface melt, causing undulations. They are not always in perfect view of the receiving stations or potentially the satellites, leading to inaccurate data. To combat the changing surface due to melt, the GPS nodes had custom-built ice crampons. However, they are still affected by undulations on the surface.

Figure 5:10, GPS node with the custom ice crampons deployed on Helheim Glacier. Also, note the glacier's highly crevassed and undulating nature.

Lastly, through this research and looking at the moving power graphs to identify the tidal signal, it has been identified that the time frames used through U-Tide are too short for it to handle and as a result in this study we are unable to comment on the linearity of the glacier

response to tidal flow. Future studies should use the data produced to perform more complex analyses, like tidal admittance analysis (O'Neel et al., 2003).

The limitations outlined should not negate the results found in this thesis and the deployment of the GPS network, as the GPS network is one of the first of its kind operating a large number of GPS nodes at the calving front. The geoPebble (Anandakrishnan et al., 2022) is an exciting development as the potential to use GPS data alongside seismic sensing could be a game changer. However, the geoPebble system is only single frequency compared to the dual frequency of this GPS network, limiting accuracy. This system has recently been deployed on Helheim Glacier; however, the data storage is local and collected using drones, resulting in data loss when the nodes are lost (Anandakrishnan et al., 2022), meaning you cannot see what happens during a calving event when the GPS receiver is lost.

5.7 Implications for the future of Helheim Glacier

Helheim Glacier is dynamic and ever-changing, with a vast array of variables that work with and against each other; being located inside Sermilik Fjord, Helheim Glacier has a clear visual semi-diurnal horizontal flow signal in line with the tides, and the floating portions of the glacier also show increases in height during high tide. Calving events cause step increases in flow in the short term whilst not affecting the whole glacier. SST is increasing (Fox-Kemper et al., 2021) alongside an increase in air temperature (Hanna et al., 2012; Mernild et al., 2014); this is likely to cause increased frontal ablation (D. I. Benn, Cowton, et al., 2017; Luckman et al., 2015). Increased calving will at least lead to an increase in horizontal flow in the short term. Increased basal melt could allow the tidal forces explained in this thesis to propagate further up the glacier, providing a positive feedback loop of increased ocean temperature leading to increased melting alongside the tide, forcing this water up the glacier bed with the potential for the spring tide to exert maximum influence. Ocean warming could also cause thinning, which may allow larger areas of floating ice, leading to increased flow speeds and a more accessible entry for water infiltrating the glacier bed. This could push Helheim Glacier into a more negative mass balance. Williams et al. (2021) state that Helheim Glacier is more vulnerable to oceanic and atmospheric warming due to its thinning and mass loss since 2005.

Chapter 6 – Conclusion

The goal of this thesis was to help contribute to a better understanding of tidewater glacier dynamics and the interactions between calving and ocean tides focusing on glacier flow. This research is important because understanding how tides interact with calving and flow is an important factor when producing calving models which rarely include a tidal component. Increased GPS usage and accessibility are important for gathering the best data possible as a glacier is not a single fixed block but has different flow regimes and paths of stretching and thinning in varying locations depending on the conditions.

To contribute to this goal, a KF has been written to process and filter GPS data, which was collected during a separate study in 2013 (Martin et al., 2014). This produced a high-quality and robust data set that allowed the identification of the tidal modulation on Helheim Glacier when analysed together with tidal gauge and other supplementary data sets (Temperature, Precipitation).

Despite facing adverse conditions, deploying GPS nodes on Helheim Glacier has resulted in usable data from 19 out of 20 nodes. This success highlights the potential of GPS technology to enhance our understanding of flow dynamics in large glaciers. Factors such as data gaps, the KF, and calving events have influenced data quality, but effective management and analysis have led to the extraction of valuable information.

The results presented shed light on various aspects of Helheim Glacier's behaviour. Long-term flow variations at the calving front align with previous research, showing median horizontal flow velocities of 16-24 m/d. However, these flow speeds are variable depending on the location of the GPS node on the glacier, with faster flow speeds recorded in the centre of the calving front whereas the edges of Helheim and further behind the calving front are much slower.

One of the key findings of this study is the semi-floating nature of the glacier front, the GPS data revealed tidal modulation in the variation of height (Figure 5:4). This indicates that this region is floating, however, due to the occurrence of glacial earthquakes, Helheim must be semi-floating. Because when a floating glacier calves the icebergs do not rotate. Further research opportunities should look at this occurrence in more detail to better understand what is happening at the glacier bed.

When the GPS nodes show tidal modulation of the variation in height, the modulation matches the ocean tide, rising and falling at the same time; this is the opposite of horizontal flow. With a ~2-hour time delay during high tide, the horizontal flow is slowest and after low tide, the flow speeds up. This indicates that high tide is causing pressure on the glacier, stemming glacier flow. Then, at low tide, this pressure is released, allowing increased flow.

This study provides results regarding horizontal flow velocity changes and height changes identifying a semidiurnal signal that is almost certainly resulting from tidal modulation. These semidiurnal signals are also linked with calving events and increase with proximity to the calving front. This indicates that whatever is causing this semidiurnal signal is crucial in regulating glacier motion and is almost definitely a result of ocean tides. However, a different approach is required to effectively quantify the signal and its true relationship with the ocean tide.

Calving events induce dynamic variations in horizontal flow velocity. These events can lead to short-term increases in flow speed, which is more pronounced closer to the calving front. Reducing back stress caused by calving events contributes to these flow changes, demonstrating the complex interplay between glacier dynamics and calving processes.

Despite the achievements of this research, there are opportunities for further improvement. Future studies could explore more sophisticated use of the KF and deploy a more extensive GPS network across multiple glaciers. Additionally, placing GPS nodes earlier in the season, integrating more tide gauges, and addressing the challenges posed by changing glacier surfaces could enhance data quality and coverage.

In conclusion, this study has significantly contributed to our understanding of Helheim Glacier's behaviour, highlighting the role of tides and calving events in shaping flow dynamics. The combination of GPS technology and data analysis techniques has deepened our insights into glacier processes. As glaciers respond to changing environmental conditions, ongoing research in this field remains crucial for advancing our knowledge of ice flow and its implications for sea level rise. Future research should focus on understanding when and where tidewater glaciers are floating or grounded and then identify the causes of these differences.

Chapter 7 – Appendix

7.1 Methodology

7.1.1 Kalman Filter in Detail

Table 7:1, Abbreviations used for the Kalman filter in the step-by-step breakdown.

Name	*Symbol*
Transition Matrix	*M*
Transposed Transition Matrix	*MT*
Predicted State	*PS*
Process Noise VCM (Variance Covariance Matrix)	*Pn*
Predicted State VCM	*Cx_i*
Innovation	*Vi*
Observed VCM	*CI*
Design Matrix	*A*
Kalman Gain	*G*
Corrected state	*CS*
Corrected state VCM	*Cx_I*

Below is a walk-through of how the Kalman filter works. The calculations shown are Just for Height, but Easting and Northing are also calculated in the whole filter.

1. Convert data to 1-second data.
    a. If data is missing, the position value is recorded as "Not a Number" (NaN)
2. Set Processing Variables
    a. Sigma height (50m) – when there is data.
        i. When there is a NaN value – Sigma observation = 999999
    b. Process noise position (5e-20)
    c. Process noise velocity (5e-20)
3. Set the Transition Matrix (M)
    a. $\begin{bmatrix} 1 & 1 \\ 0 & 1 \end{bmatrix}$
4. Set Design Matrix
    a. $\begin{bmatrix} 1 & 0 \end{bmatrix}$

5. Previous Corrected state of the observation
    a. For the First Epoch, the previous Corrected state is manually set to:
        i. Height - $[150 \quad 0]$
        ii. Easting - $[53600 \quad 0.00025]$
        iii. Northing - $[7361000 \quad -0.00005]$
    b. On every other Epoch, the Precious corrected state is the Corrected state of the previous Epoch.
6. Calculate the Predicted State observation.
    a. Transition Matrix * Previous Corrected state observation.
    b. $\begin{bmatrix} 1 & 1 \\ 0 & 1 \end{bmatrix} * [150 \quad 0] = [150 \; 0]$
7. Get the Previous Corrected state VCM (Cx_I^{-1})
    a. Once the KF is running, this is just taking the Corrected state VCM from the previous Epoch.
    b. When initiating the KF, the Corrected state is set to:
        i. $\begin{bmatrix} 1000000000 & 0 \\ 0 & 0.001 \end{bmatrix}$
8. Process noise VCM is constant.
    a. [[Process Noise Position 0], [0 Process Noise Velocity]]
    b. $\begin{bmatrix} 5e-20 & 0 \\ 0 & 5e-20 \end{bmatrix}$
9. Calculate the Transitioned old VCM (M*Cx_i-1*MT)
    a. Transition Matrix * Previous Corrected stateVCM * Transposed Transition Matrix
    b. Transposed $M^t = \begin{bmatrix} 1 & 0 \\ 1 & 1 \end{bmatrix}$
        i. $\begin{bmatrix} 1 & 1 \\ 0 & 1 \end{bmatrix} * \begin{bmatrix} 1000000000 & 0 \\ 0 & 0.001 \end{bmatrix} * \begin{bmatrix} 1 & 0 \\ 1 & 1 \end{bmatrix} * =$
        $\begin{bmatrix} 1000000000.001 & 0.0001 \\ 0.0001 & 0.0001 \end{bmatrix}$
10. Calculate Predicted state VCM (CX_I)
    a. Transitioned old VCM + Process Noise VCM
    b. $\begin{bmatrix} 1000000000.001 & 0.0001 \\ 0.0001 & 0.0001 \end{bmatrix} + \begin{bmatrix} 5e-20 & 0 \\ 0 & 5e-20 \end{bmatrix} =$
    $\begin{bmatrix} 1000000000.001 & 0.0001 \\ 0.0001 & 0.0001 \end{bmatrix}$
        i. The value is too small to show.
11. Calculate Innovation (Vi)
    a. Measured Value – Predicted state.

b. $152.201 - 150 = 2.201$

12. Calculate the Observed VCM (CI)
    a. Current Sigma Height^2
    b. When there is data = 2500
    c. No data = 9.99998e+11
13. Calculate P1
    a. Predicted state VCM * transposed Design matrix.
    b. $\begin{bmatrix} 1000000000.001 & 0.0001 \\ 0.0001 & 0.0001 \end{bmatrix} * \begin{bmatrix} 1 \\ 0 \end{bmatrix} = \begin{bmatrix} 1000000000.001 \\ 0.001 \end{bmatrix}$
14. Calculate P2
    a. Design Matrix * P1
    b. $[1\ 0] * \begin{bmatrix} 1000000000.001 \\ 0.001 \end{bmatrix} = 1000000000.001$
15. Calculate P3
    a. P2 + Sigma height^2.
    b. $1000000000.001 + 2500 = 1000002500.0010000$
16. Calculate Kalman Gain (G)
    a. P1 * (Inverse matrix of P3)
    b. $\begin{bmatrix} 1000000000.001 \\ 0.001 \end{bmatrix} *$ 9.99998e-10 (inverse matrix of 1000000000.001)
    $= \begin{bmatrix} 0.9999975 \\ 1e-12 \end{bmatrix}$
17. Kalman Gain * Innovation
    a. G * Vi
    b. $\begin{bmatrix} 0.9999975 \\ 1e-12 \end{bmatrix} * 2.201 = \begin{bmatrix} 2.20099450 \\ 2.2e-12 \end{bmatrix}$
18. Calculate Correct State –
    a. (G * Vi) + Predicted.
    b. $\begin{bmatrix} 2.20099450 \\ 2.2e-12 \end{bmatrix} + [150 \quad 0] = \begin{bmatrix} 152.20099450 \\ 2.2e-12 \end{bmatrix}$
    c. 152.20099450 is the corrected height position.
    d. $2.2e-12$ is the corrected height velocity.

19. G*A*Cx_i
    a. Kalman Gain * Design Matrix * Predicted State VCM
    b. $\begin{bmatrix} 0.9999975 \\ 1e-12 \end{bmatrix} * \left([1 \quad 0] * \begin{bmatrix} 1000000000.001 & 0.0001 \\ 0.0001 & 0.0001 \end{bmatrix} \right) =$
    $\begin{bmatrix} 999997500.0072500 & 0.0010000 \\ 0.0010000 & 1e-15 \end{bmatrix}$

20. Corrected State VCM
    a. Predicted state VCM - (G*A*Cx_i)

$$\begin{bmatrix} 1000000000.001 & 0.0001 \\ 0.0001 & 0.0001 \end{bmatrix} - \begin{bmatrix} 999997500.0072500 & 0.0010000 \\ 0.0010000 & 1e-15 \end{bmatrix}$$

$$= \begin{bmatrix} 2499.993749857 & 2.49999E-09 \\ 2.49999E-09 & 0.00100000 \end{bmatrix}$$

7.1.2 External Data Links and Programs

- GitHub – https://github.com/Jcolinese
- Python U-Tide – https://github.com/wesleybowman/U-Tide
- Danish Metrological Institute – https://www.dmi.dk/publikationer/
- Python – https://www.python.org/
- QGIS – https://www.qgis.org/en/site/

7.1.3 Calving Data

Table 7:2, Table of the Calving events recorded Earthquakes 1 is from the Original dataset, then Earthquakes 2 is from the second pass through the seismic array, and then the two data sets are combined.

Type	Date	Time	Day of Year
Photos	24-Jul	19:37	205
	24-Jul	19:38	205
	25-Jul	03:13	206
	25-Jul	11:30	206
	25-Jul	12:56	206
	25-Jul	13:30	206
	25-Jul	15:30	206
	26-Jul	01:43	207
	28-Jul	22:30	209
	30-Jul	20:01	211
	31-Jul	19:21	212
	03-Aug	00:30	215
	07-Aug	08:30	219
	08-Aug	06:49	220
	14-Aug	23:41	226
	14-Aug	23:50	226
	16-Aug	01:30	228
	20-Aug	00:30	232
Earthquakes 1	23-Jun	14:35	174
	25-Jul	03:13	206
	25-Jul	12:56	206
	08-Aug	06:49	220
	14-Aug	23:41	226
	14-Aug	23:50	226
Earthquakes 2	24-Jul	11:01	205
	24-Jul	19:37	205
	24-Jul	19:38	205
	26-Jul	01:43	207
	30-Jul	20:01	211
	31-Jul	19:21	212
	31-Jul	20:28	212

7.2 Results

Table 7:3, U-Tide results of the tide gauge for just the 2013 summer study period (July – August). The amplitude is in d-bar.

2013 Summer (2013-07-01 to 2013-08-23)						
Constituents	Frequency cpd	Amplitude	Signal to Noise Ratio	Percent Energy	Phase ◦	Amplitude
M2	1.9322736	1.0452386	59157.1561832	81.1708872	200.371465	1.045239
S2	2.0000000	0.4005207	9932.2971692	11.9184346	250.031944	0.400521
N2	1.8959820	0.2263047	3879.9534333	3.8050160	171.415193	0.226305
K1	1.0027379	0.1764431	7213.0644564	2.3130159	163.047301	0.176443
O1	0.9295357	0.0712295	1180.8777553	0.3769551	114.198332	0.07123
MU2	1.8645472	0.0486292	155.5904733	0.1756965	175.980247	0.048629
L2	1.9685653	0.0294939	59.3962098	0.0646298	213.763903	0.029494
MSF	0.0677264	0.0274735	53.8481249	0.0560785	311.605662	0.027473
MM	0.0362916	0.0227990	36.3405060	0.0386188	241.759006	0.022799
2MS6	5.8645472	0.0145020	231.3121678	0.0156252	246.754353	0.014502
ETA2	2.0417675	0.0131237	13.3888650	0.0127962	170.252323	0.013124
M4	3.8645472	0.0112056	2235.4974511	0.0093290	234.127014	0.011206
M6	5.7968208	0.0109667	180.0826456	0.0089356	167.334874	0.010967
M3	2.8984104	0.0095513	434.9868675	0.0067779	272.31206	0.009551
Q1	0.8932441	0.0087645	26.1380205	0.0057072	51.649304	0.008764
MS4	3.9322736	0.0083489	1166.7689973	0.0051788	312.331717	0.008349
NO1	0.9664463	0.0067187	13.3837938	0.0033538	144.912323	0.006719
J1	1.0390296	0.0055635	6.7306412	0.0022996	221.168334	0.005563
EPS2	1.8282556	0.0050008	1.8175231	0.0018580	135.086664	0.005001
2MN6	5.7605292	0.0046311	25.9941694	0.0015935	114.652937	0.004631
UPS1	1.1122318	0.0044097	6.3818280	0.0014447	332.357911	0.00441
MN4	3.8282556	0.0041231	241.6971020	0.0012631	181.187708	0.004123
ALP1	0.8255177	0.0034231	3.5983564	0.0008706	237.003147	0.003423
SK3	3.0027379	0.0033982	56.4286453	0.0008580	26.792651	0.003398
2SM6	5.9322736	0.0029993	12.3339672	0.0006684	349.769455	0.002999
2Q1	0.8569524	0.0028846	2.4683927	0.0006182	284.985524	0.002885
OO1	1.0759401	0.0028085	2.7209341	0.0005860	204.175286	0.002809
MK3	2.9350115	0.0018635	20.1151196	0.0002580	44.781129	0.001863
SN4	3.8959820	0.0016027	56.5537811	0.0001908	312.525857	0.001603
3MK7	6.7995588	0.0015118	7.4278488	0.0001698	212.702923	0.001512
MO3	2.8618093	0.0013130	9.3872733	0.0001281	87.903047	0.001313
M8	7.7290945	0.0009094	4.7119905	0.0000614	207.765896	0.000909
S4	4.0000000	0.0008325	10.7606872	0.0000515	77.2347	0.000833
2MK5	4.8672851	0.0006994	11.2192042	0.0000363	66.991693	0.000699
2SK5	5.0027379	0.0003237	3.1288843	0.0000078	9.80806	0.000324

Table 7:4, UTide Results of the Tide gauge for the whole available record (2011-2013). The amplitude is in d-bar.

Whole Record (2011-08-20 to 2013-08-23)						
Constituents	Frequency cpd	Amplitude	Signal to Noise Ratio	Percent Energy	Phase ◦	Amplitude
M2	1.9322736	1.0443191	10266829.1096773	79.8046825	200.42	1.044319
S2	2.0000000	0.4163305	1444002.0685594	12.6834787	238.86	0.41633
N2	1.8959820	0.2001524	301175.3479478	2.9314574	178.22	0.200152
K1	1.0027379	0.1540485	123862.0449169	1.7365081	148.98	0.154048
K2	2.0054758	0.1163696	95176.3690621	0.9909252	236.55	0.11637
SA	0.0027378	0.0995426	407.8058759	0.7250697	318.63	0.099543
O1	0.9295357	0.0730425	30249.8146957	0.3904036	113.71	0.073043
P1	0.9972621	0.0488543	13280.3882136	0.1746493	143.74	0.048854
NU2	1.9008389	0.0378840	12064.2693820	0.1050202	182.96	0.037884
MU2	1.8645472	0.0323131	8481.4147111	0.0764044	150.86	0.032313
2N2	1.8596903	0.0310368	7629.0991816	0.0704879	154.45	0.031037
SSA	0.0054758	0.0276111	34.9973286	0.0557865	101.19	0.027611
L2	1.9685653	0.0249948	6013.2274571	0.0457153	224.15	0.024995
T2	1.9972622	0.0217382	4232.7304868	0.0345787	233.83	0.021738
MF	0.0732022	0.0209520	28.6929212	0.0321227	214.15	0.020952
MM	0.0362916	0.0204329	32.4002857	0.0305508	210.48	0.020433
MSM	0.0314347	0.0175277	18.5361846	0.0224807	146.32	0.017528
2MS6	5.8645472	0.0129250	2789.2915284	0.0122243	234.66	0.012925
M4	3.8645472	0.0117009	15393.6592177	0.0100185	231.43	0.011701
NO1	0.9664463	0.0106870	552.7603048	0.0083574	129.70	0.010687
M3	2.8984104	0.0095264	5023.8807438	0.0066409	277.36	0.009526
M6	5.7968208	0.0091233	1835.5206417	0.0060906	166.05	0.009123
EPS2	1.8282556	0.0085073	815.8775578	0.0052959	123.99	0.008507
MS4	3.9322736	0.0082779	7816.5136645	0.0050142	302.07	0.008278
ETA2	2.0417675	0.0077008	571.3792492	0.0043395	261.80	0.007701
S1	1.0000001	0.0073694	298.9012849	0.0039740	254.78	0.007369
LDA2	1.9637084	0.0071119	417.0183067	0.0037011	205.87	0.007112
J1	1.0390296	0.0065106	195.6584170	0.0031017	149.15	0.006511
MSF	0.0677264	0.0049660	1.7307440	0.0018046	252.72	0.004966
H1	1.9295358	0.0048590	170.4406562	0.0017277	192.70	0.004859
OO1	1.0759401	0.0046275	90.9483282	0.0015669	146.57	0.004627
Q1	0.8932441	0.0044832	139.7530892	0.0014708	57.15	0.004483
H2	1.9350114	0.0044249	184.5410515	0.0014328	265.53	0.004425
GAM2	1.9274167	0.0042215	135.8022760	0.0013041	208.21	0.004222
MN4	3.8282556	0.0039298	1678.5359379	0.0011301	197.47	0.00393
OQ2	1.8233987	0.0037803	182.6838644	0.0010457	117.79	0.00378
2MN6	5.7605292	0.0036532	238.7010551	0.0009766	138.30	0.003653
PHI1	1.0082137	0.0036442	61.5326481	0.0009718	139.27	0.003644
2MK6	5.8700231	0.0033234	229.0251980	0.0008082	233.67	0.003323
PI1	0.9945243	0.0032135	45.7588467	0.0007556	156.77	0.003213
MKS2	1.9377494	0.0029841	83.6227885	0.0006516	220.62	0.002984
2Q1	0.8569524	0.0029564	43.2189691	0.0006396	272.50	0.002956
R2	2.0027378	0.0028711	63.9982636	0.0006032	240.66	0.002871
MK4	3.9377494	0.0025763	802.5513675	0.0004857	305.36	0.002576
RHO1	0.8981010	0.0025285	30.8829071	0.0004678	86.95	0.002529
MO3	2.8618093	0.0024151	278.0249710	0.0004268	144.45	0.002415
CHI1	0.9713032	0.0021896	20.3215683	0.0003508	170.34	0.00219
2SM6	5.9322736	0.0018752	62.4320567	0.0002573	308.16	0.001875
TAU1	0.9350115	0.0018130	14.5692958	0.0002405	100.75	0.001813
MSK6	5.9377494	0.0017825	73.0546866	0.0002325	302.88	0.001782
SK3	3.0027379	0.0017612	151.1320393	0.0002270	338.68	0.001761
PSI1	1.0054757	0.0017236	14.9986347	0.0002174	53.16	0.001724
SO1	1.0704643	0.0016505	13.0755174	0.0001993	107.64	0.00165
MK3	2.9350115	0.0016160	122.8349606	0.0001911	104.41	0.001616
MSN2	2.0362916	0.0015426	30.8938356	0.0001741	80.38	0.001543
SN4	3.8959820	0.0012240	154.7557224	0.0001096	288.01	0.001224
SO3	2.9295357	0.0010929	66.7401553	0.0000874	273.42	0.001093
SIG1	0.8618093	0.0010747	6.0990798	0.0000845	351.03	0.001075
UPS1	1.1122318	0.0009070	7.7651695	0.0000602	101.98	0.000907
BET1	0.9609704	0.0009009	4.5677062	0.0000594	249.89	0.000901
M8	7.7290945	0.0006435	32.0821967	0.0000303	199.70	0.000643
SK4	4.0054758	0.0006385	39.7183397	0.0000298	283.96	0.000639
3MK7	6.7995588	0.0006253	21.8789466	0.0000286	190.27	0.000625
S4	4.0000000	0.0005604	31.6882480	0.0000230	85.22	0.00056
2MK5	4.8672851	0.0005490	81.6729860	0.0000221	60.73	0.000549
THE1	1.0341726	0.0004877	1.8625192	0.0000174	158.45	0.000488
ALP1	0.8255177	0.0002422	0.5650507	0.0000043	91.51	0.000242
2SK5	5.0027379	0.0002378	15.0751105	0.0000041	98.90	0.000238

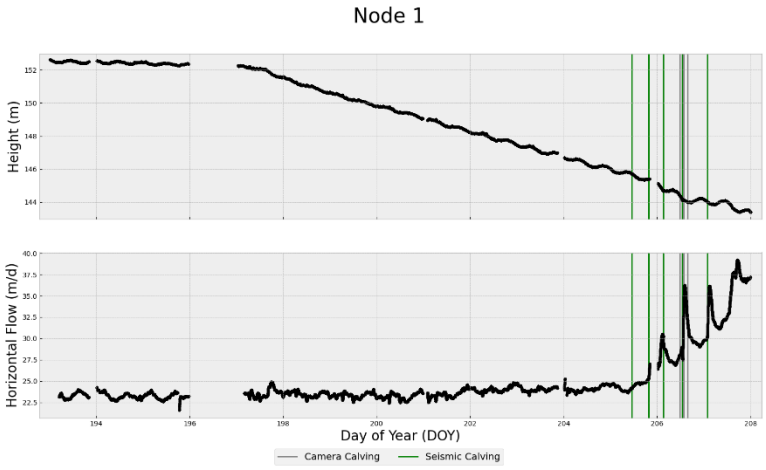

Figure 7:1, Node 1 Height (Top) and Horizontal Flow (Bottom). Alongside the Camera and Seismic Calving.

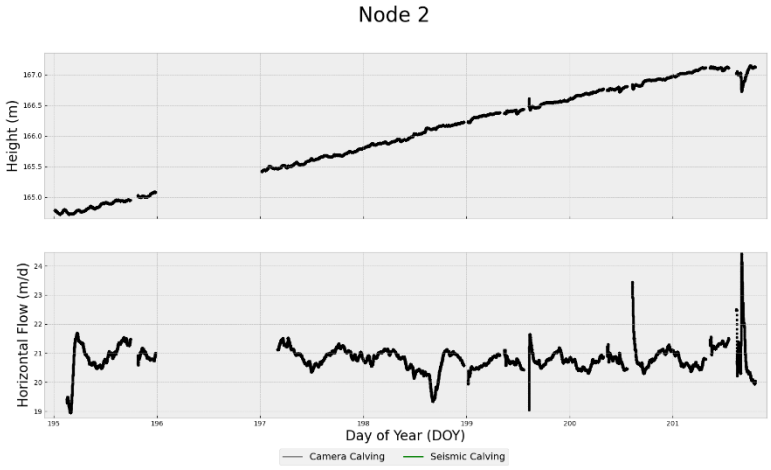

Figure 7:2, Node 2 Height (Top) and Horizontal Flow (Bottom). Alongside the Camera and Seismic Calving.

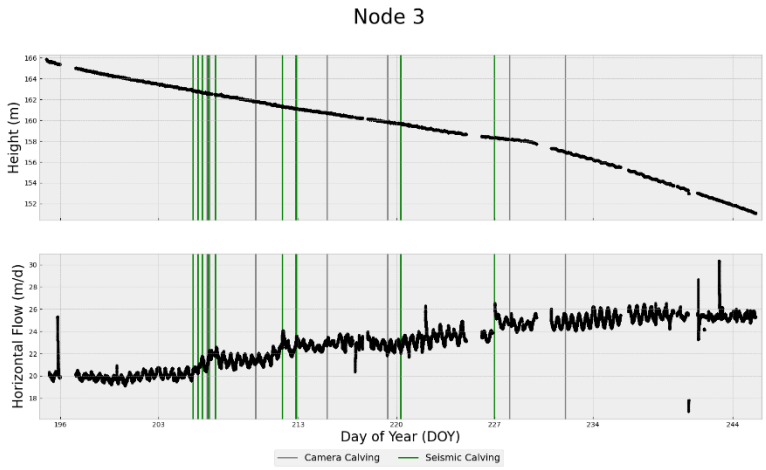

Figure 7:3, Node 3 Height (Top) and Horizontal Flow (Bottom). Alongside the Camera and Seismic Calving.

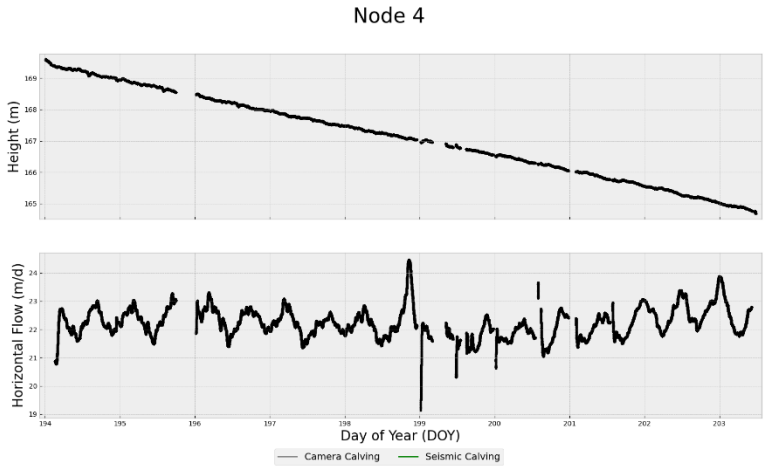

Figure 7:4, Node 4 Height (Top) and Horizontal Flow (Bottom). Alongside the Camera and Seismic Calving.

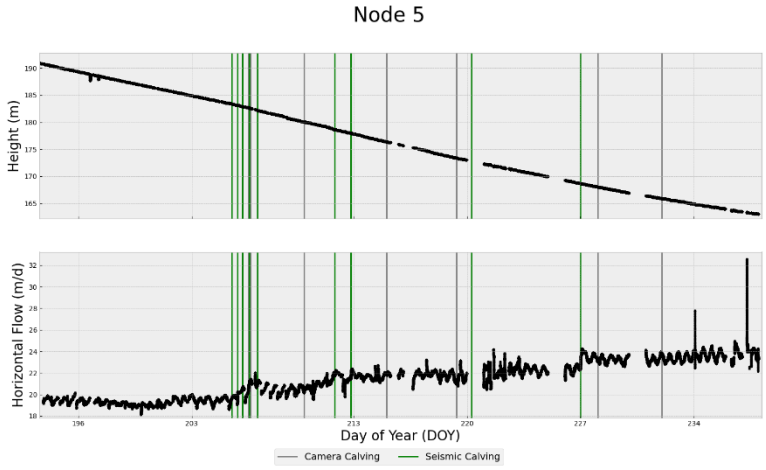

Figure 7:5, Node 5 Height (Top) and Horizontal Flow (Bottom). Alongside the Camera and Seismic Calving.

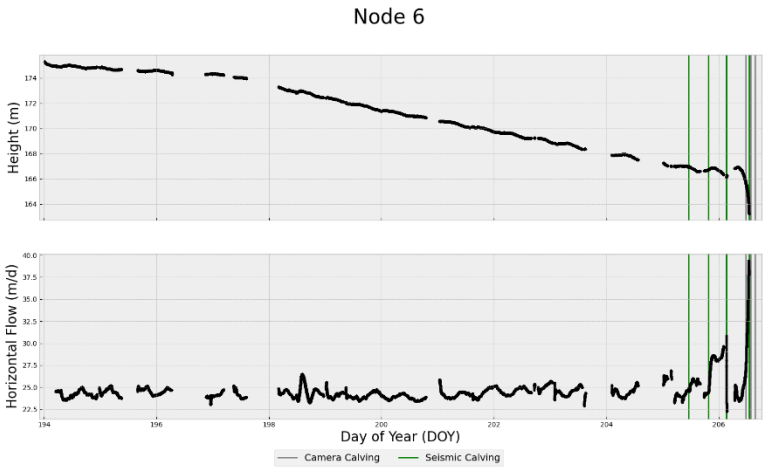

Figure 7:6, Node 6 Height (Top) and Horizontal Flow (Bottom). Alongside the Camera and Seismic Calving.

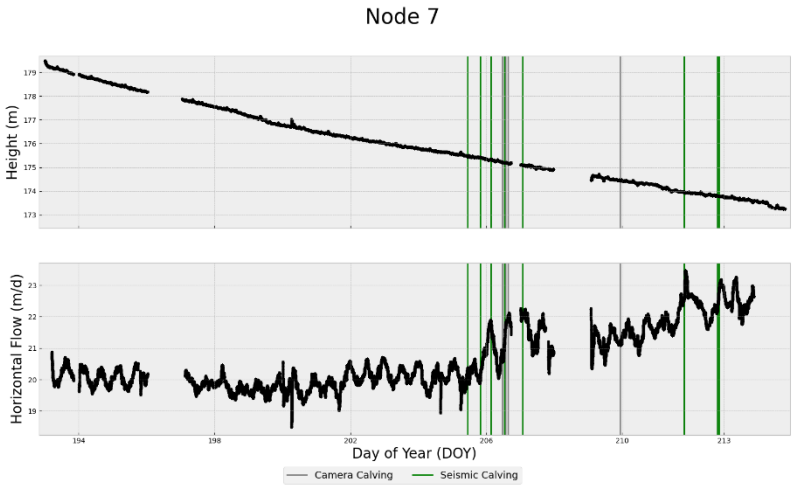

Figure 7:7, Node 7 Height (Top) and Horizontal Flow (Bottom). Alongside the Camera and Seismic Calving.

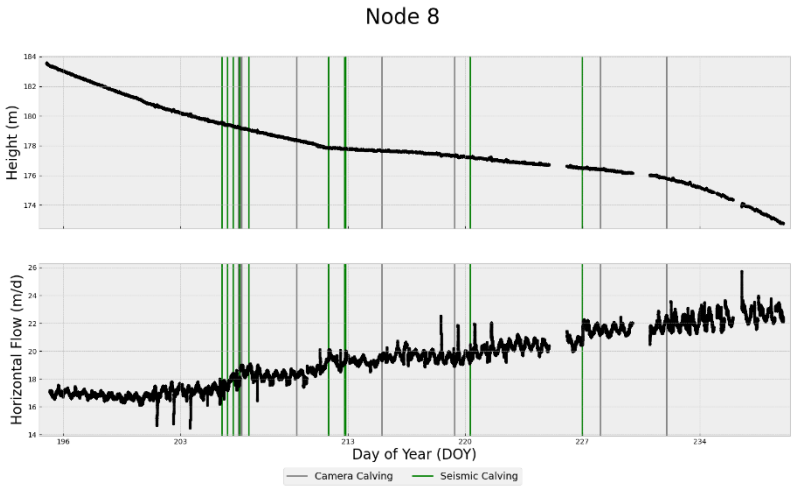

Figure 7:8, Node 8 Height (Top) and Horizontal Flow (Bottom). Alongside the Camera and Seismic Calving.

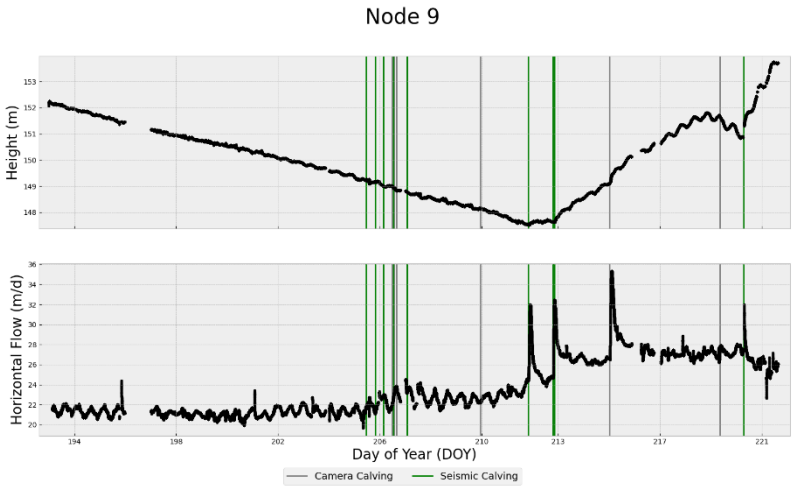

Figure 7:9, Node 9 Height (Top) and Horizontal Flow (Bottom). Alongside the Camera and Seismic Calving.

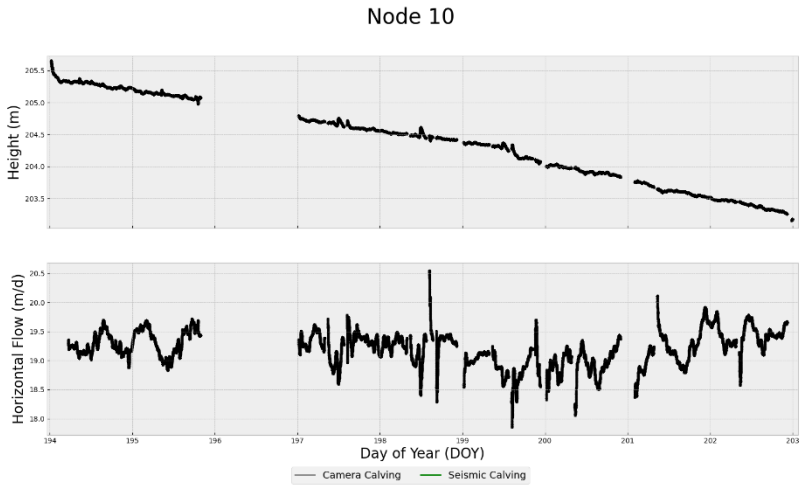

Figure 7:10, Node 10 Height (Top) and Horizontal Flow (Bottom). Alongside the Camera and Seismic Calving.

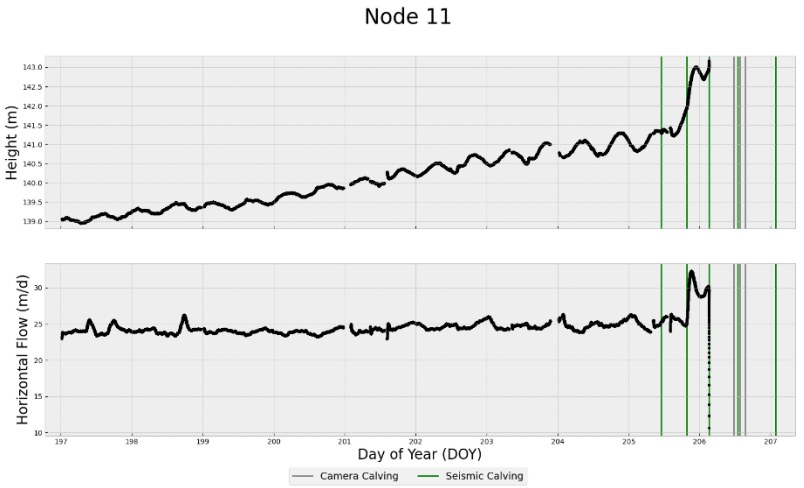

Figure 7:11, Node 11 Height (Top) and Horizontal Flow (Bottom). Alongside the Camera and Seismic Calving.

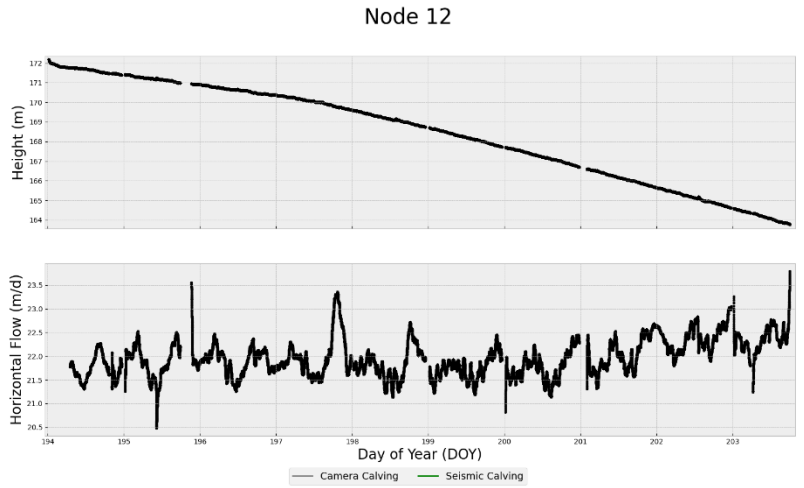

Figure 7:12, Node 12 Height (Top) and Horizontal Flow (Bottom). Alongside the Camera and Seismic Calving.

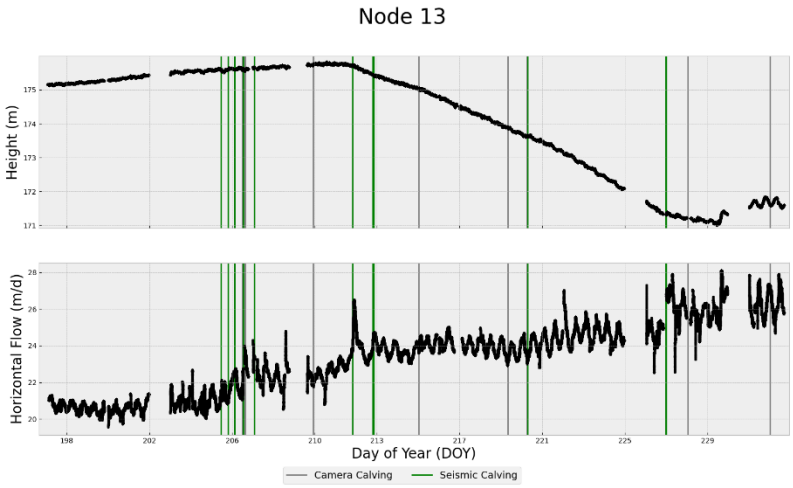

Figure 7:13, Node 13 Height (Top) and Horizontal Flow (Bottom). Alongside the Camera and Seismic Calving.

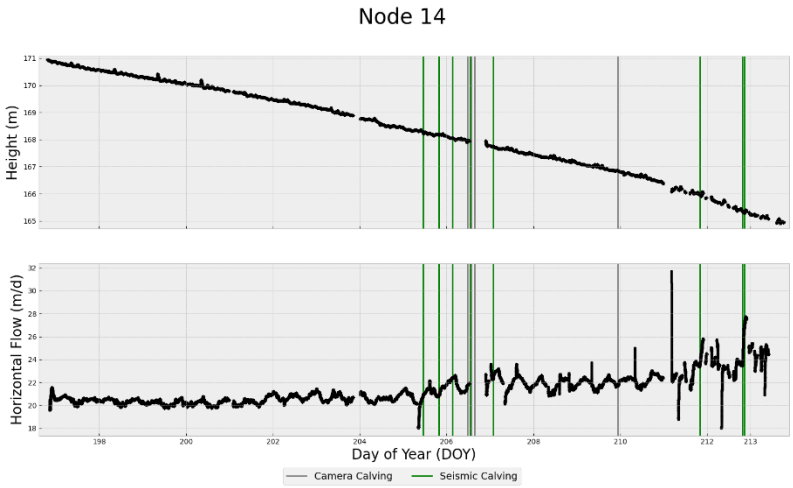

Figure 7:14, Node 14 Height (Top) and Horizontal Flow (Bottom). Alongside the Camera and Seismic Calving.

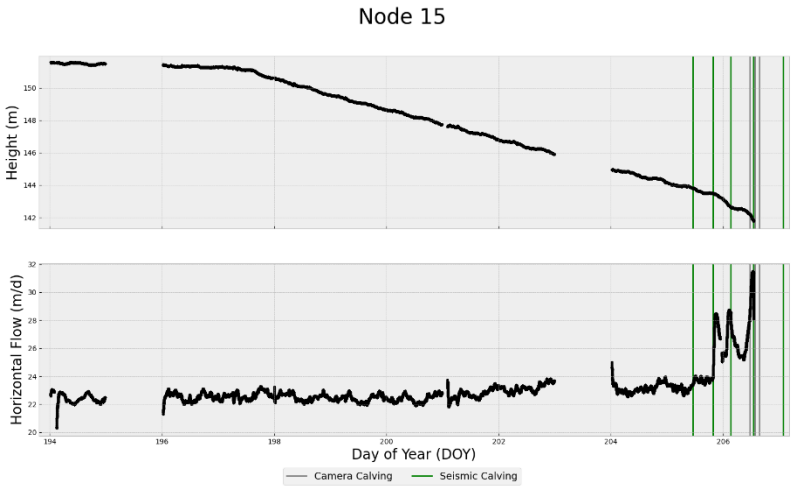

Figure 7:15, Node 15 Height (Top) and Horizontal Flow (Bottom). Alongside the Camera and Seismic Calving.

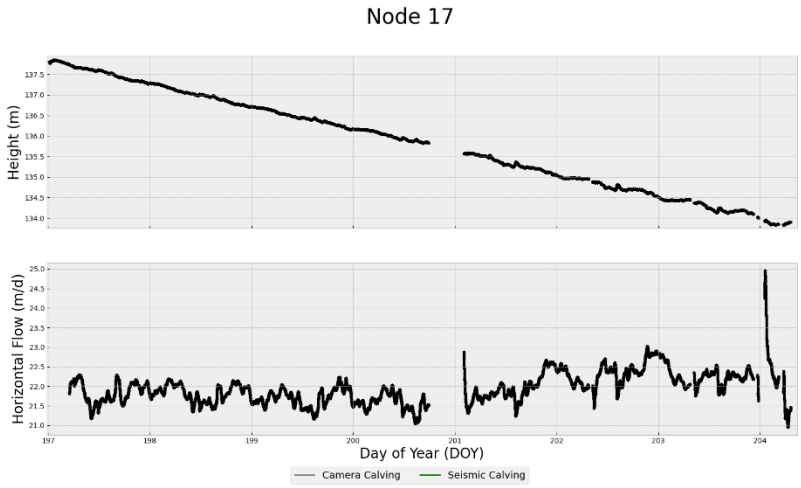

Figure 7:16, Node 17 Height (Top) and Horizontal Flow (Bottom). Alongside the Camera and Seismic Calving.

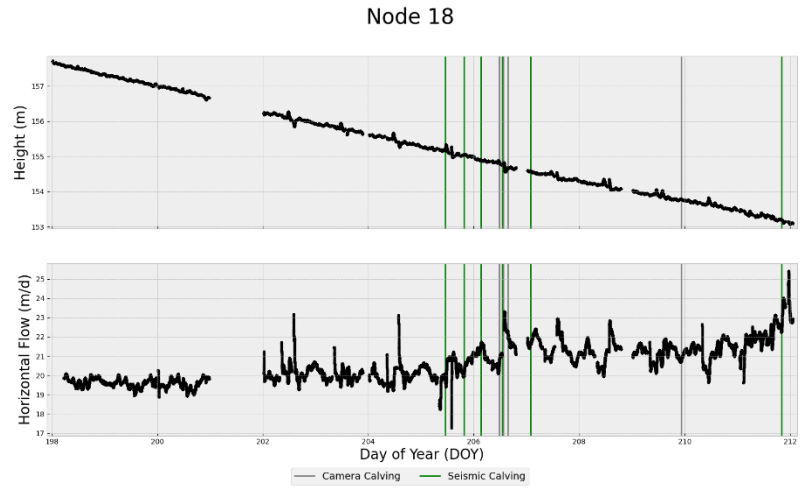

Figure 7:17, Node 18 Height (Top) and Horizontal Flow (Bottom). Alongside the Camera and Seismic Calving.

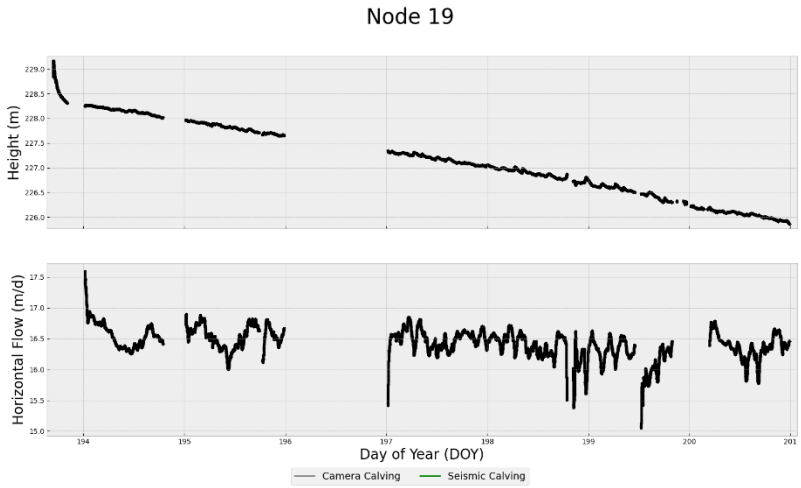

Figure 7:18, Node 19 Height (Top) and Horizontal Flow (Bottom). Alongside the Camera and Seismic Calving.

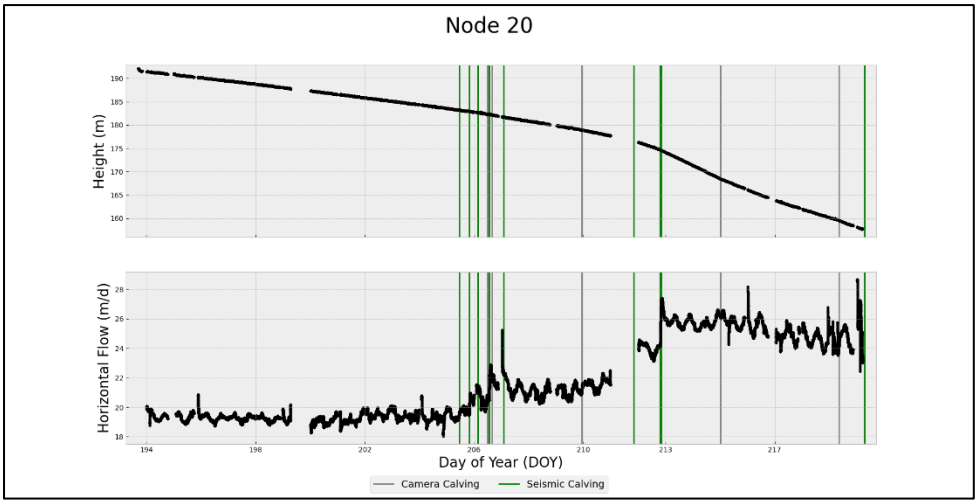

Figure 7:19, Node 20 Height (Top) and Horizontal Flow (Bottom). Alongside the Camera and Seismic Calving.

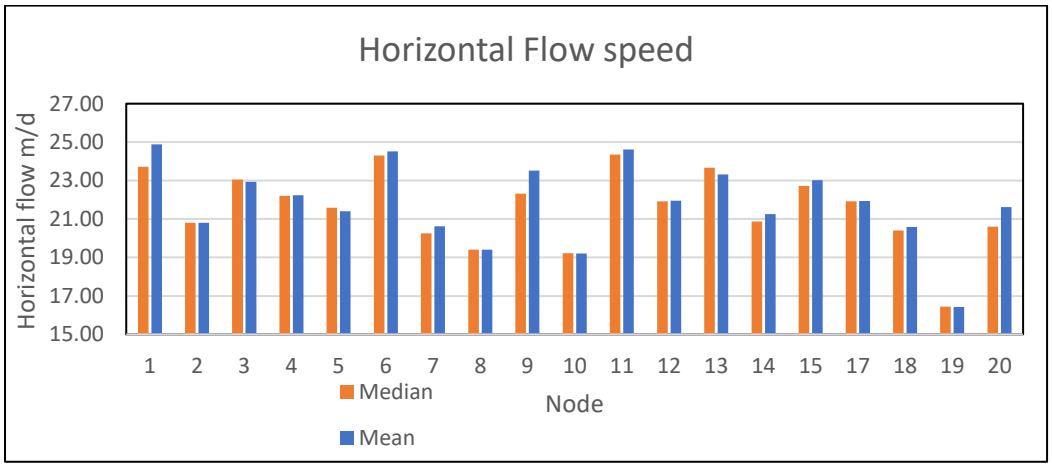

Figure 7:20, Bar chart showing the Median and Mean horizontal Flow for each GPS node.

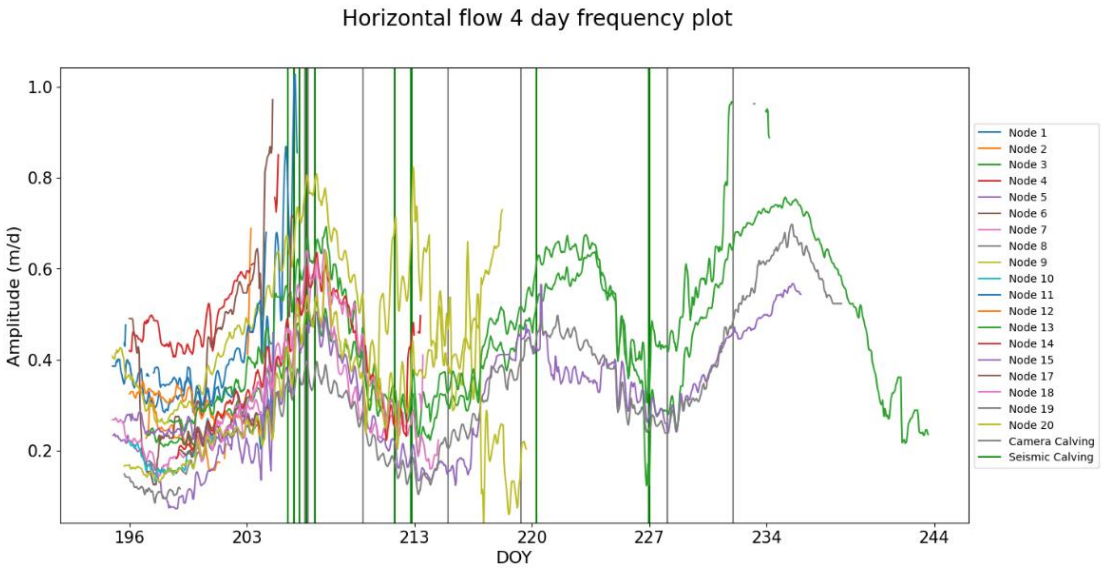

Figure 7:21, Horizontal Flow M2 amplitude for all nodes showing the fortnightly tidal signal change.

Table 7:5, GPS Nodes flow direction as a percentage. Most nodes are constantly flowing southeast. However, some nodes for small periods flow North-East.

Node Flow Direction								
Node	North	North-East	East	South-East	South	South-West	West	North-West
1	0.00	0.00	0.00	**100.00**	0.00	0.00	0.00	0.00
2	0.00	0.00	0.00	**100.00**	0.00	0.00	0.00	0.00
3	0.00	**0.03**	0.00	**99.97**	0.00	0.00	0.00	0.00
4	0.00	0.00	0.00	**100.00**	0.00	0.00	0.00	0.00
5	0.00	**0.15**	0.00	**99.85**	0.00	0.00	0.00	0.00
6	0.00	**0.02**	0.00	**99.98**	0.00	0.00	0.00	0.00
7	0.00	**0.04**	0.00	**99.96**	0.00	0.00	0.00	0.00
8	0.00	**0.02**	0.00	**99.98**	0.00	0.00	0.00	0.00
9	0.00	0.00	0.00	**100.00**	0.00	0.00	0.00	0.00
10	0.00	**0.33**	0.00	**99.67**	0.00	0.00	0.00	0.00
11	0.00	0.00	0.00	**100.00**	0.00	0.00	0.00	0.00
12	0.00	0.00	0.00	**100.00**	0.00	0.00	0.00	0.00
13	0.00	0.00	0.00	**100.00**	0.00	0.00	0.00	0.00
14	0.00	0.00	0.00	**100.00**	0.00	0.00	0.00	0.00
15	0.00	**0.02**	0.00	**99.98**	0.00	0.00	0.00	0.00
17	0.00	0.00	0.00	**100.00**	0.00	0.00	0.00	0.00
18	0.00	0.00	0.00	**100.00**	0.00	0.00	0.00	0.00
19	0.00	**5.61**	0.00	**94.39**	0.00	0.00	0.00	0.00
20	0.00	**0.02**	0.00	**99.98**	0.00	0.00	0.00	0.00

Table 7:6, GPS nodes time difference between each recorded position for represented using summary statistics.

Time Difference (Seconds)							
Node	Count	Mode	Median	Minimum value	Maximum value	Maximum value (Days)	Interquartile range
NODE0001	252,336	3.00	4.00	1.00	61245.00	0.71	4.00
NODE0002	113,006	6.00	5.00	1.00	126772.00	1.47	3.00
NODE0003	730,055	6.00	5.00	1.00	92409.00	1.07	4.00
NODE0004	152,665	7.00	6.00	1.00	132804.00	1.54	3.00
NODE0005	406,299	7.00	7.00	1.00	88343.00	1.02	1.00
NODE0006	122,644	7.00	6.00	1.00	48606.00	0.56	1.00
NODE0007	377,668	6.00	4.00	1.00	92450.00	1.07	4.00
NODE0008	865,472	3.00	4.00	1.00	100890.00	1.17	4.00
NODE0009	455,552	6.00	5.00	1.00	86409.00	1.00	3.00
NODE0010	133,823	6.00	5.00	1.00	100001.00	1.16	3.00
NODE0011	171,318	6.00	5.00	1.00	78886.00	0.91	3.00
NODE0012	186,173	6.00	5.00	1.00	59787.00	0.69	4.00
NODE0013	595,533	6.00	4.00	1.00	325833.00	3.77	4.00
NODE0014	248,569	6.00	6.00	1.00	351841.00	4.07	4.00
NODE0015	220,351	6.00	4.00	1.00	86410.00	1.00	4.00
NODE0017	122,620	6.00	5.00	1.00	306300.00	3.55	4.00
NODE0018	265,593	6.00	4.00	1.00	1860893.00	21.54	4.00
NODE0019	98,191	6.00	5.00	1.00	86406.00	1.00	3.00
NODE0020	451,203	3.00	4.00	1.00	86410.00	1.00	4.00

Chapter 8 – References

Abdalati, W., Krabill, W., Frederick, E., Manizade, S., Martin, C., Sonntag, J., Swift, R., Thomas, R., Wright, W., & Yungel, J. (2001). Outlet glacier and margin elevation changes: Near-coastal thinning of the Greenland ice sheet. *Journal of Geophysical Research: Atmospheres*, *106*(D24), 33729–33741. https://doi.org/10.1029/2001JD900192

Amundson, J. M., Truffer, M., Lüthi, M. P., Fahnestock, M., West, M., & Motyka, R. J. (2008). Glacier, fjord, and seismic response to recent large calving events, Jakobshavn Isbræ, Greenland. *Geophysical Research Letters*, *35*(22). https://doi.org/10.1029/2008GL035281

An, L., Rignot, E., Chauche, N., Holland, D. M., Holland, D., Jakobsson, M., Kane, E., Wood, M., Klaucke, I., Morlighem, M., Velicogna, I., Weinrebe, W., & Willis, J. K. (2019). Bathymetry of Southeast Greenland From Oceans Melting Greenland (OMG) Data. *Geophysical Research Letters*, *46*(20), 11197–11205. https://doi.org/10.1029/2019GL083953

An, L., Rignot, E., Wood, M., Willis, J. K., Mouginot, J., & Khan, S. A. (2021). Ocean melting of the Zachariae Isstrøm and nioghalvfjerdsfjorden glaciers, northeast Greenland. *Proceedings of the National Academy of Sciences of the United States of America*, *118*(2), e2015483118. https://doi.org/10.1073/PNAS.2015483118/SUPPL_FILE/PNAS.2015483118.SD01.XLSX

Anandakrishnan, S., & Alley, R. B. (1997). Tidal forcing of basal seismicity of ice stream C, West Antarctica, observed far inland. *Journal of Geophysical Research: Solid Earth*, *102*(B7), 15183–15196. https://doi.org/https://doi.org/10.1029/97JB01073

Anandakrishnan, S., Bilén, S. G., Urbina, J. V., Bock, R. G., Burkett, P. G., & Portelli, J. P. (2022). The geoPebble System: Design and Implementation of a Wireless Sensor Network of GPS-Enabled Seismic Sensors for the Study of Glaciers and Ice Sheets. *Geosciences (Switzerland)*, *12*(1). https://doi.org/10.3390/geosciences12010017

Anandakrishnan, S., Voigt, D. E., Alley, R. B., & King, M. A. (2003). Ice stream D flow speed is strongly modulated by the tide beneath the Ross Ice Shelf. *Geophysical Research Letters*, *30*(7), 1361. https://doi.org/10.1029/2002GL016329

Andersen, M. L., Larsen, T. B., Nettles, M., Elosegui, P., van As, D., Hamilton, G. S., Stearns, L. A., Davis, J. L., Ahlstrøm, A. P., de Juan, J., Ekström, G., Stenseng, L., Khan, S. A., Forsberg, R., & Dahl-Jensen, D. (2010). Spatial and temporal melt variability at Helheim Glacier, East Greenland, and its effect on ice dynamics. *Journal of Geophysical Research: Earth Surface*, *115*(F4). https://doi.org/https://doi.org/10.1029/2010JF001760

Andresen, C. S., Straneo, F., Ribergaard, M. H., Bjørk, A. A., Andersen, T. J., Kuijpers, A., Nørgaard-Pedersen, N., Kjær, K. H., Schjøth, F., Weckström, K., & Ahlstrøm, A. P. (2012). Rapid response of Helheim Glacier in Greenland to climate variability over the past century. *Nature Geoscience*, *5*(1), 37–41. https://doi.org/10.1038/ngeo1349

Aschwanden, A., Fahnestock, M. A., Truffer, M., Brinkerhoff, D. J., Hock, R., Khroulev, C., Mottram, R., & Abbas Khan, S. (2019). Contribution of the Greenland Ice Sheet to sea level over the next millennium. *Science Advances*, *5*(6). https://doi.org/10.1126/SCIADV.AAV9396/SUPPL_FILE/AAV9396_SM.PDF

Bamber, J. L., Oppenheimer, M., Kopp, R. E., Aspinall, W. P., & Cooke, R. M. (2019). Ice sheet contributions to future sea-level rise from structured expert judgment. *Proceedings of the National Academy of Sciences of the United States of America*, *166*(23), 11195–11200. https://doi.org/10.1073/PNAS.1817205116/SUPPL_FILE/PNAS.1817205116.SAPP.PDF

Bamber, J. L., Westaway, R. M., Marzeion, B., & Wouters, B. (2018). The land ice contribution to sea level during the satellite era. *Environmental Research Letters*, *13*(6), 063008. https://doi.org/10.1088/1748-9326/AAC2F0

Bartholomaus, T. C., Anderson, R. S., & Anderson, S. P. (2007). Response of glacier basal motion to transient water storage. *Nature Geoscience 2008 1:1*, *1*(1), 33–37. https://doi.org/10.1038/ngeo.2007.52

Bartholomaus, T. C., Larsen, C. F., & O'Neel, S. (2013). Does calving matter? Evidence for significant submarine melt. *Earth and Planetary Science Letters*, *380*, 21–30. https://doi.org/10.1016/J.EPSL.2013.08.014

Bartholomaus, T. C., Larsen, C. F., West, M. E., O'Neel, S., Pettit, E. C., & Truffer, M. (2015). Tidal and seasonal variations in calving flux observed with passive seismology. *Journal of Geophysical Research: Earth Surface*, *120*(11), 2318–2337. https://doi.org/10.1002/2015JF003641

Benn, D., & Evans, D. J. A. (2014). Glaciers and Glaciation, Second Edition. *Glaciers and Glaciation, Second Edition*, 1–802. https://doi.org/10.4324/9780203785010/GLACIERS-GLACIATION-2ND-EDITION-DOUGLAS-BENN-DAVID-EVANS

Benn, D. I., Åström, J. A. N., Zwinger, T., Todd, J. O. E., Nick, F. M., Cook, S., Hulton, N. R. J., & Luckman, A. (2017). Melt-under-cutting and buoyancy-driven calving from tidewater glaciers: new insights from discrete element and continuum model simulations. *Journal of Glaciology*, *63*(240), 691–702. https://doi.org/10.1017/jog.2017.41

Benn, D. I., Cowton, T., Todd, J., & Luckman, A. (2017). Glacier Calving in Greenland. *Current Climate Change Reports*, *3*(4), 282–290. https://doi.org/10.1007/S40641-017-0070-1/FIGURES/3

Bevan, S. L., Luckman, A. J., & Murray, T. (2012). Glacier dynamics over the last quarter of a century at Helheim, Kangerdlugssuaq and 14 other major Greenland outlet glaciers. *Cryosphere*, *6*(5), 923–937. https://doi.org/10.5194/TC-6-923-2012

Bindoff, N., Willebrand, J., Artale, V., Cazenave, A., Gregory, J., Gulev, S., Hanawa, K., le Quéré, C., Levitus, S., Nojiri, Y., Shum, C., Talley, L., & Unnikrishnan, A. (2007). *Observations: Oceanic Climate Change and Sea Level*. 385–432. http://www.cambridge.org/uk/catalogue/catalogue.asp?isbn=9780521705967

Bindschadler, R. A., King, M. A., Alley, R. B., Anandakrishnan, S., & Padman, L. (2003). Tidally controlled stick-slip discharge of a West Antarctic ice stream. *Science*, *301*(5636), 1087–1089. https://doi.org/10.1126/SCIENCE.1087231/ASSET/6E700DA5-C2CD-4796-AC73-BBF7C628CBD5/ASSETS/GRAPHIC/SE3131768002.JPEG

Bindschadler, R. A., Vornberger, P. L., King, M. A., & Padman, L. (2003). Tidally driven stick-slip motion in the mouth of Whillans Ice Stream, Antarctica. *Annals of Glaciology*, *36*, 263–272. https://doi.org/10.3189/172756403781816284

Błaszczyk, M., Jania, J. A., Ciepły, M., Grabiec, M., Ignatiuk, D., Kolondra, L., Kruss, A., Luks, B., Moskalik, M., Pastusiak, T., Strzelewicz, A., Walczowski, W., & Wawrzyniak, T. (2021). Factors Controlling Terminus Position of Hansbreen, a Tidewater Glacier in Svalbard. *Journal of Geophysical Research: Earth Surface*, *126*(2), e2020JF005763. https://doi.org/10.1029/2020JF005763

Burgess, E. W., Forster, R. R., Box, J. E., Mosley-Thompson, E., Bromwich, D. H., Bales, R. C., & Smith, L. C. (2010). A spatially calibrated model of annual accumulation rate on the Greenland Ice Sheet (1958-2007). *Journal of Geophysical Research: Earth Surface*, *115*(2). https://doi.org/10.1029/2009JF001293

Cassotto, R., Fahnestock, M., Amundson, J. M., Truffer, M., Boettcher, M. S., De, S., Peña, L. A., & Howat, I. (2018). *Non-linear glacier response to calving events, Jakobshavn Isbrae, Greenland*. https://doi.org/10.1017/jog.2018.90

Cassotto, R., Fahnestock, M., Amundson, J. M., Truffer, M., & Joughin, I. (2015). *Seasonal and interannual variations in ice melange and its impact on terminus stability, Jakobshavn Isbræ, Greenland*. https://doi.org/10.3189/2015JoG13J235

Catania, G. A., Stearns, L. A., Moon, T. A., Enderlin, E. M., & Jackson, R. H. (2020). Future Evolution of Greenland's Marine-Terminating Outlet Glaciers. *Journal of Geophysical Research: Earth Surface*, *125*(2). https://doi.org/10.1029/2018JF004873

Catania, G. A., Stearns, L. A., Sutherland, D. A., Fried, M. J., Bartholomaus, T. C., Morlighem, M., Shroyer, E., & Nash, J. (2018). Geometric Controls on Tidewater Glacier Retreat in Central Western Greenland. *Journal of Geophysical Research: Earth Surface*, *123*(8), 2024–2038. https://doi.org/10.1029/2017JF004499

Chadaporn, K., Baber, J., & Bakhtyar, M. (2013). *Simple Example of Applying Extended Kalman Filter*. https://www.researchgate.net/publication/273381901

Chen, G., Hening, T. A., & Supervisor, T. (1998). GPS kinematic positioning for the airborne laser altimetry at Long Valley, California. *Astronomy*. https://dspace.mit.edu/handle/1721.1/9680

Cheng, G., Morlighem, M., Mouginot, J., & Cheng, D. (2022). Helheim Glacier's Terminus Position Controls Its Seasonal and Inter-Annual Ice Flow Variability. *Geophysical Research Letters*, *49*(5). https://doi.org/10.1029/2021GL097085

Christmann, J., Helm, V., Khan, S. A., Kleiner, T., Müller, R., Morlighem, M., Neckel, N., Rückamp, M., Steinhage, D., Zeising, O., & Humbert, A. (2021). Elastic deformation plays a non-negligible role in Greenland's outlet glacier flow. *Communications Earth & Environment*, *2*(1), 232. https://doi.org/10.1038/s43247-021-00296-3

Christoffersen, P., & Hambrey, M. J. (2006). Is the Greenland Ice Sheet in a state of collapse? *Geology Today*, *22*(3), 98–103. https://doi.org/10.1111/J.1365-2451.2006.00561.X

Codiga, D. L. (2011). *Unified Tidal Analysis and Prediction Using the UTide Matlab Functions*. *September*, 59. https://doi.org/10.13140/RG.2.1.3761.2008

Cook, S., Rutt, I. C., Murray, T., Luckman, A., Zwinger, T., Selmes, N., Goldsack, A., & James, T. D. (2014). Modelling environmental influences on calving at Helheim Glacier in eastern Greenland. *Cryosphere*, *8*(3), 827–841. https://doi.org/10.5194/TC-8-827-2014

Davis, J. L., De Juan, J., Nettles, M., Elosegui, P., & Andersen, M. L. (2014). *Evidence for non-tidal diurnal velocity variations of Helheim Glacier, East Greenland*. https://doi.org/10.3189/2014JoG13J230

De Rydt, J., Hilmar Gudmundsson, G., Nagler, T., & Wuite, J. (2019). Calving cycle of the Brunt Ice Shelf, Antarctica, driven by changes in ice shelf geometry. *Cryosphere*, *13*(10), 2771–2787. https://doi.org/10.5194/TC-13-2771-2019

Doake, C. S. M., Corr, H. F. J., Nicholls, K. W., Gaffikin, A., Jenkins, A., Bertiger, W. I., & King, M. A. (2002). Tide-induced lateral movement of Brunt Ice Shelf, Antarctica. *Geophysical Research Letters*, *29*(8), 67–1. https://doi.org/10.1029/2001GL014606

Ekström, G., Nettles, M., & Abers, G. A. (2003). Glacial Earthquakes. *Science*, *302*(5645), 622–624. https://doi.org/10.1126/science.1088057

Enderlin, E. M., Howat, I. M., Jeong, S., Noh, M. J., van Angelen, J. H., & van den Broeke, M. R. (2014). An improved mass budget for the Greenland ice sheet. *Geophysical Research Letters*, *41*(3), 866–872. https://doi.org/10.1002/2013GL059010

Fox-Kemper, B., Aðalgeirsdóttir, G., Drijfhout, S. S., Edwards, T. L., Nicholas R, G., Mark, H., Robert E, K., Gerhard, K., Alan, M., Dirk, N., Sophie, N., Intan Suci, N., Lucas, R., Jean-Baptiste, S., Aimee B.A, S., & Yongqiang, Y. (2021). *Chapter 9: Ocean, Cryosphere and Sea Level Change*. 1211–1362. https://doi.org/10.1017/9781009157896.011

Gallagher, M. R., Chepfer, H., Shupe, M. D., & Guzman, R. (2020). Warm Temperature Extremes Across Greenland Connected to Clouds. *Geophysical Research Letters*, *47*(9). https://doi.org/10.1029/2019GL086059

Gerkema, T. (2019). Introductory Concepts. In *An Introduction to Tides* (pp. 1–26). Cambridge University Press. https://doi.org/10.1017/9781316998793.002

Goliber, S., Black, T., Catania, G., Ginny, C., James M., L., Helene, O., Daniel, C., Suzanne, B., Anders, B., Charlie, B., Stephen, B., J. Rachel, C., Tom, C., Alex, G., Dominik, F., Emily, H., Ian, J., Niels J., K., Adrian, L., … Enze, Z. (2022). *TermPicks: a century of Greenland*

glacier terminus data for use in scientific and machine learning applications. https://doi.org/10.5281/ZENODO.6557981

Gudmundsson, G. H. (2006). Fortnightly variations in the flow velocity of Rutford Ice Stream, West Antarctica. *Nature 2006 444:7122*, *444*(7122), 1063–1064. https://doi.org/10.1038/nature05430

Hanna, E., Cappelen, J., Fettweis, X., Mernild, S. H., Mote, T. L., Mottram, R., Steffen, K., Ballinger, T. J., & Hall, R. J. (2021). Greenland surface air temperature changes from 1981 to 2019 and implications for ice-sheet melt and mass-balance change. *International Journal of Climatology*, *41*(S1), E1336–E1352. https://doi.org/10.1002/JOC.6771

Hanna, E., Fettweis, X., Mernild, S. H., Cappelen, J., Ribergaard, M. H., Shuman, C. A., Steffen, K., Wood, L., & Mote, T. L. (2014). Atmospheric and oceanic climate forcing of the exceptional Greenland ice sheet surface melt in summer 2012. *International Journal of Climatology*, *34*(4), 1022–1037. https://doi.org/10.1002/joc.3743

Hanna, E., Mernild, S. H., Cappelen, J., & Steffen, K. (2012). Recent warming in Greenland in a long-term instrumental (1881–2012) climatic context: I. Evaluation of surface air temperature records. *Environmental Research Letters*, *7*(4), 045404. https://doi.org/10.1088/1748-9326/7/4/045404

Hansen, J., Ruedy, R., Sato, M., & Lo, K. (2010). Global surface temperature change. *Reviews of Geophysics*, *48*(4). https://doi.org/10.1029/2010RG000345

Herdes, E., Copland, L., Danielson, B., & Sharp, M. (2012). Relationships between iceberg plumes and sea-ice conditions on northeast Devon Ice Cap, Nunavut, Canada. *Annals of Glaciology*, *53*(60). https://doi.org/10.3189/2012AoG60A163

Holden, J. (2012). *An Introduction to Physical Geography and the Environment*. Pearson. https://books.google.co.uk/books?id=C0YBuwAACAAJ

Holmes, F. A., Kirchner, N., Kuttenkeuler, J., Krützfeldt, J., & Noormets, R. (2019). Relating ocean temperatures to frontal ablation rates at Svalbard tidewater glaciers: Insights from glacier proximal datasets. *Scientific Reports 2019 9:1*, *9*(1), 1–11. https://doi.org/10.1038/s41598-019-45077-3

Holmes, F. A., Van Dongen, E., Noormets, R., Pętlicki, M., & Kirchner, N. (2023). Impact of tides on calving patterns at Kronebreen, Svalbard - Insights from three-dimensional ice

dynamical modelling. *Cryosphere*, *17*(5), 1853–1872. https://doi.org/10.5194/TC-17-1853-2023

Howat, I. M., Box, J. E., Ahn, Y., Herrington, A., & McFadden, E. M. (2010). Seasonal variability in the dynamics of marine-terminating outlet glaciers in Greenland. *Journal of Glaciology*, *56*(198), 601–613. https://doi.org/10.3189/002214310793146232

Howat, I. M., Joughin, I., Tulaczyk, S., & Gogineni, S. (2005). Rapid retreat and acceleration of Helheim Glacier, east Greenland. *Geophysical Research Letters*, *32*(22), 1–4. https://doi.org/10.1029/2005GL024737

Humbert, A., Helm, V., Neckel, N., Zeising, O., Rückamp, M., Khan, S. A., Loebel, E., Brauchle, J., Stebner, K., Gross, D., Sondershaus, R., & Müller, R. (2023). Precursor of disintegration of Greenland's largest floating ice tongue. *Cryosphere*, *17*(7), 2851–2870. https://doi.org/10.5194/TC-17-2851-2023

Huss, M., & Hock, R. (2015). A new model for global glacier change and sea-level rise. *Frontiers in Earth Science*, *3*, 54. https://doi.org/10.3389/FEART.2015.00054/BIBTEX

IPCC. (2021a). *Climate Change 2021: The Physical Science Basis. Contribution of Working Group I to the Sixth Assessment Report of the Intergovernmental Panel on Climate Change: Vol. In Press*. Cambridge University Press. https://doi.org/10.1017/9781009157896

IPCC. (2021b). Summary for Policymakers. In V. Masson-Delmotte, P. Zhai, A. Pirani, S. L. Connors, C. Péan, S. Berger, N. Caud, Y. Chen, L. Goldfarb, M. I. Gomis, M. Huang, K. Leitzell, E. Lonnoy, J. B. R. Matthews, T. K. Maycock, T. Waterfield, O. Yelekçi, R. Yu, & B. Zhou (Eds.), *Climate Change 2021: The Physical Science Basis. Contribution of Working Group I to the Sixth Assessment Report of the Intergovernmental Panel on Climate Change* (p. 3−32). Cambridge University Press. https://doi.org/10.1017/9781009157896.001

Jackson, R. H. (2010). *Dynamics of Greenland's Glacial Fjords*.

Jackson, R. H., Straneo, F., & Sutherland, D. A. (2014). Externally forced fluctuations in ocean temperature at Greenland glaciers in non-summer months. *Nature Geoscience 2014*, *7*(7), 503–508. https://doi.org/10.1038/ngeo2186

Johannessen, O. M., Korablev, A., Miles, V., Miles, M. W., & Solberg, K. E. (2011). Interaction Between the Warm Subsurface Atlantic Water in the Sermilik Fjord and Helheim

Glacier in Southeast Greenland. *Surveys in Geophysics*, *32*(4–5), 387–396. https://doi.org/10.1007/S10712-011-9130-6

Joughin, I., Abdalati, W., & Fahnestock, M. (2004). Large fluctuations in speed on Greenland's Jakobshavn Isbræ glacier. *Nature 2004 432:7017*, *432*(7017), 608–610. https://doi.org/10.1038/nature03130

Joughin, I., Howat, I., Alley, R. B., Ekström, G., Fahnestock, M., Moon, T., Nettles, M., Truffer, M., & Tsai, V. C. (2008). Ice-front variation and tidewater behavior on Helheim and Kangerdlugssuaq Glaciers, Greenland. *Journal of Geophysical Research: Earth Surface*, *113*(F1), 1004. https://doi.org/10.1029/2007JF000837

Joughin, I., Smith, B. E., Howat, I. M., Floricioiu, D., Alley, R. B., Truffer, M., & Fahnestock, M. (2012). Seasonal to decadal scale variations in the surface velocity of Jakobshavn Isbrae, Greenland: Observation and model-based analysis. *Journal of Geophysical Research: Earth Surface*, *117*(2). https://doi.org/10.1029/2011JF002110

Juan, J. De. (2011). *Tidewater glacier flow of Helheim Glacier, Greenland, 2006-2008, using high-rate GPS*.

Juan, J. De, Elósegui, P., Nettles, M., Larsen, T. B., Davis, J. L., Hamilton, G. S., Stearns, L. A., Andersen, M. L., Ekström, G., Ahlstrøm, A. P., Stenseng, L., Khan, S. A., & Forsberg, R. (2010). Sudden increase in tidal response linked to calving and acceleration at a large Greenland outlet glacier. *Geophysical Research Letters*, *37*(12). https://doi.org/10.1029/2010GL043289

Kalman, R. E. (1960). A new approach to linear filtering and prediction problems. *Journal of Fluids Engineering, Transactions of the ASME*, *82*(1), 35–45. https://doi.org/10.1115/1.3662552

Kamb, B. (1987). Glacier Surge Mechanism Based on Linked Cavity Configuration of the Basal Water Conduit System. *JOURNAL OF GEOPHYSICAL RESEARCH*, *92*(B9). https://doi.org/10.1029/JB092iB09p09083

Karlsson, N. B., Solgaard, A. M., Mankoff, K. D., Gillet-Chaulet, F., MacGregor, J. A., Box, J. E., Citterio, M., Colgan, W. T., Larsen, S. H., Kjeldsen, K. K., Korsgaard, N. J., Benn, D. I., Hewitt, I. J., & Fausto, R. S. (2021). A first constraint on basal melt-water production of the Greenland ice sheet. *Nature Communications 2021 12:1*, *12*(1), 1–10. https://doi.org/10.1038/s41467-021-23739-z

Kehrl, L. M., Joughin, I., Shean, D. E., Floricioiu, D., & Krieger, L. (2017). Seasonal and interannual variabilities in terminus position, glacier velocity, and surface elevation at Helheim and Kangerlussuaq Glaciers from 2008 to 2016. *Journal of Geophysical Research: Earth Surface*, *122*(9), 1635–1652. https://doi.org/10.1002/2016JF004133

Khan, S. A., Aschwanden, A., Bjørk, A. A., Wahr, J., Kjeldsen, K. K., & Kjaær, K. H. (2015). Greenland ice sheet mass balance: a review. *Reports on Progress in Physics*, *78*(4), 046801. https://doi.org/10.1088/0034-4885/78/4/046801

Khan, S. A., Bjørk, A. A., Bamber, J. L., Morlighem, M., Bevis, M., Kjær, K. H., Mouginot, J., Løkkegaard, A., Holland, D. M., Aschwanden, A., Zhang, B., Helm, V., Korsgaard, N. J., Colgan, W., Larsen, N. K., Liu, L., Hansen, K., Barletta, V., Dahl-Jensen, T. S., … Schenk, T. (2020). Centennial response of Greenland's three largest outlet glaciers. *Nature Communications*, *11*(1). https://doi.org/10.1038/S41467-020-19580-5

Khan, S. A., Kjeldsen, K. K., Kjær, K. H., Bevan, S., Luckman, A., Bjørk, A. A., Korsgaard, N. J., Box, J. E., van den Broeke, M., van Dam, T. M., & Fitzner, A. (2014). Glacier dynamics at Helheim and Kangerdlugssuaq glaciers, southeast Greenland, since the Little Ice Age. *Cryosphere*, *8*(4), 1497–1507. https://doi.org/10.5194/TC-8-1497-2014

Khazendar, A., Fenty, I. G., Carroll, D., Gardner, A., Lee, C. M., Fukumori, I., Wang, O., Zhang, H., Seroussi, H., Moller, D., Noël, B. P. Y., van den Broeke, M. R., Dinardo, S., & Willis, J. (2019). Interruption of two decades of Jakobshavn Isbrae acceleration and thinning as regional ocean cools. *Nature Geoscience*, *12*(4), 277–283. https://doi.org/10.1038/s41561-019-0329-3

King, M. (2004). Rigorous GPS data-processing strategies for glaciological applications. *Journal of Glaciology*, *50*(171), 601–607. https://doi.org/10.3189/172756504781829747

Krabill, W., Hanna, E., Huybrechts, P., Abdalati, W., Cappelen, J., Csatho, B., Frederick, E., Manizade, S., Martin, C., Sonntag, J., Swift, R., Thomas, R., & Yungel, J. (2004). Greenland Ice Sheet: Increased coastal thinning. *Geophysical Research Letters*, *31*(24), 1–4. https://doi.org/10.1029/2004GL021533

Krug, J., Weiss, J., Gagliardini, O., & Durand, G. (2014). Combining damage and fracture mechanics to model calving. *The Cryosphere*, *8*, 2101–2117. https://doi.org/10.5194/tc-8-2101-2014

Kvale, E. P. (2006). The origin of neap–spring tidal cycles. *Marine Geology*, *235*(1–4), 5–18. https://doi.org/10.1016/J.MARGEO.2006.10.001

Larsen, C. F., Burgess, E., Arendt, A. A., O'Neel, S., Johnson, A. J., & Kienholz, C. (2015). Surface melt dominates Alaska glacier mass balance. *Geophysical Research Letters*, *42*(14), 5902–5908. https://doi.org/10.1002/2015GL064349

Leffler, K. E., & Jay, D. A. (2009). Enhancing tidal harmonic analysis: Robust (hybrid L1 / L2) solutions. *Continental Shelf Research*, *29*(1), 78–88. https://doi.org/10.1016/J.CSR.2008.04.011

Lemke, P., Ren, J., Alley, R. B., Allison, I., Carrasco, J., Flato, G., Fujii, Y., Kaser Austria, G., Mote, P., Thomas, R. H., Barry, R., Koike, T., Ren, J., Alley, R., Allison, I., Carrasco, J., Flato, G., Fujii, Y., Kaser, G., … Tignor, M. (2007). *Observations: Changes in Snow, Ice and Frozen Ground*.

Luckman, A., Benn, D. I., Cottier, F., Bevan, S., Nilsen, F., & Inall, M. (2015). Calving rates at tidewater glaciers vary strongly with ocean temperature. *Nature Communications*. https://doi.org/10.1038/ncomms9566

Luckman, A., Murray, T., de Lange, R., & Hanna, E. (2006). Rapid and synchronous ice-dynamic changes in East Greenland. *Geophysical Research Letters*, *33*(3). https://doi.org/10.1029/2005GL025428

M. Floyd. (2023). *GAMIT/GLOBK*. http://geoweb.mit.edu/gg/

Mankoff, K. D., Solgaard, A., Colgan, W., Ahlstrøm, A. P., Abbas Khan, S., & Fausto, R. S. (2020). Greenland Ice Sheet solid ice discharge from 1986 through March 2020. *Earth System Science Data*, *12*, 1367–1383. https://doi.org/10.5194/essd-12-1367-2020

Martin, I., O'Farrell, T., Aspey, R., Edwards, S., James, T., Loskot, P., Murray, T., Rutt, I., Selmes, N., & Baugé, T. (2014). A high-resolution sensor network for monitoring glacier dynamics. *IEEE Sensors Journal*, *14*(11), 3926–3931. https://doi.org/10.1109/JSEN.2014.2348534

Medrzycka, D., Benn, D. I., Box, J. E., Copland, L., & Balog, J. (2016). Calving Behavior at Rink Isbræ, West Greenland, from Time-Lapse Photos. *Https://Doi.Org/10.1657/AAAR0015-059*, *48*(2), 263–277. https://doi.org/10.1657/AAAR0015-059

Meier, M. F., & Post, A. (1987). Fast tidewater glaciers. *Journal of Geophysical Research*, *92*(B9), 9051–9058. https://doi.org/10.1029/JB092iB09p09051

Mernild, S. H., Hanna, E., Yde, J. C., Cappelen, J., & Malmros, J. K. (2014). Coastal Greenland air temperature extremes and trends 1890-2010: Annual and monthly analysis. *International Journal of Climatology*, *34*(5), 1472–1487. https://doi.org/10.1002/JOC.3777

Miles, V. v., Miles, M. W., & Johannessen, O. M. (2016). Satellite archives reveal abrupt changes in behavior of Helheim Glacier, southeast Greenland. *Journal of Glaciology*, *62*(231), 137–146. https://doi.org/10.1017/jog.2016.24

Minchew, B. M., Simons, M., Riel, B., & Milillo, P. (2017). Tidally induced variations in vertical and horizontal motion on Rutford Ice Stream, West Antarctica, inferred from remotely sensed observations. *Journal of Geophysical Research: Earth Surface*, *122*(1), 167–190. https://doi.org/10.1002/2016JF003971

Moon, T., & Joughin, I. (2008). Changes in ice front position on Greenland's outlet glaciers from 1992 to 2007. *Journal of Geophysical Research: Earth Surface*, *113*(F2), 2022. https://doi.org/10.1029/2007JF000927

Morlighem, M., Williams, C. N., Rignot, E., An, L., Arndt, J. E., Bamber, J. L., Catania, G., Chauché, N., Dowdeswell, J. A., Dorschel, B., Fenty, I., Hogan, K., Howat, I., Hubbard, A., Jakobsson, M., Jordan, T. M., Kjeldsen, K. K., Millan, R., Mayer, L., … Zinglersen, K. B. (2017). BedMachine v3: Complete Bed Topography and Ocean Bathymetry Mapping of Greenland From Multibeam Echo Sounding Combined With Mass Conservation. *Geophysical Research Letters*, *44*(21), 11,051-11,061. https://doi.org/10.1002/2017GL074954

Motyka, R. J., Hunter, L., Echelmeyer, K. A., & Connor, C. (2003). Submarine melting at the terminus of a temperate tidewater glacier, LeConte Glacier, Alaska, U.S.A. *Annals of Glaciology*, *36*, 57–65. https://doi.org/10.3189/172756403781816374

Mouginot, J., Rignot, E., Bjørk, A. A., van den Broeke, M., Millan, R., Morlighem, M., Noël, B., Scheuchl, B., & Wood, M. (2019). Forty-six years of Greenland Ice Sheet mass balance from 1972 to 2018. *Proceedings of the National Academy of Sciences of the United States of America*, *116*(19), 9239–9244. https://doi.org/10.1073/PNAS.1904242116/-/DCSUPPLEMENTAL

Murray, T., Nettles, M., Selmes, N., Cathles, L. M., Burton, J. C., James, T. D., Edwards, S., Martin, I., O'Farrell, T., Aspey, R., Rutt, I., & Baugé, T. (2015). Reverse glacier motion during iceberg calving and the cause of glacial earthquakes. *Science*, *349*(6245), 305–

308. https://doi.org/10.1126/SCIENCE.AAB0460/SUPPL_FILE/AAB0460-MURRAY-SM.PDF

Murray, T., Scharrer, K., James, T. D., Dye, S. R., Hanna, E., Booth, A. D., Selmes, N., Luckman, A., Hughes, A. L. C., Cook, S., & Huybrechts, P. (2010). Ocean regulation hypothesis for glacier dynamics in southeast Greenland and implications for ice sheet mass changes. *Journal of Geophysical Research: Earth Surface*, *115*(F3), 3026. https://doi.org/10.1029/2009JF001522

Murray, T., Scharrer, K., Selmes, N., Booth, A. D., James, T. D., Bevan, S. L., Bradley, J., Cook, S., Llana, L. C., Drocourt, Y., Dyke, L., Goldsack, A., Hughes, A. L., Luckman, A. J., & McGovern, J. (2015). Extensive Retreat of Greenland Tidewater Glaciers, 2000-2010. *Arctic, Antarctic, and Alpine Research*, *47*(3), 427–447. https://doi.org/10.1657/AAAR0014-049/SUPPL_FILE/UAAR_A_11957844_SM0001.KMZ

Murray, T., Selmes, N., James, T. D., Edwards, S., Martin, I., O'Farrell, T., Aspey, R., Rutt, I., Nettles, M., & Baugé, T. (2015). Dynamics of glacier calving at the ungrounded margin of Helheim Glacier, southeast Greenland. *Journal of Geophysical Research: Earth Surface*, *120*(6), 964–982. https://doi.org/10.1002/2015JF003531

Murray, T., Smith, A. M., King, M. A., & Weedon, G. P. (2007). Ice flow modulated by tides at up to annual periods at Rutford Ice Stream, West Antarctica. *Geophysical Research Letters*, *34*(18). https://doi.org/10.1029/2007GL031207

Nettles, M., & Ekström, G. (2010). Glacial earthquakes in Greenland and Antarctica. *Annual Review of Earth and Planetary Sciences*, *38*, 467–491. https://doi.org/10.1146/annurev-earth-040809-152414

Nettles, M., Larsen, T. B., Elósegui, P., Hamilton, G. S., Stearns, L. A., Ahlstrøm, A. P., Davis, J. L., Andersen, M. L., De Juan, J., Khan, S. A., Stenseng, L., Ekström, G., & Forsberg, R. (2008). Step-wise changes in glacier flow speed coincide with calving and glacial earthquakes at Helheim Glacier, Greenland. *Geophysical Research Letters*, *35*(24). https://doi.org/10.1029/2008GL036127

Nick, F. M., van der Veen, C. J., Vieli, A., & Benn, D. I. (2010). A physically based calving model applied to marine outlet glaciers and implications for the glacier dynamics. *Journal of Glaciology, Vol. 56, No. 199, 2010*, *56*(199). https://doi.org/10.3189/002214310794457344

Nick, F. M., Vieli, A., Andersen, M. L., Joughin, I., Payne, A., Edwards, T. L., Pattyn, F., & Van De Wal, R. S. W. (2013). Future sea-level rise from Greenland's main outlet glaciers in a warming climate. *Nature 2013 497:7448*, *497*(7448), 235–238. https://doi.org/10.1038/nature12068

NOAA. (2023, January 20). *What is an iceberg?* National Ocean Service . https://oceanservice.noaa.gov/facts/iceberg.html#:~:text=A%20bergy%20bit%20is%20a,a%20truck%20or%20grand%20piano.

NOAA National Centers for Environmental Information. (2021, January). *Monthly Global Climate Report for Annual 2020*. NOAA. https://www.ncei.noaa.gov/access/monitoring/monthly-report/global/202013

Nyen Thin, L., Ying Ting, L., Adila Husna, N., & Heikal Husin, M. (2016). GPS Systems Literature: Inaccuracy Factors And Effective Solutions. *International Journal of Computer Networks & Communications (IJCNC)*, *8*(2). https://doi.org/10.5121/ijcnc.2016.8211

Ohmura, A. (2011). Observed Mass Balance of Mountain Glaciers and Greenland Ice Sheet in the 20th Century and the Present Trends. *Surveys in Geophysics*, *32*(4–5), 537–554. https://doi.org/10.1007/s10712-011-9124-4

O'Leary, M., & Christoffersen, P. (2013). Calving on tidewater glaciers amplified by submarine frontal melting. *Cryosphere*, *7*(1), 119–128. https://doi.org/10.5194/TC-7-119-2013

O'Neel, S., Echelmeyer, K. A., & Motyka, R. J. (2003). Short-term variations in calving of a tidewater glacier: LeConte Glacier, Alaska, U.S.A. *Journal of Glaciology*, *49*(167), 587–598. https://doi.org/10.3189/172756503781830430

Parker, B. B., Gutierrez, C. M., Lautenbacher, C. C., Dunnigan, J. H., Administrator, A., & Szabados, M. (2007). *Tidal Analysis and Prediction*. http://tidesandcurrents.noaa.gov

Pawlowicz, R., Beardsley, B., & Lentz, S. (2002). Classical tidal harmonic analysis including error estimates in MATLAB using T_TIDE. *Computers & Geosciences*, *28*(8), 929–937. https://doi.org/10.1016/S0098-3004(02)00013-4

Pearson, C. E. R. (2018). *Network Solution as a Facilitator for Precise Point Positioning Real-Time Kinematic (PPP-RTK)*.

Podolskiy, E. A., Sugiyama, S., Funk, M., Walter, F., Genco, R., Tsutaki, S., Minowa, M., & Ripepe, M. (2016). Tide-modulated ice flow variations drive seismicity near the calving front of Bowdoin Glacier, Greenland. *Geophysical Research Letters*, *43*(5), 2036–2044. https://doi.org/10.1002/2016GL067743

Podrasky, D., Truffer, M., Lu¨thi, M., Lu¨thi, L., & Fahnestock, M. (2014). *Quantifying velocity response to ocean tides and calving near the terminus of Jakobshavn Isbrae, Greenland*. https://doi.org/10.3189/2014JoG13J130

Post, A., O'Neel, S., Motyka, R. J., & Streveler, G. (2011). A complex relationship between calving glaciers and climate. *Eos*, *92*(37), 305–306. https://doi.org/10.1029/2011EO370001

QGIS Development Team. (2009). *QGIS Geographic Information System*. http://qgis.org

Ray, R. D., & Egbert, G. D. (2004). The Global S1 Tide. *Journal of Physical Oceanography*, *34*(8), 1922–1935. https://doi.org/https://doi.org/10.1175/1520-0485(2004)034<1922:TGST>2.0.CO;2

Rignot, E., Braaten, D., Gogineni, S. P., Krabill, W. B., & McConnell, J. R. (2004). Rapid ice discharge from southeast Greenland glaciers. *Geophysical Research Letters*, *31*(10), 10401. https://doi.org/10.1029/2004GL019474

Rignot, E., & Kanagaratnam, P. (2006). Changes in the velocity structure of the Greenland Ice Sheet. *Science*, *311*(5763), 986–990. https://doi.org/10.1126/SCIENCE.1121381

Sanz Subirana, Jaime., Hernandez-Pajares, Manuel., & Juan Zornoza, J. Miguel. (2013). *GNSS data processing : Fundamentals and algorithms*. European Space Agency.

Schild, K. M., & Hamilton, G. S. (2013). Seasonal variations of outlet glacier terminus position in Greenland. *Journal of Glaciology*, *59*(216), 759–770. https://doi.org/10.3189/2013JOG12J238

Schoof, C. (2010). Ice-sheet acceleration driven by melt supply variability. *Nature*. https://doi.org/10.1038/nature09618

Sergeant, A., Mangeney, A., Yastrebov, V. A., Walter, F., Montagner, J.-P., Castelnau, O., Stutzmann, E., Bonnet, P., Jean-Luc Ralaiarisoa, V., Bevan, S., & Luckman, A. (2019). Monitoring Greenland ice sheet buoyancy-driven calving discharge using glacial earthquakes. *Annals of Glaciology*, *60*(79), 75–95. https://doi.org/10.1017/aog.2019.7

Sergienko, O. V., Bindschadler, R. A., Vornberger, P. L., & MacAyeal, D. R. (2008). Ice stream basal conditions from block-wise surface data inversion and simple regression models of ice stream flow: Application to Bindschadler Ice Stream. *Journal of Geophysical Research: Earth Surface*, *113*(4). https://doi.org/10.1029/2008JF001004

Sevestre, H., Benn, D. I., Luckman, A., Nuth, C., Kohler, J., Lindbäck, K., & Pettersson, R. (2018). Tidewater Glacier Surges Initiated at the Terminus. *Journal of Geophysical Research: Earth Surface*, *123*(5), 1035–1051. https://doi.org/10.1029/2017JF004358

Shoemaker, E. M. (1986). The Formation of Fjord Thresholds. *Journal of Glaciology*, *32*(110), 65–71. https://doi.org/10.3189/S0022143000006894

Slater, D. A., & Straneo, F. (2022). Submarine melting of glaciers in Greenland amplified by atmospheric warming. *Nature Geoscience 2022 15:10*, *15*(10), 794–799. https://doi.org/10.1038/s41561-022-01035-9

Smith, J. A., Callard, L., Bentley, M. J., Jamieson, S. S. R., Sánchez-Montes, M. L., Lane, T. P., Lloyd, J. M., McClymont, E. L., Darvill, C. M., Rea, B. R., O'Cofaigh, C., Gulliver, P., Ehrmann, W., Jones, R. S., & Roberts, D. H. (2023). Holocene history of the 79N ice shelf reconstructed from epishelf lake and uplifted glaciomarine sediments. *The Cryosphere*, *17*(3), 1247–1270. https://doi.org/10.5194/tc-17-1247-2023

Stern, A. A., Adcroft, A., Sergienko, O., & Marques, G. (2017). Modeling tabular icebergs submerged in the ocean. *Journal of Advances in Modeling Earth Systems*, *9*(4), 1948–1972. https://doi.org/https://doi.org/10.1002/2017MS001002

Stevens, L. A., Nettles, M., Davis, J. L., Creyts, T. T., Kingslake, J., Ahlstrom, A. P., & Larsen, T. B. (2022). Helheim Glacier diurnal velocity fluctuations driven by surface melt forcing. *Journal of Glaciology*, *68*(267), 77–89. https://doi.org/10.1017/JOG.2021.74

Straneo, F., Hamilton, G. S., Stearns, L. A., & Sutherland, D. A. (2016). Connecting the Greenland Ice Sheet and the ocean: A case study of Helheim Glacier and Sermilik Fjord. *Oceanography*, *29*(4), 34–45. https://doi.org/10.5670/oceanog.2016.97

Straneo, F., Hamilton, G. S., Sutherland, D. A., Stearns, L. A., Davidson, F., Hammill, M. O., Stenson, G. B., & Rosing-Asvid, A. (2010). Rapid circulation of warm subtropical waters in a major glacial fjord in East Greenland. *Nature Geoscience*, *3*, 182–186. https://doi.org/10.1038/NGEO764

Straneo, F., & Heimbach, P. (2013). North Atlantic warming and the retreat of Greenland's outlet glaciers. *Nature 2013 504:7478*, *504*(7478), 36–43. https://doi.org/10.1038/nature12854

Straneo, F., Heimbach, P., Sergienko, O., Hamilton, G., Catania, G., Griffies, S., Hallberg, R., Jenkins, A., Joughin, I., Motyka, R., Pfeffer, W. T., Price, S. F., Rignot, E., Scambos, T., Truffer, M., & Vieli, A. (2013). Challenges to understanding the dynamic response of Greenland's marine terminating glaciers to oceanic and atmospheric forcing. *Bulletin of the American Meteorological Society*, *94*(8), 1131–1144. https://doi.org/10.1175/BAMS-D-12-00100.1

Sugiyama, S., Sakakibara, D., Tsutaki, S., Maruyama, M., & Sawagaki, T. (2015). Glacier dynamics near the calving front of Bowdoin Glacier, northwestern Greenland. *Journal of Glaciology*, *61*(226), 223–232. https://doi.org/10.3189/2015JOG14J127

Sutherland, D. A., & Straneo, F. (2012). Estimating ocean heat transports and submarine melt rates in Sermilik Fjord, Greenland, using lowered acoustic Doppler current profiler (LADCP) velocity profiles. *Annals of Glaciology*, *53*(60), 50–58. https://doi.org/10.3189/2012AOG60A050

Sutherland, D. A., Straneo, F., Stenson, G. B., Davidson, F. J. M., Hammill, M. O., & Rosing-Asvid, A. (2013). Atlantic water variability on the SE Greenland continental shelf and its relationship to SST and bathymetry. *Journal of Geophysical Research: Oceans*, *118*(2), 847–855. https://doi.org/10.1029/2012JC008354

Thomas, R. H. (2007). Tide-induced perturbations of glacier velocities. *Global and Planetary Change*, *59*(1–4), 217–224. https://doi.org/10.1016/J.GLOPLACHA.2006.11.017

Thomson, R. E., & Emery, W. J. (2014). The Spatial Analyses of Data Fields. *Data Analysis Methods in Physical Oceanography*, 313–424. https://doi.org/10.1016/B978-0-12-387782-6.00004-1

Truffer, M., & Motyka, R. J. (2016). Where glaciers meet water: Subaqueous melt and its relevance to glaciers in various settings. *Reviews of Geophysics*, *54*(1), 220–239. https://doi.org/10.1002/2015RG000494

Tuckett, P. A., Ely, J. C., Sole, A. J., Livingstone, S. J., Davison, B. J., Melchior van Wessem, J., & Howard, J. (2019). Rapid accelerations of Antarctic Peninsula outlet glaciers driven

by surface melt. *Nature Communications 2019 10:1*, *10*(1), 1–8. https://doi.org/10.1038/s41467-019-12039-2

Ultee, L., Felikson, D., Minchew, B., Stearns, L. A., & Riel, B. (2022). Helheim Glacier ice velocity variability responds to runoff and terminus position change at different timescales. *Nature Communications*, *13*(1), 6022. https://doi.org/10.1038/s41467-022-33292-y

Våge, K., Pickart, R. S., Sarafanov, A., Knutsen, Ø., Mercier, H., Lherminier, P., van Aken, H. M., Meincke, J., Quadfasel, D., & Bacon, S. (2011). The Irminger Gyre: Circulation, convection, and interannual variability. *Deep Sea Research Part I: Oceanographic Research Papers*, *58*(5), 590–614. https://doi.org/10.1016/J.DSR.2011.03.001

Van Den Broeke, M. R., Enderlin, E. M., Howat, I. M., Kuipers Munneke, P., Noël, B. P. Y., Jan Van De Berg, W., Van Meijgaard, E., & Wouters, B. (2016). On the recent contribution of the Greenland ice sheet to sea level change. *Cryosphere*, *10*(5), 1933–1946. https://doi.org/10.5194/TC-10-1933-2016

Van Rossum, G., & Drake Jr, F. L. (1995). *Python tutorial*. Centrum voor Wiskunde en Informatica Amsterdam, The Netherlands.

Vaňková, I., & Holland, D. M. (2016). Calving signature in ocean waves at Helheim Glacier and Sermilik Fjord, East Greenland. *Journal of Physical Oceanography*, *46*(10), 2925–2941. https://doi.org/10.1175/JPO-D-15-0236.1

Vieli, A., Funk, M., & Blatter, H. (2001). Flow dynamics of tidewater glaciers : a numerical modelling approach. *Journal of Glaciology*, *47*(159), 595–606. https://doi.org/10.3189/172756501781831747

Vijay, S., Khan, S. A., Kusk, A., Solgaard, A. M., Moon, T., & Bjørk, A. A. (2019). Resolving Seasonal Ice Velocity of 45 Greenlandic Glaciers With Very High Temporal Details. *Geophysical Research Letters*, *46*(3), 1485–1495. https://doi.org/10.1029/2018GL081503

Voytenko, D., Stern, A., Holland, D. M., Dixon, T. H., Christianson, K., & Walker, R. T. (2015). Tidally driven ice speed variation at Helheim Glacier, Greenland, observed with terrestrial radar interferometry. *Journal of Glaciology*, *61*(226), 301–308. https://doi.org/10.3189/2015JOG14J173

Walter, J. I., Box, J. E., Tulaczyk, S., Brodsky, E. E., Howat, I. M., Ahn, Y., & Brown, A. (2012). Oceanic mechanical forcing of a marine-terminating Greenland glacier. *Annals of Glaciology*, *53*(60), 181–192. https://doi.org/10.3189/2012AoG60A083

Walters, R. A., & Dunlap, W. W. (1987). Analysis of time series of glacier speed: Columbia Glacier, Alaska. *Journal of Geophysical Research: Solid Earth*, *92*(B9), 8969–8975. https://doi.org/10.1029/JB092IB09P08969

Weidick, A., Williams, R. S., & Ferrigno, J. G. (1995). *Satellite Image Atlas of Glaciers of the World: Greenland*.

Welch, G., & Bishop, G. (1995). An Introduction to the Kalman Filter. *University of North Carolina*. http://www.cs.unc.edu/~gb

Williams, J. J., Gourmelen, N., Nienow, P., Bunce, C., & Slater, D. (2021). Helheim Glacier Poised for Dramatic Retreat. *Geophysical Research Letters*, *48*(23), e2021GL094546. https://doi.org/10.1029/2021GL094546

Winberry, J. P., Anandakrishnan, S., Alley, R. B., Bindschadler, R. A., & King, M. A. (2009). Basal mechanics of ice streams: Insights from the stick-slip motion of Whillans Ice Stream, West Antarctica. *Journal of Geophysical Research: Earth Surface*, *114*(F1), 1016. https://doi.org/10.1029/2008JF001035

Zhang, M., & Zhang, J. (2009). A fast satellite selection algorithm: Beyond four satellites. *IEEE Journal on Selected Topics in Signal Processing*, *3*(5), 740–747. https://doi.org/10.1109/JSTSP.2009.2028381

Zhong, M., Simons, M., Minchew, B., & Zhu, L. (2023). Inferring Tide-Induced Ephemeral Grounding in an Ice-Shelf-Stream System: Rutford Ice Stream, West Antarctica. *Journal of Geophysical Research: Earth Surface*, *128*(2), e2022JF006789. https://doi.org/10.1029/2022JF006789